Cy 2

AD A060 050

AMMRC CTR 76-32 VOLUME II

BRITTLE MATERIALS DESIGN, HIGH TEMPERATURE GAS TURBINE STATOR VANE DEVELOPMENT AND STATIC RIG TESTS

Technical Report By:

Donald G. Miller, Westinghouse Electric Corp., Pittsburgh, PA 15235
C. Robert Booher, Jr., Westinghouse Electric Corp., Lester, PA 19113

Program Manager:

Raymond J. Bratton, Westinghouse Electric Corp., Pittsburgh, PA 15235

December, 1976

Final Report

Contract Number DAAG 46-71-C-0162

Sponsored by the Advanced Research Projects Agency

ARPA Order Number 1849

Project Code Number 1D10

Agency Accession Number DA OD 4733

Approved for public release; distribution unlimited.

Prepared for

ARMY MATERIALS AND MECHANICS RESEARCH CENTER
Watertown, Massachusetts 02172

The findings in this report are not to be construed as an official Advanced Research Projects Agency, Department of the Army, or U.S. Government position, either expressed or implied, unless so designated by other authorized documents.

Mention of any trade names or manufacturers in this report shall not be construed as advertising nor as an official indorsement or approval of such products or companies by the United States Government.

DISPOSITION INSTRUCTIONS

Destroy this report when it is no longer needed. Do not return it to the originator.

AMMRC CTR 76-32 Volume II

BRITTLE MATERIALS DESIGN HIGH TEMPERATURE GAS TURBINE STATOR VANE DEVELOPMENT AND STATIC RIG TESTS

Technical Report By:

Donald G. Miller, Westinghouse Electric Corp., Pittsburgh, PA.15235
C. Robert Booher, Jr., Westinghouse Electric Corp., Lester, PA. 19113

Program Manager:

Raymond J. Bratton, Westinghouse Electric Corp., Pittsburgh, PA 15235

December, 1976

Final Report

Contract Number DAAG 46-71-C-0162

Sponsored by the Advanced Research Projects Agency

ARPA Order Number 1849

Project Code Number 1D10

Agency Accession Number DA OD 4733

Approved for public release; distribution unlimited.

Prepared for:

ARMY MATERIALS AND MECHANICS RESEARCH CENTER
Watertown, Massachusetts 02172

ABSTRACT

The three-piece design concept of a separate airfoil section confined within an inner and outer end cap to produce first stage stator vane assemblies for large industrial gas turbines from brittle ceramic materials was reduced to practice in three design iterations. All of the spring-loaded support structures (the insulator blocks, cushions, metal shoes, seals, pivots and plungers) required to adapt the ceramic vanes to the turbine configuration were developed, manufactured and tested. The Norton Company manufactured all stator vane assembly component parts from hot pressed silicon nitride (HS130/NC132) or hot pressed silicon carbide (NC203).

Static rig tests were conducted under cyclic conditions, controlled to simulate a turbine environment in peaking power to service at 2200 and 2500°F peak inlet temperature at 0.8 turbine simulation. First generation HS130 silicon nitride vanes remained fully functional after 106 cycles of testing from 2200 to 1200°F with the shutdown transient at 25°F/sec. Contact stress superimposed upon transient thermal stress produced extensive cracks in four of eight airfoils and two of sixteen end caps. The initial attempt to test at 2500°F was terminated prematurely on the fifth cycle when a combustor implosion and apparent ceramic exhaust duct damage precipitated a temperature excursion to 3000°F under conditions of choked flow leading to catastrophic rig failure and subsequent rapid quench to the compressor discharge temperature (600°F). Cracks developed in one of four Si_3N_4 airfoils and two of eight end caps. All elements of four SiC stator vane assemblies (end caps and airfoils) were virtually destroyed.

The static rig was rebuilt with a cooled combustor, water-cooled metal exhaust duct and water-spray cooled mixer. Final design configuration NC132 silicon nitride vane assemblies were installed with boron nitride insulators. Testing resumed at 2500°F. After 25 cycles, contact stresses resulting from gross misalignment of the test rig produced failure indications in four of eight airfoils and one end cap. Two incidents of transient thermal-stress-induced failure were identified during the next thirty-five cycles. A single trailing edge crack was observed at the conclusion of 2500°F testing after the last forty-three cycles had been run. The airfoil in cascade position 4, which experienced the most severe conditions in a highly temperature-profiled gas stream survived all 103 cycles. The rig functioned perfectly in its modified form. Subsequent failure analysis and supportive stress analysis indicated failures to be of a statistical nature controlled by the scatter of critical mechanical properties within the vane material. The design was considered viable.

SUMMARY

The three-piece design concept of a separate airfoil section confined within an inner and outer end cap to produce first stage stator vane assemblies for large industrial gas turbines from brittle ceramic materials was reduced to practice in three design iterations. All of the spring-loaded support structure components (the insulator blocks, cushions, metal shoes, seals, pivots and plungers) required to adapt the ceramic vane components to the turbine configuration were developed, manufactured and tested.

The Norton Company produced twenty vane sets to meet the first generation design specification (inner and outer end cap with nontapered nontwisted airfoil) from HS130 hot pressed silicon nitride. Eight similar assemblies were later made from Noralide NC203 silicon carbide. Both hot pressed silicon nitride (HS130) and silicon carbide (Noralide NC203) were used in the manufacture of sixteen vane assemblies of second generation design (inner and outer end cap with tapered-twisted airfoils which had tenon geometry developed fully to conform in total volume to the end cap cavities at either end, the so-called dog-bone design). Noralide NC132 silicon nitride was used exclusively in the fabrication of twenty, three-piece stator vane assemblies of the third generation or final design (inner and outer end cap with tapered-twisted airfoil).

Static rig tests were conducted under cyclic conditions, controlled to simulate a turbine environment in peaking power service at 2200 and 2500°F peak inlet temperature with 0.8 actual turbine pressure ratio achieved (8 atmospheres rather than 10.5). First generation HS130 silicon nitride vanes remained fully functional after 106 cycles of testing from 2200 to 1200°F with the shutdown transient at 25°F/sec. Contact stress superimposed upon transient thermal stress produced extensive cracks in four of eight airfoils and two of sixteen end caps, however. The initial attempt to test at 2500°F was terminated prematurely on the fifth cycle when a combustor implosion and apparent ceramic exhaust duct damage precipitated a temperature excursion to 3000°F under conditions of choked flow leading to catastrophic rig failure and subsequent rapid quench to the compressor discharge temperature (600°F). Cracks were formed in one of four Si_3N_4 airfoils and two of eight end caps, while all elements of four SiC stator vane assemblies, end caps and airfoils alike, were virtually destroyed.

The static rig was rebuilt with an extensively cooled combustor, water-cooled metal exhaust duct and water-spray cooled mixer. Final design configuration NC132 silicon nitride vane assemblies were installed with boron nitride insulators. Testing resumed at 2500°F. After 25 cycles, contact stresses resulting from gross misalignment of the test rig produced failure indications in four of eight airfoils and one end cap. Two incidents of transient thermal-stress-induced failure were identified during the next thirty-five cycles. A single trailing edge crack was observed at the conclusion of 2500°F testing after the last forty-three cycles had been run. The airfoil in cascade position 4, which experienced the most severe conditions in a highly temperature-profiled gas stream survived all 103 cycles. The rig functioned perfectly in its modified form.

Subsequent failure analysis and supportive stress analysis indicated failures to be of a statistical nature controlled by the scatter of critical mechanical properties within the vane material. The design was considered viable.

TABLE OF CONTENTS

Section Page

FOREWORD xviii

SECTION 1 INTRODUCTION 1

SECTION 2 PRELIMINARY DESIGN AND ANALYSIS 9

2.1 DESIGN 9
2.2 ANALYSIS 10
2.3 CORRELATION OF DESIGN ANALYSIS CODES 19

SECTION 3 STATOR VANE SYSTEM DESIGN CONCEPTS 25

3.1 INTRODUCTION 25
3.2 FIRST GENERATION STATOR VANE ASSEMBLY DESIGN 33
3.3 FIRST GENERATION STATOR VANE ANALYSIS 37
3.4 INSULATOR ANALYSIS - PRELIMINARY DESIGN REQUIREMENTS . . . 57
3.5 THE KINEMATIC MODEL 61
3.6 SECOND GENERATION VANE ASSEMBLY DESIGN 63
3.7 THIRD GENERATION VANE ASSEMBLY DESIGN 79

SECTION 4 STATIC RIG TESTING. 81

4.1 STATIC RIG PREPARATION 81
4.2 DEFINITION OF THE STATIC RIG TEST CYCLE 87
4.3 2200°F STATIC RIG TESTS OF SILICON NITRIDE VANES 95
    4.3.1 THE TEST ASSEMBLY 95
    4.3.2 THE 2200°F TEST CYCLE 95
    4.3.3 TEST RESULTS 102
4.4 STATIC RIG MODIFICATION FOR 2500°F TESTS 113
4.5 STATIC RIG TESTS OF Si_3N_4 AND SiC VANES 115
    4.5.1 STATIC RIG PREPARATION 115
    4.5.2 PRELIMINARY TEST RESULTS 123
    4.5.3 TEST RESULTS AT 2500°F 126
4.6 FINAL STATIC RIG DEMONSTRATION OF Si_3N_4 STATOR VANES . . . 139
    4.6.1 STATIC RIG MODIFICATION 139
    4.6.2 CERAMIC STATOR VANE TEST SECTION 142
    4.6.3 STEADY-STATE PROFILE TESTS 142
    4.6.4 TRANSIENT THERMAL CYCLES 1-25 149
    4.6.5 TRANSIENT THERMAL CYCLES 26-60 155
    4.6.6 TRANSIENT THERMAL CYCLES 61-103 157
    4.6.7 SUMMARY OF FINAL 2500°F TESTING 165
4.7 FINAL HEAT TRANSFER AND STRESS ANALYSIS 170
    4.7.1 INTRODUCTION 170
    4.7.2 INPUT CONDITIONS 171
    4.7.3 THE AIRFOIL HEAT TRANSFER ANALYSIS 178
    4.7.4 THE AIRFOIL STRESS ANALYSIS 181

Section Page

SECTION 5 STATOR VANE ASSEMBLY FABRICATION 207

5.1 INTRODUCTION 207
5.2 NORTON SILICON NITRIDE 208
  5.2.1 PRELIMINARY BILLET MATERIAL 208
  5.2.2 HS130 Si_3N_4 MATERIAL AND COMPONENTS 208
  5.2.3 SECOND GENERATION DESIGN COMPONENTS 215
  5.2.4 THIRD GENERATION STATOR VANE ASSEMBLIES 216

5.3 NORTON SILICON CARBIDE 228
5.4 ENERGY RESEARCH CVD SILICON CARBIDE 229

SECTION 6 CONCLUSIONS AND RECOMMENDATIONS 231
6.1 CONCLUSIONS 231
6.2 RECOMMENDATIONS 232

LIST OF FIGURES

Figure Page

1-1 Westinghouse W251 Gas Turbine 2
1-2 Iterative Development Procedure for Industrial Gas Turbine Components 3
1-3 Conceptual Ceramic Turbine for Power Generation 4
1-4 DARPA Stationary Turbine Project - Iterative Development Plan 5
1-5 Stator Vane Development on Stationary Turbine Project 6

2-1 Three-Piece Stator Vane Schematic 10
2-2 First Row Stator Vane - Integral Version 10
2-3 Heat Transfer Coefficient Ratios as a Function of Time for a Row 1 Vane Emergency Shutdown Condition 11
2-4 Distribution of Maximum Heat Transfer Coefficients around Row 1 Vane for an Emergency Startup and Shutdown Condition 12
2-5 Two-Dimensional Finite Element Mesh for Solid Airfoil Section 13
2-6 Thermal Stress in a Vane 14
2-7 Stress History for Si_3N_4 Airfoils from 1950°F and 2500°F 15
2-8 Maximum Stresses in Solid Airfoil as a Function of Size 15
2-9 Temperature Contours in Solid Half-Size Si_3N_4 Airfoils 17
2-10 Stress Contours in Solid Half-Size Si_3N_4 Airfoils 17
2-11 Dimensions of Blunted Leading and Trailing Edges of Ceramic Airfoils 18
2-12 Thermal Quench Cylinder Coordinate System 19
2-13 Boundary Conditions - Gas Temperature and Film Coefficient 20
2-14 Temperature Decay and Maximum Transient Tensile Stress in the Axial Direction for Silicon Carbide Cylinders Cooled in Test Passage 21
2-15 Temperature Decay for a Thermocouple at Position No. 3 in Thermally Quenched Cylinders of SiC 21
2-16 Cylinder Models 23
2-17 Effect of Time on Temperature for Cylinder Thermal Quench Test 24
2-18 Development of Stress in Cylinder Thermal Quench Test 24

3-1 30 Mw Test Turbine Flow Path 25
3-2 Design Concept I 26
3-3 Design Concept II 28
3-4 Design Concept III 29
3-5 First Row Ceramic Stator Vane Assembly - Longitudinal View (First Generation Static Rig Test Configuration) 30
3-6 First Row Ceramic Stator Vane Assembly - Radial and Circumferential Views (First Generation Static Rig Test Configuration) 30

Figure Page

3-7 Ceramic Vane and Support Hardware Assembly 31

3-8 First Generation, First Row Ceramic Vane Assemblies with Airfoil, End Caps and Insulators - Systems 1 and 2 Provide Circumferential Locking 34

3-9 First Generation Ceramic Vane End Cap to Insulator Circumferential Locking Arrangement 34

3-10 First Generation Ceramic End Cap Configuration 35

3-11 First Generation Airfoil-to-End Cap Juncture - Compound Curvature Locking Concept 35

3-12 First Generation Ceramic Airfoil End Configuration 36

3-13 Loads and Interfaces 38

3-14 Cylindrical Contact Analogy for the Determination of Stresses Due to Tangentially Applied Tractive Loads on a Body with Compound Curvature 39

3-15 One-Dimensional Force Equilibrium Diagram for the Airfoil-End Cap Interface 39

3-16 The Effect of Friction on Maximum Contact Stress at the Airfoil-End Cap Interface 40

3-17 Interface Edge Loading Analysis Airfoil-End Cap 41

3-18 Startup Tensile Contact Stress at the Airfoil-End Cap Interface Showing the Effects of Parameter Variation 42

3-19 Shutdown Tensile Contact Stress at Vane/End Cap Interface Showing Effects of Parameter Variation 43

3-20 Critical Axial Radius vs Startup Coefficient of Friction at End Cap/Insulator Interface 45

3-21 Startup Tensile Contact Stress at the End Cap/Insulator Interface Showing Effects of Parameter Variation 45

3-22 Shutdown Tensile Contact Stress at the End Cap/Insulator Interface Showing the Effects of Parameter Variation 46

3-23 Circumferential Edge Loading Analysis of Hertzian Contact Stresses (Tensile) at Thick-Thin End Cap/Insulator Interlocks 47

3-24 Finite Element Geometry - End Cap With Torroidal Groove 48

3-25 Maximum Plate Stress in Outer End Cap Under Thermal Steady State Showing Groove Depth Effect and Adjustment for Asymmetry 49

3-26 Two-Dimensional Finite Element Mesh for Heat Transfer in the End Cap Sections AA, BB-CC-DD and EE 51

3-27 Steady-State Thermal Contour Representation Through End Cap Section AA 52

3-28 Steady-State Thermal Contour Representation Through End Cap Section CC 52

3-29 Thermal Contour Representation Through End Cap Section AA 5 Seconds After Shutdown 53

3-30 Thermal Contour Representation Through End Cap Section CC 5 Seconds After Shutdown 53

Figure Page

3-31 Thermal Contour Representation Through End Cap Section AA 60 Seconds After Shutdown 54
3-32 Thermal Contour Representation Through End Cap Section CC 60 Seconds After Shutdown 54
3-33 Thermal Stress Distribution in Ceramic End Caps Under Steady-State Conditions 56
3-34 Preliminary 1-D Radial Steady-State Conduction/ Convection Heat Transfer Analysis - Simplified Ceramic Vane Assembly Model and Temperature Profile 58
3-35 Preliminary 1-D Radial Steady-State Conduction/ Convection Heat Transfer Analysis - Effect of Insulator Thickness on Surface Temperature 58
3-36 Preliminary 1-D Radial Steady-State Conduction/ Convection Heat Transfer Analysis - Effect of Insulator Thickness on Temperature Gradients Within Components 59
3-37 Thermal Conductivity of End Cap, Typical Insulator and Shoe Materials 59
3-38 Kinematic Model of the Three-Piece Ceramic Vane Design with Support Structure 61
3-39 The Second Generation Ceramic Stator Vane Assembly Design 63
3-40 Vane Cross Section Showing Elliptical Contact Surface Projections for the Worst Contact Conditions at the Inner Airfoil/End Cap Interface 65
3-41 Startup Tensile Contact Stress at Airfoil/End Cap Interface Showing Effects of Parameter Variation 65
3-42 Shutdown Tensile Contact Stress at Airfoil/End Cap Interface Showing Effects of Parameter Variation 66
3-43 Circumferential Edge Loading Analysis of Hertzian Contact Stresses (Tensile) at Thick-Thin End Cap/ Insulator Interlocks 67
3-44 Second Generation Airfoil Cross Section at the End Cap Surface 67
3-45 Finite Element Model of Airfoil Section with Representative Stress Values (ksi) 68
3-46 Modified Finite Element Model Showing Principal Stresses (in ksi) and Selected Temperatures (in °F) 69
3-47 Initial and Boundary Conditions for End Cap Thermal Analysis (h = Btu hr^{-1} ft^{-2} °F, T = °F) 70
3-48 Calculated Variations in Heat Transfer Coefficients as a Function of Distance from the Leading Edge for the Airfoil Section at Mid-Height and the End Cap Surface 70
3-49 Three-Dimensional Element Model of the Second Generation Airfoil Under Equilibrium Conditions 71
3-50 Three-Dimensional Element Model of the End Cap Under Equlibirium Conditions 71

Figure Page

3-51 Temperature and Stress Distribution for Second Generation Design Airfoil 10 Seconds After Flameout from 2500°F Steady-State Gas Temperature (Section 7a) (h: High-Low) 72
3-52 Temperature and Stress Distributions for Airfoil Section 3 Ten Seconds After Flameout from 2500°F Steady-State Gas Temperature (h: High-Low) 72
3-53 Temperature and Stress Distribution for Airfoil Section 6A Ten Seconds After Flameout from 2500°F Steady-State Gas Temperature [(a) h: High-Low, (b) h: High-Low, (c) h: High-High)] 73
3-54 Stress Distribution in Airfoil Section 6a at 50 Seconds After Shutdown from 2500°F Steady-State Gas Temperature at 25°F/Sec 74
3-55 Temperature and Stress Distributions for End Cap Section 7e at 14 Seconds After Flameout from 2500°F Steady-State Gas Temperature (h: High-Low) 74
3-56 Temperature and Stress Distributions for End Cap Section 6e at 14 Seconds After Flameout from 2500°F Steady-State Gas Temperature (h: High-Low) 75
3-57 Temperature and Stress Distributions for End Cap Section 3 at 14 Seconds After Flameout from 2500°F Steady-State Gas Temperature (h: High-Low) 75
3-58 Stress Distribution during Cooling at 25°F/Sec from 2500°F Steady-State Gas Temperature in End Cap Section 7e After 58 Seconds 76
3-59 Deformations of the Airfoil/End Cap Contact Surfaces at Steady State and During Shutdown Transient 77
4-1 Modified Static Test Rig for 2200°F Test of Ceramic Vanes 82
4-2 The Static Rig for Testing Ceramic Stator Vanes at 2200 and 2500°F (Mitered Section is 42 inches in Diameter) 82
4-3 Mitered Section of Static Rig Showing Barrier Plate for the Installation of the Test Assembly 83
4-4 Mitered Section of the Static Rig with Test Assembly Installed 84
4-5 Hot Gas Duct for 2200°F Static Rig Test 84
4-6 Ceramic Stator Vane Assembly for Static Rig Testing at 2200°F 86
4-7 Instrumented Test Assembly for the 2200°F Static Rig Testing of Silicon Nitride Stator Vanes 86
4-8 Relation of Peak Ceramic Vane Temperature to Temperature Profile and Average Turbine Inlet Temperature 87
4-9 Shutdown from 2500°F to 950°F (Gas Temperature) in 2.0 Seconds 88
4-10 Shutdown from 2200°F to 950°F (Gas Temperature) in 2.0 Seconds 89

Figure Page

4-11 Effects of 100°F/Sec and 315°F/Sec Shutdown from 2500°F 89
4-12 Effect of 25°F/Sec Shutdown from 2500°F on Stresses Developed in Ceramic Vanes 90
4-13 Effect of Controlled Temperature Decay from 2500°F on Maximum Stress in Ceramic Airfoils 91
4-14 Effect of Step Function Temperature Decay from 2500°F on Maximum Stress Development in Ceramic Airfoils 91
4-15 Maximum Stress History with Respect to Time for Controlled Shutdown from 2500°F 92
4-16 Normal and Emergency Shutdown from Base-Load to No-Load Idle Conditions 93
4-17 Shutdown from Base-Load to No-Load Idle Condtiions (W501D) 93
4-18 Final Shutdown from Idle Temperature for Normal, Emergency and Full-Load Dump (W501D) 94
4-19 Silicon Nitride Stator Vanes Assembled with Support Structure for Test at 2200°F 96
4-20 Test Cycle for 2200°F Static Rig Testing of First Generation Silicon Nitride Vane Assemblies 97
4-21 Typical Cycles and Cyclic History of 2200°F Silicon Nitride Vane Tests 98
4-22 The Two-Dimensional Analytical Model 99
4-23 A Three-Dimensional Finite Element Plot for Heat Transfer and Stress Calculations for Silicon Nitride Vanes 99
4-24 Calculated Variations in Heat Transfer Coefficients at Mid-Height Surface Locations Around a Silicon Nitride Airfoil 100
4-25 Emergency Shutdown Ramp for Silicon Nitride Vane Test, 0.8 Simulation, 2200°F 101
4-26 Transient Stress Distribution on the Suction Side of Silicon Nitride Airfoils as a Result of Emergency Shutdown from 2225°F Peak Temperature 101
4-27 Transient Stress Distribution on the Pressure Side of Silicon Nitride Airfoils as a Result of Emergency Shutdown from 2225°F Peak Temperature 102
4-28 Temperature Profile for 2200°F Static Rig Tests - °F 103
4-29 Comparison of Temperature Transients as Measured by Downstream Control Thermocouples, Upstream Gas Thermocouple Rakes and the Radiation Pyrometer 103
4-30 Silicon Nitride Stator Vanes as Seen from View Port During 2200°F Tests in the Static Rig 104
4-31 Silicon Nitride Vanes in Static Rig Test Assembly at the Completion of 2200°F Tests 105
4-32 Ultraviolet Xyglo Photograph of Si_3N_4 Airfoil Showing Typical Crack Patterns after 2200°F Static Rig Tests (Suction Side of Airfoil)
4-33 Ultraviolet Xyglo Photograph of Typical Crack Pattern Development on the Pressure Side of Si_3N_4 Airfoil after 2200°F Static Rig Tests 106

Figure Page

4-34 Ultraviolet Xyglo Photograph of Failure Indications in Outer End Cap 6 After 2200°F Static Rig Tests 107
4-35 Ultraviolet Xyglo Photograph of Crack Pattern Development in Outer End Cap 1 after 2200°F Static Rig Tests 108
4-36 The Concave Surface View (Pressure Side) of a Typical Airfoil Section after Explosure to Hot Combustion Gases in the Static Test Rig at 2200°F Peak Test Temperature 109
4-37 The Convex Surface View (Suction Side) of a Typical Airfoil Section after Exposure to Hot Combustion Gases in the Static Rig at 2200°F Peak Test Temperature 110
4-38 Inside Surface of an Outer End Cap after Exposure to Hot Combustion Gases - Static Rig Test at 2200°F Peak Temperature 110
4-39 Typical Failure Indications in LAS Insulators as Seen from the End Cap/Insulator Interface 112
4-40 Plan View of the Static Rig for the 2500°F (1370°C) Test of Ceramic Vanes 113
4-41 Installation of Ceramic Duct in the Static Rig for Tests at 2500°F Peak Temperature 114
4-42 Location of Ceramic Components in 2500°F (1370°C) Test Assembly 116
4-43 Typical Insulator Failures in Cervit C-140 LAS Material (2200°F Test) 116
4-44 One-Dimensional Radial Conduction/Convection/Radiation Heat Transfer Model, Steady-State Condition 117
4-45 Two-Dimensional Finite Element Heat Transfer Model 120
4-46 Gas/Air Temperature versus Time Response for End Cap/Insulator Combination 120
4-47 Convection Coefficient versus Time Response for End Cap/Insulator Combination 121
4-48 Insulator Hot Gas Transient Temperature Response for LAS Material 122
4-49 Insulator Hot Gas Transient Temperature Response for Hot Pressed Si_3N_4 Material 122
4-50 Insulator Two-Dimensional Stress Model 124
4-51 Insulator Hot Gas Two-Dimensional In-Plane Maximum Stress Response of Hot Pressed Si_3N_4 Material 124
4-52 Insulator Hot Gas Two-Dimensional In-Plane Maximum Stress Response of LAS Material 125
4-53 Gas Temperature Profile at 1200°F (Idle) 127
4-54 Gas Temperature Profile at 1800°F 127
4-55 Gas Temperature Profiel at 2300°F 128
4-56 Extrapolated Gas Temperature Profile at 2500°F 128
4-57 Typical Cycle for 2500°F (1370°C) Testing Based on Pryometer Response 129
4-58 Combustor Failure from 2500°F Static Rig Tests of SiC and Si_3N_4 Vanes 131

Figure Page

4-59 Silicon Nitride (Left) and Silicon Carbide (Right) Stator Vane Assemblies After 2500°F Static Rig Test (Five Cycles) 131

4-60 Ceramic Mixer-Inlet Side, 2500°F Static Rig Test 133

4-61 Ceramic Mixer-Outlet Side, 2500°F Static Rig Test 133

4-62 Typical Si_3N_4 Stator Vane Assembly After 2500°F Test (Cleaned) 134

4-63 Silicon Nitride Airfoil with Thermal Cracks After 2500°F Test 134

4-64 Silicon Nitride Inner End Cap 2 After 2500°F Test 135

4-65 Silicon Nitride Inner End Cap 4 After Static Rig Test at 2500°F 136

4-66 Silicon Carbide Outer End Cap 5 After Static Rig Test at 2500°F 136

4-67 Silicon Carbide Inner End Cap 6 After Static Rig Test at 2500°F 137

4-68 Insulators from 2500°F Static Rig Test (Five Cycles) 138

4-69 Water Cooled Static Rig for 2500°F Testing of Ceramic Vanes 140

4-70 New Combustor with Additional Secondary Wall Cooling 140

4-71 Water-Cooled Exhaust Duct 141

4-72 Water Spray-Cooled Mixer Section 141

4-73 Longitudinal View of the Ceramic Vane - 2500°F Static Rig Test Fixture 143

4-74 Third Generation Stator Vane Assembly Components 143

4-75 Hot Pressed Silicon Nitride Stator Vanes (Norton NC132) for 2500°F Static Rig Testing - Airfoils 3 and 6 (from left) Were Preoxided 103 Hours in Alumina Lined Muffle Furnace at 2500°F (Static Air) 144

4-76 2500°F Static Rig Test Assembly in Place Showing Aspirating Thermocouple Rakes 144

4-77 Inner and Outer Boron Nitride Insulators for 2500°F Static Rig 146

4-78 Gas Temperature Profile Under Steady-State Conditions at 1400°F 146

4-79 Gas Temperature Profile Under Steady-State Conditions at 2000°F (Mid-Load Temperature) 147

4-80 Gas Temperature Profile Under Steady-State Conditions at 2300°F (Thermocouple Rake Temperature Limit) 147

4-81 Extrapolated Gas Temperature Profile Under Steady-State Conditions at 2500°F (Peak Load Temperature) 148

4-82 Gas Temperature vs Percent Airfoil Height (Leading Edge) for Extrapolation of Peak Load Gas Temperature Profile 148

4-83 Combustor Wall Temperature Under Peak Load Conditions at 2500°F 150

4-84 Planned Stator Vane Transient Thermal Cycle for 2500°F Tests 150

4-85 Typical Transient Thermal Cycles as Recorded from Static Rig Testing at 2500°F (Cycles 1-25 and 26-60, Respectively) 151

Figure Page

4-86 Stator Vane Test Assembly as It Appeared in the Static Rig After 25 Cycles of Testing to 2500°F (View from Downstream Location) 151
4-87 Typical Example of Airfoil/End Cap Edge Loading Resulting from the Shift in Outer End Cap Position (Cycles 1-25, 2500°F Static Rig Test) 152
4-88 Illustration of Outer End Cap Position Shift During Static Rig Tests at 2500°F (Cycles 1-25) 152
4-89 Silicon Nitride Stator Vane Components as They Appeared After 25 Cycles of Testing in the Static Rig at 2500°F 153
4-90 Failure Indications in Silicon Nitride Stator Vane Components After 25 Cycles of Transient Testing in the Static Rig at 2500°F 154
4-91 Typical Example of Chipping at the Inner End Cap/Airfoil Tenon Interface (Cycles 1-25, Static Rig Test at 2500°) 154
4-92 Failure in Outer End Cap 1 from 2500°F Static Rig Test (Cycles 1-25) 155
4-93 Silicon Nitride Stator Vanes Installed in Static Rig for Continuation of 2500°F Tests (Airfoils 3 and 6 Were Preoxidized for 100 hours in an Alumina-Lined Muffle Furnace at 2500°F). 156
4-94 Failure Indications in Silicon Nitride Stator Vane Airfoils (Cycles 26-60, Static Rig Testing at 2500°F) 158
4-95 Trailing Edge View of Si_3N_4 Components after 2500°F Static Rig Test (Cycles 26-60) 158
4-96 Stator Vane Components and Insulators from Static Rig Testing at 2500°F (Cycles 26-60) 159
4-97 Contact Areas on Outer Airfoil Tenons Defined Along Machine Chatter Marks 159
4-98 Ultraviolet Macrographs of Airfoil 5 Showing Cracks as Revealed by Dye Penetrant 160
4-99 Ultraviolet Macrographs of Vane 6 (preoxidized) Showing Cracks as Revealed by Dye Penetrant 160
4-100 Silicon Nitride Stator Vanes Assembled for Test at 2500°F (Cycles 61-103) (White Dots Indicate Pyrometer Target Areas) 161
4-101 Gas Temperature Profile at 1400°F Peak (Cycles 61-103) 161
4-102 Gas Temperature Profile at 2000°F Peak (Cycles 61-103) 162
4-103 Gas Temperature Profile at 2300°F Peak (Cycles 61-103) 162
4-104 Extrapolated Gas Temperature Profile for 2500°F Peak (Cycles 61-103) 163
4-105 Gas Temperature Distribution Along Airfoil Leading Edge with Respect to Time of Shutdown 164
4-106 Peak Gas Temperature During Controlled Shutdown Transient as Measured by the Supervisory Thermocouple (Cycles 61-103 164

Figure Page

4-107 Ceramic Vane Temperature Record (Pyrometer Measurement) for Final 43 Cycles of Static Rig Testing at 2500°F (Cycles 61-103) 165
4-108 Static Rig Test Fixture with Ceramic Vanes in Place at the Conclusion of 2500°F Testing - Pressure Side View (Cycles 61-103) 166
4-109 Static Rig Test Fixture with Ceramic Vane Assemblies in Place at the Conclusion of 2500°F Testing - Suction Side View (Cycles 61-103)
4-110 Failure Indications in Airfoil 8 as Seen from Pressure and Suction Sides (Cycles 61-103, 2500°F Static Rig Test) 167
4-111 Fracture Origin in Fillet Radius of Airfoil 8 168
4-112 The Three-Dimensional Finite Element Model of the Parallel-Sided, Nontwisted Airfoil Section (Generation I) Used for the Final Heat Transfer - Stress Analysis of Ceramic Vanes 172
4-113 A Comparison of Airfoil Section Geometries, the Parallel-Sided, Nontwisted Section (Generation I) Analyzed and the Tapered-Twisted Section (Generation III) 172
4-114 Thermoelastic Properties of Hot Pressed Si_3N_4 (Norton NC132) 173
4-115 Heat Transfer Coefficients at the Airfoil Surface 173
4-116 Three Conditions of Transient Thermal Shutdown 174
4-117 Radial Gas Temperature Profiles for the Cooled-Wall Combustor 174
4-118 Radial Gas Temperature Profiles for the W251 Production Turbine Combustor 175
4-119 Extrapolated Gas Temperature Profiles for Three Combustor Types at 2500°F Peak 175
4-120 Gas Temperature Profile Model for Production-Type Combustor at 2500°F Peak 176
4-121 Gas Temperature Outer Profile Model for Cooled-Wall Combustor at 2500°F Peak 176
4-122 Gas Temperature Inner Profile Model for Cooled-Wall Combustor at 2500°F Peak 177
4-123 Comparison of Inner and Outer Gas Temperature Profile Models for the Cooled-Wall Combustor 177
4-124 Comparison of Inner-Half Cooled-Wall Combustor Profile with Pyrometer Temperature Measurement from 2500°F Test 178
4-125 Comparison of Outer-Half Cooled-Wall Combustor Profile with Pyrometer Temperature Measurement from 2500°F Test 179
4-126 Airfoil Temperature Response for a Linear Shutdown Transient at 25°F/sec Using the Uniform Gas Temperature Profile 179
4-127 The Effect of the Production Combustor Gas Temperature Profile on Airfoil Temperature Response for a Linear Shutdown Transient at 25°F/sec 180

Figure Page

4-128 The Effect of the Cooled-Wall Inner-Half Gas Temperature Profile on Airfoil Temperature Response for a Linear Shutdown Transient at 25°F/sec 180
4-129 The Effect of the Cooled-Wall Outer-Half Combustor Profile on Airfoil Temperature Response for a Linear Shutdown Transient at 25°F/sec 181
4-130 The Effect of a Uniform Combustor Profile on Airfoil Temperature Response for the Controlled, Nonlinear, Shutdown Transient of the 2500°F Static Rig Test 182
4-131 The Effect of the Production Combustor Gas Temperature Profile on Airfoil Temperature Response for the Controlled, Nonlinear Shutdown Transient of the 2500°F Static Rig Test 182
4-132 The Effect of the Cooled-Wall Inner-Half Gas Temperature Profile on Airfoil Temperature Response for the Controlled, Nonlinear Shutdown Transient of the 2500°F Static Rig Test 183
4-133 The Effect of the Cooled-Wall Inner-Half Gas Temperature Profile on Airfoil Temperature Response for an Emergency Shutdown (Fuel Trip) Transient 183
4-134 A Comparison of the Analytical and 2500°F Static Rig Test Results for the Cooled-Wall Inner-Half Gas Temperature Profile and the Controlled Nonlinear Shutdown Transient of the 2500°F Static Rig Test 184
4-135 Stress and Temperature Distributions in a Ceramic Airfoil Resulting from Steady-State Condition at 2500°F and the First Ramp of the Controlled, Nonlinear Shutdown Transient and the Cooled-Wall Inner-Half Gas Temperature Profile 186
4-136 The State of Stress in a Plate Analogy for the Production Combustor Gas Temperature Profile Under Steady-State Conditions 187
4-137 Airfoil Section Steady-State Stress and Temperature Distributions Resulting from the Production Combustor Gas Temperature Profile 188
4-138 Airfoil Section Steady-State Stress and Temperature Distribtuions Resulting from the Cooled-Wall Inner-Half Combustor Gas Temperature Profile 189
4-139 The State of Stress in a Heated Strip Analogy for the Cooled-Wall Outer-Half Gas Temperature Profile 189
4-140 Airfoil Section Steady-State Stress and Temperature Distributions Resulting from the Cooled-Wall Outer-Half Gas Temperature Profile 191
4-141 The Effect of a Linear Shutdown Transient on the State of Stress and Temperature in an Airfoil Section Resulting from a Uniform Gas Temperature Profile 193
4-142 The Effect of a Linear Shutdown Transient on the State of Stress and Temperature in an Airfoil Section Resulting from the Cooled-Wall Inner-Half Gas Temperature Profile 194

Figure Page

4-143 The Effect of a Linear Shutdown Transient on the Development of Maximum Principal Stress in an Airfoil Section Resulting from a Uniform Gas Temperature Profile 196

4-144 The Effect of a Linear Shutdown Transient on the Development of Maximum Principal Stress in an Airfoil Section Resulting from the Production Combustor Gas Temperature Profile 196

4-145 The Effect of a Linear Shutdown Transient on the Development of Maximum Principal Stress in an Airfoil Section Resulting from the Cooled-Wall/Inner-Half Combustor Gas Temperature Profile 197

4-146 The Effect of the Nonlinear, Controlled Shutdown Transient on the Development of Maximum Principal Stress in an Airfoil Section from Cases B1 - the Uniform, B2 - The Production Combustor, and B3 - The Cooled-Wall Inner-Half Combustor Gas Temperature Profile 198

4-147 The Effect of an Emergency Shutdown Transient on the Development of Maximum Principal Stress in an Airfoil Section Resulting from the Cooled-Wall/Inner-Half Combustor Gas Temperature Profile 199

4-148 The Effect of a Linear Shutdown Transient on Stress and Temperature Gradients in an Airfoil Section at Mid-Chord (50% Vane Height) Resulting from a Uniform Gas Temperature 199

4-149 The Effect of a Uniform Shutdown Transient on Stress and Temperature Gradients in an Airfoil Section at 41% Vane Height Resulting from the Cooled-Wall/Inner-Half Combustor Gas Temperature Profile 200

4-150 The Maximum Principal Stress and Temperature Gradients Developed on the Pressure Side of a Ceramic Airfoil as a Result of a Linear Shutdown Transient in a Cooled-Wall/Inner-Half Combustor Gas Temperature Profile 200

4-151 The Maximum Principal Stress and Temperature Gradients in an Airfoil Section Developed as a Result of a Linear Shutdown Transient with the Production (Hot Wall) Combustor Gas Temperature Profile 201

4-152 The Maximum Principal Stress and Temperature Gradients in an Airfoil Section Developed as a Result of a Linear Shutdown Transient with the Cooled-Wall/Inner-Half Combustor Gas Temperature Profile 201

4-153 Maximum Principal Stress and Temperature Gradients in an Airfoil Section Developed as a Result of the Nonlinear, Controlled Shutdown with the Cooled-Wall/Inner-Half Combustor Gas Temperature Profile

Figure Page

4-154 Maximum Principal Stress and Temperature Gradients in an Airfoil Section Developed as a Result of an Emergency Shutdown Transient with the Cooled-Wall/Inner-Half Combustor Gas Temperature Profile 203
4-155 Stress-Strain Data for Norton Silicon Nitride (NC132) Compared with Calculated Pseudo-Elastic Properties 203
4-156 Airfoil Tensile Strength Comparison with Billet Tensile Property Data 204
4-157 Tensile Strength of Airfoils 4 and 5 as a Function of Temperature 204
4-158 Airfoil Tensile Strength and Performance Summary 206
5-1 Airfoil Blanks Machined from HS130 Si_3N_4 by Norton Company 209
5-2 Major Steps in the Machining of the Airfoil 210
5-3 Steps in the Grinding of an End Cap 210
5-4 First-Generation Stator Vane Assemblies as Supplied by Norton from HS130 Silicon Nitride 211
5-5 "Xyglo" Photograph of Two Machined Airfoils Showing Surface Scratches and a Crack on the Trailing Edge of Airfoil 19 212
5-6 "Xyglo" Photograph of End Cap 27 Irregularities Showing Scratches Inside the Cavity and Surface 213
5-7 Ultrasonic Scan of an End Cap Indicating Low Density Inclusion (Large Peaks Are Reflections from Top and Bottom Surfaces) 214
5-8 Second Generation Silicon Carbide (Left) and Silicon Nitride (Right) Stator Vane Assemblies 216
5-9 Tapered-Twised Airfoil Drawing Identifying the Blend Radius and Trailing Edge Deviation 218
5-10 Third Generation Stator Vane Assembly Components 218
5-11 Sectioned Plastic Cast of Tapered-Twisted Airfoil Blank 220
5-12 Section by Section Airfoil Inspection Record 221
5-13 Airfoil Section Comparison Showing Typical Twist 222
5-14 Effect of Airfoil Angularity Machining Error 223
5-15 Correct End Cap to End Cap Orientation Resulting from Proper Airfoil Tenon Angularity 223
5-16 Blueing-Powder Display of Machine Chatter on Airfoil Tenon Surface 224
5-17 Airfoil Processing 225
5-18 End Cap Processing 227
5-19 Energy Research CVD Silicon Carbide Hollow Vane 230

LIST OF TABLES

Table		Page
2-1	COMPARISON OF Si_3N_4 PROPERTY DATA	16
4-1	INSULATOR MATERIAL STRESS COMPARISON	118
4-2	END CAP STRESSES FOR VARIOUS INSULATOR MATERIALS	119
4-3	A COMPARISON OF STATIC RIG AND ANALYTICAL HEAT TRANSFER RESULTS	184
4-4	STEADY-STATE STRESSES IN AIRFOIL SECTIONS (psi)	192
4-5	TRANSIENT THERMAL STRESS IN AIRFOIL SECTIONS	195
4-6	STATIC RIG TEST AIRFOIL BILLET UNOXIDIZED FLEXURAL STRENGTH (ROOM TEMPERATURE) (NORTON Co., 4 PT LOADING)	205

FOREWORD

The Stationary Gas Turbine Project represents the Westinghouse contribution to the Defense Advanced Research Project Agency (DARPA) sponsored "Brittle Material Design, High Temperature Turbine" program, Order Number 1849, Contract Number DAAG-46-71-C-0162.

The final report is presented in four volumes as follows:

Volume I - Program Summary

Volume II - Ceramic Stator Vane Development

Volume III - Rotor Blade Development and Turbine Modification

Volume IV - Materials Technology

Final results of static rig testing and analysis for the tenth semiannual report period are included as part of this final report which represents a comprehensive project review summarizing the activities from July 1, 1971 to June 30, 1976.

Westinghouse performed this work under subcontract to the Ford Motor Company, prime contractor for the Defense Advanced Research Project Agency. The Army Material and Mechanics Research Center (AMMRC) at Watertown Arsenal, Watertown, Massachusetts, served as Program Monitor for DARPA.

The program's overall Principal Investigator was Mr. A. F. McLean, who also served as Program Manager for the Ford Vehicular Turbine Project.

Dr. R. J. Bratton was Principal Investigator and Program Manager for Westinghouse. Mr. D. G. Miller served as Project Engineer. Mr. A. N. Holden, now deceased, functioned as Project Manager at Westinghouse Generation Systems Division from July 1, 1971 to May 1, 1975. Mr. G. Levari succeeded Mr. Holden with Mr. C. R. Booher, Jr, accepting responsibility for design, analysis and rig testing for the Division at that time.

Westinghouse wishes to acknowledge the efforts of the following personnel who contributed to the program:

1. Dr. Maurice J. Sinnott who conceived and started the program when he was at DARPA in 1971.

2. DARPA - for support of the program. Dr. E. Van Reuth and Dr. M. Stickley for their interest and support.

3. AMMRC - for monitoring the program. Dr. E. S. Wright, who replaced Dr. A. E. Gorum (presently retired) as Technical Monitor, and Drs. R. N. Katz, E.N. Lenoe and H. Priest.

4. Ford Motor Co. - A. F. McLean, T. W. McLaughlin, E. A. Fisher, P. Berry, R. R. Baker and A. Paluszny.

The final report was prepared and edited by D. G. Miller and R. J. Bratton with editing assistance from E. J. Phillips. Contributions to the final report were made by C. R. Booher, Jr., S. C. Singhal, F. F. Lange, W. Van Buren and E. S. Diaz.

Other Westinghouse and former Westinghouse employees who contributed to the technical program include:

Westinghouse Generation Systems Division

J. Allen, G. W. Bauserman, D. D. Lawthers, L. Kish, F. Laus, S. D. Leshnoff, S. Mumford, T. J. Rahaim, J. D. Roughgarden, S. C. Sanday, R. J. Schaller, C. E. Seglem, E. J. Stenowoj, J. P. Smed, L. C. Szema, S. Twiss, E. H. Wiler, D. D. Wood

Westinghouse R&D Center

D. Boes, W. C. Frazier, R. Kossowsky, S. Y. Lee, C. Visser, J. H. White, W. E. Young, S. Gabrielse, D. E. Harrison

This final report is dedicated to A. N. Holden.

SECTION 1

INTRODUCTION

The "Brittle Materials Design - High Temperature Gas Turbine" program was formulated under the auspices of the Defense Advanced Research Projects Agency (DARPA) of the Department of Defense (DOD) to demonstrate the use of brittle material design concepts in the successful application of ceramics as structural components in high temperature gas turbines. The talents of the Ford Motor Company and Westinghouse, as prime and subcontractor, respectively, were directed toward the development of a vehicular ceramic turbine (Ford) and a ceramic stator vane for a large stationary gas turbine (Westinghouse). The Army Materials and Mechanics Research Center (AMMRC) served as technical monitor for DARPA.

The five-year performance period of the Westinghouse Stationary Gas Turbine Project, July 1, 1971 through June 30, 1976, is summarized in Volume I, "The Program Summary" of this report. Here in Volume II, "High Temperature Stationary Gas Turbine - Ceramic Stator Vane Development," the engineering aspects of ceramic stator vane design, analysis, fabrication, testing, and verification are described in a comprehensive manner. A three-piece stator vane with all supporting structure for the inlet, first stage of a Westinghouse W251 stationary gas turbine (Figure 1-1) eventually evolved. After the development of a fully functional test facility, performance was evaluated under cyclic, controlled conditions at 0.8 turbine simulation (8 atmospheres pressure rather than 10.5 atmospheres as experienced in a turbine operating in the peaking power mode) in an instrumented static rig. The results of static rig testing at 2200 and 2500° were assessed in terms of failure analysis, relying heavily upon three-dimensional stress analyses.

Figure 1-2 is reproduced from Volume I to emphasize the iterative development of ceramic components for industrial gas turbines as identified in Figure 1-3. Component development and material technology follow parallel but interacting paths to provide the coordination for fabrication, static-rig testing and final demonstration in the overall project plan. Failure analysis with design modification, further analysis and material improvement forms the iterative loop required for successful application.

Overall program objectives, as originally proposed and finally accomplished, are illustrated in Figure 1-4. Final rotor blade design

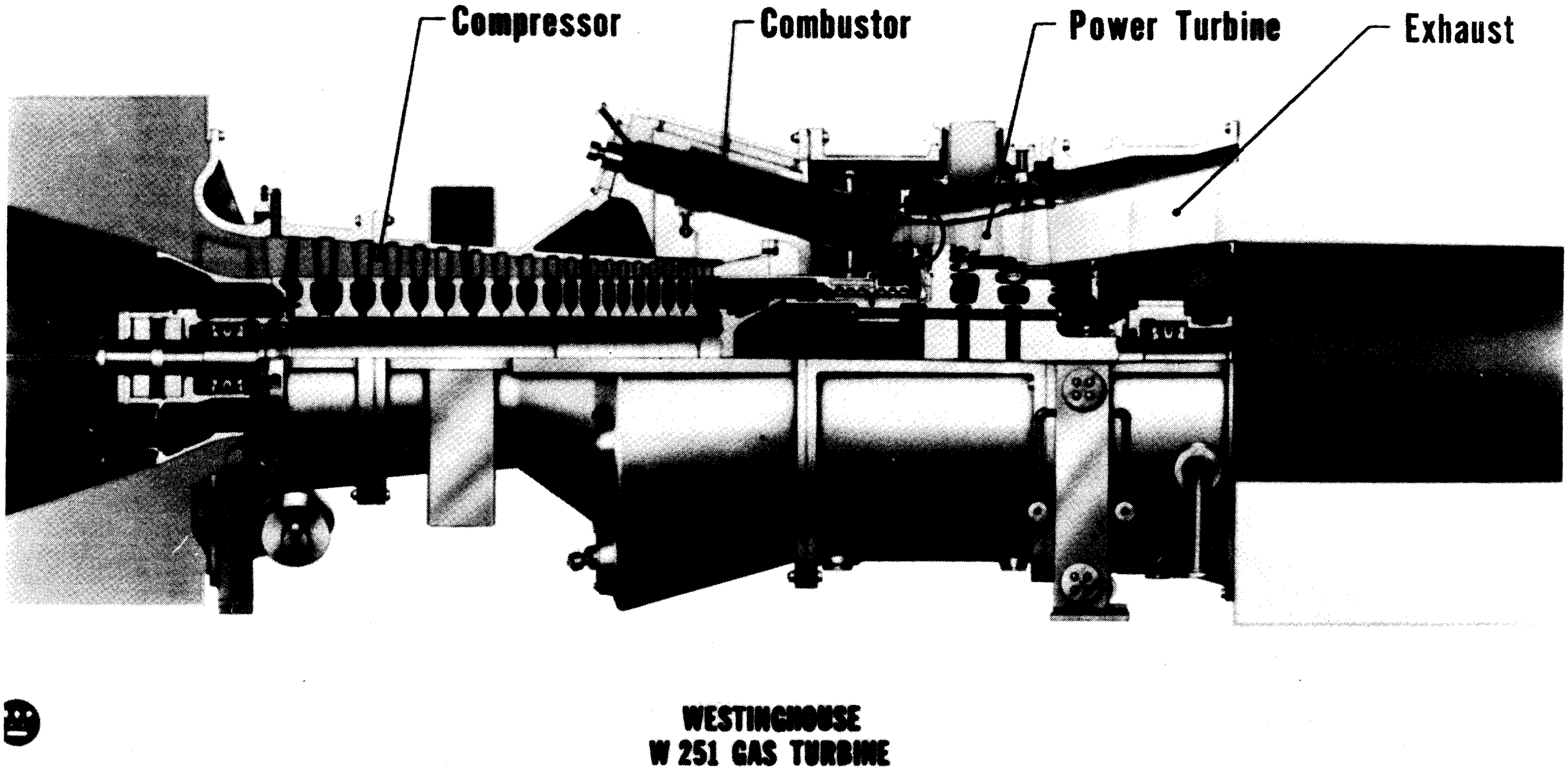
Compressor
Combustor
Power Turbine
Exhaust
WESTINGHOUSE
W 251 GAS TURBINE

Figure 1-1. Westinghouse W251 Gas Turbine

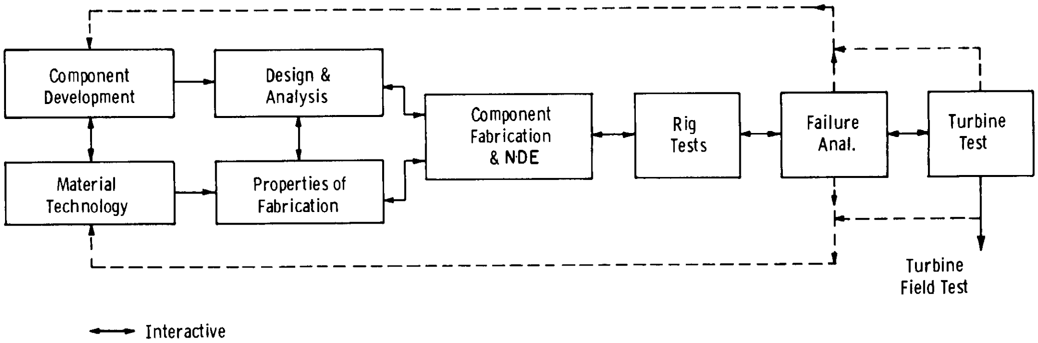
Component Development
Design & Analysis
Material Technology
Properties of Fabrication
Component Fabrication & NDE
Rig Tests
Failure Anal.
Turbine Test
Turbine Field Test
Interactive

Figure 1-2. Iterative Development Procedure for Industrial Gas Turbine Components

and computer simulation were delayed, then terminated in 1973 to permit full concentration of effort on the formidable tasks of ceramic vane development and static rig construction. The 30 megawatt turbine demonstration was also delayed and terminated when it became obvious that the rapidly escalating costs of an advanced turbine rig conversion and the need for additional verification of stator vane performance in the static rig placed this task beyond a reasonable scope of funding within the designated period of performance (5 years).

All of the essential elements of the ceramic stator vane development appear in Figure 1-5. The design process with appropriate analysis proceeded logically from the preliminary stages, through Vane Designs I and II to the final third generation, three-piece stator vane assembly with tapered-twisted airfoil. Component fabrication had to follow a parallel rather than a subsequent or series route in many cases, anticipating the design because of the long lead time required to meet the static rig test specifications as scheduled. Fabrication processes were developed as part of component manufacture, thus complicating the procedure. The second generation airfoil, for example, had to be committed to procurement before analysis disproved design viability. The static

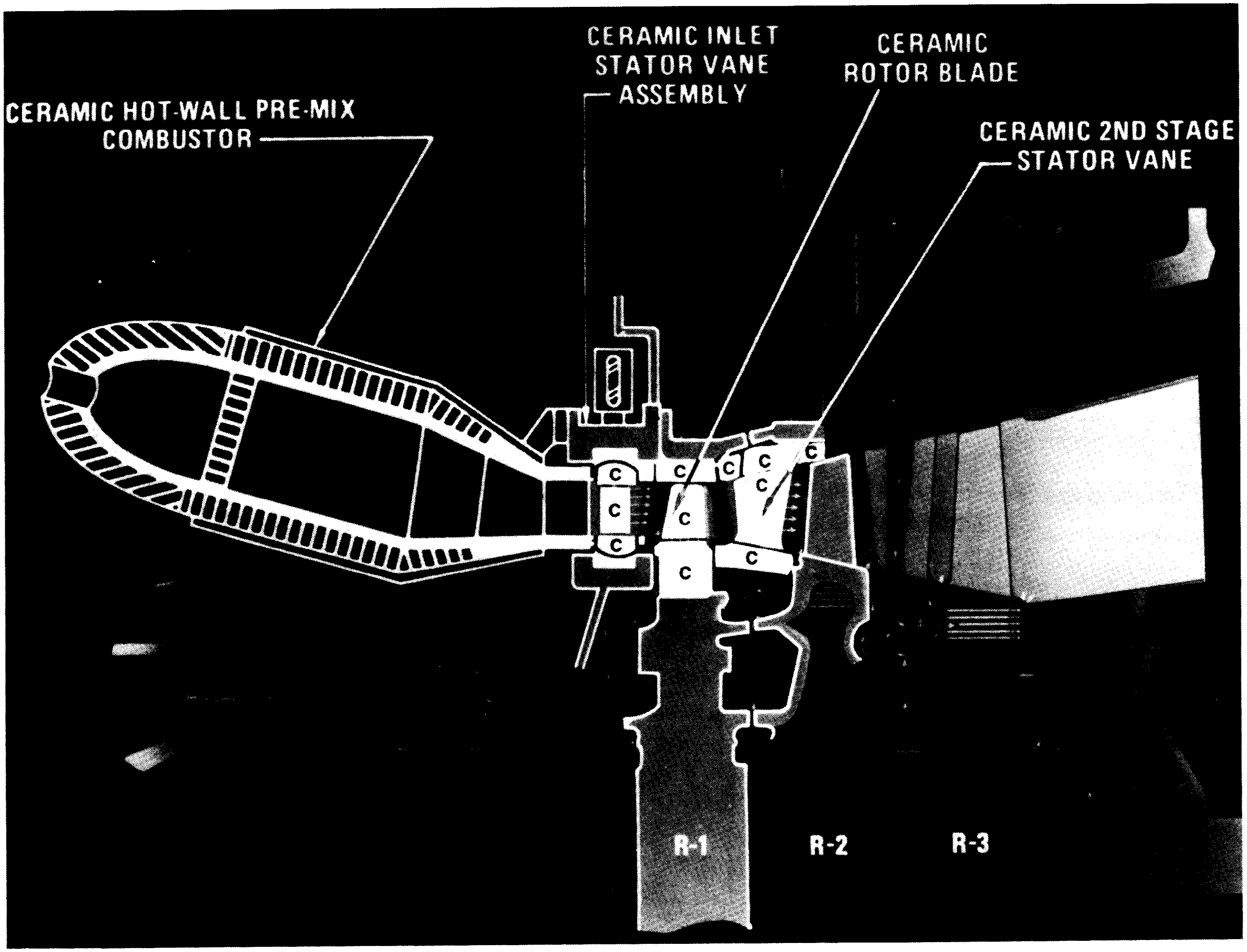
CERAMIC INLET
STATOR VANE
ASSEMBLY
CERAMIC
ROTOR BLADE
CERAMIC HOT-WALL PRE-MIX
COMBUSTOR
CERAMIC 2ND STAGE
STATOR VANE
C
C
C
C
C
C
C
C
C
C
C
C
R-1
R-2
R-3

Figure 1-3 Conceptual Ceramic Turbine for Power Generation

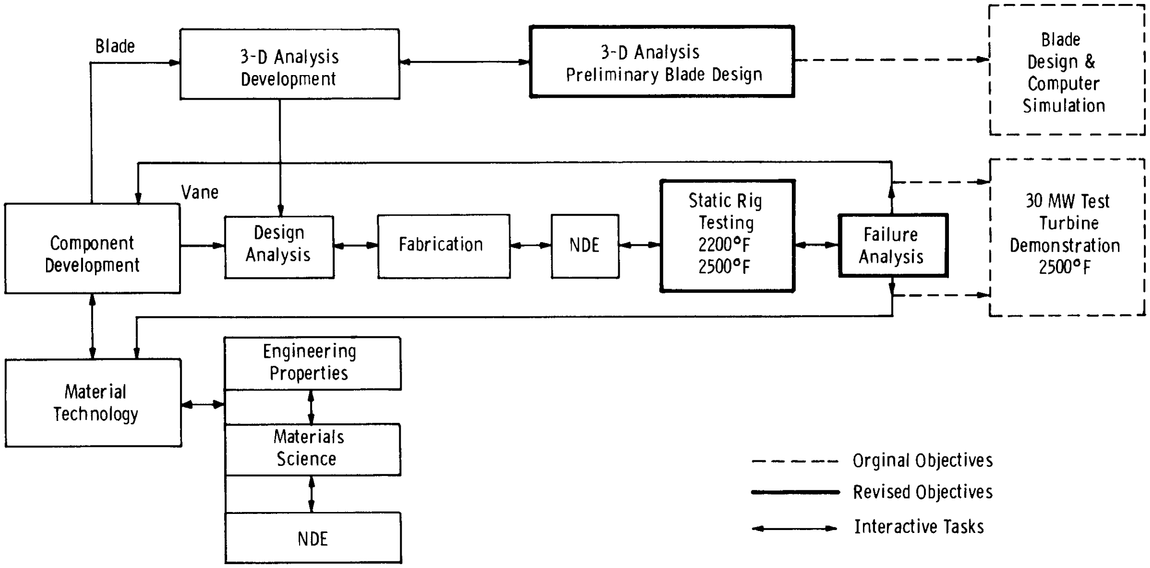
Blade
3-D Analysis Development
3-D Analysis Preliminary Blade Design
Blade Design & Computer Simulation
Vane
Component Development
Design Analysis
Fabrication
NDE
Static Rig Testing 2200°F 2500°F
Failure Analysis
30 MW Test Turbine Demonstration 2500°F
Material Technology
Engineering Properties
Materials Science
NDE
Orginal Objectives
Revised Objectives
Interactive Tasks

Figure 1-4. DARPA Stationary Turbine Project - Iterative Development Plan

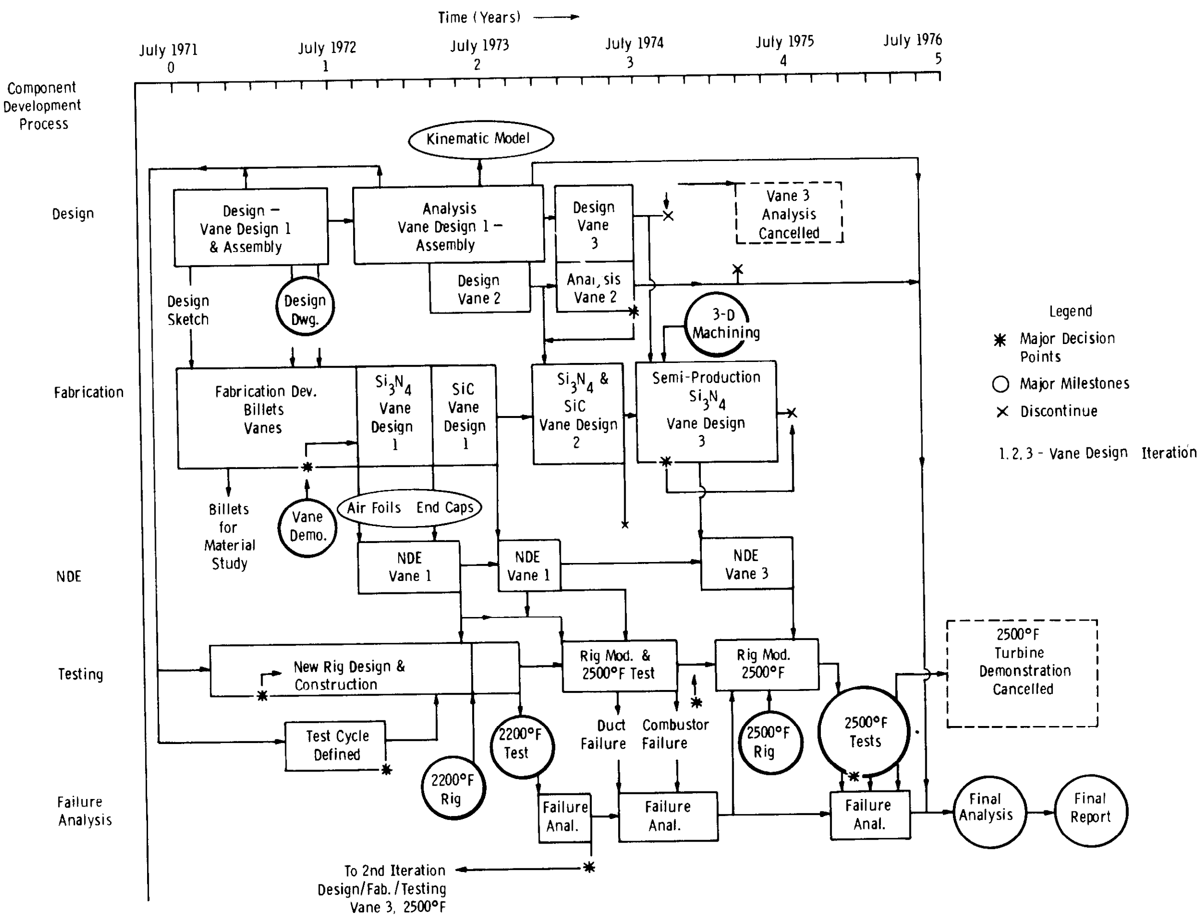
Time (Years)
July 1971
0
July 1972
1
July 1973
2
July 1974
3
July 1975
4
July 1976
5
Component Development Process
Design
Fabrication
NDE
Testing
Failure Analysis
Kinematic Model
Design – Vane Design 1 & Assembly
Analysis Vane Design 1 – Assembly
Design Vane 3
Vane 3 Analysis Cancelled
Design Vane 2
Anal,sis Vane 2
Design Sketch
Design Dwg.
3-D Machining
Fabrication Dev. Billets Vanes
Si_3N_4 Vane Design 1
SiC Vane Design 1
Si_3N_4 & SiC Vane Design 2
Semi-Production Si_3N_4 Vane Design 3
Billets for Material Study
Vane Demo.
Air Foils
End Caps
NDE Vane 1
NDE Vane 1
NDE Vane 3
New Rig Design & Construction
Rig Mod. & 2500°F Test
Rig Mod. 2500°F
2500°F Turbine Demonstration Cancelled
Test Cycle Defined
2200°F Test
2200°F Rig
Duct Failure
Combustor Failure
2500°F Rig
2500°F Tests
Failure Anal.
Failure Anal.
Failure Anal.
Final Analysis
Final Report
To 2nd Iteration Design/Fab./Testing Vane 3, 2500°F
Legend
✱ Major Decision Points
○ Major Milestones
× Discontinue
1, 2, 3 - Vane Design Iteration

Figure 1-5. Stator Vane Development on Stationary Turbine Project

rig test facility planned as a simple modification of an existing rig became a dynamic development activity coincident with the design and fabrication tasks. Indeed, the static rig requirement to test at 2500°F became the critical element in the project plan. Only once, in the final phases of the program when the vendor failed to deliver acceptable third generation hardware on time, was a critical delay experienced for a reason other than static rig availability.

Although the total effort was directed toward high service temperatures to increase power and efficiency, plans did not attempt to achieve specific levels of improved performance in either the static rig tests or an actual test turbine. The test cycle sequence, i.e., 100 cycles of peak load service at a maximum inlet temperature of 2500°F in a controlled shutdown mode, was selected to establish realistic boundary conditions for the demonstration of first stage stator vanes using the best commercial materials available. The boundary conditions thus established also served as a design constraint in the development of rotor blades as well as the stator vane components.

SECTION 2

PRELIMINARY DESIGN AND ANALYSIS

2.1 DESIGN

The original program proposal contained a conceptual version of a three-piece stator vane design with provisions for an integral modification representing a similar configuration. Both are illustrated in Figures 2-1 and 2-2. These versions mark the threshold of the design study. The three-piece design was selected because of its geometric simplicity and compatibility with existing turbine design technology. The first stage stator row was amenable to a simple supported vane structure that utilized spring loading for stability. The conventional use of inner and outer support rings at the inlet location of large stationary gas turbines made this possible and precluded the use of cantilevered vanes as dictated downstream at subsequent later stage locations.

Other advantages are obvious and in keeping with brittle material design criteria. For example, the introduction of interfaces minimizes stress concentrations. By separating airfoil from shrouds, highly stressed regions which result from thermal responses to abrupt changes in cross section are eliminated. In the proposed design, strain is accommodated, relative motion is encouraged and better temperature uniformity is ensured in elements that can be manufactured using two- and three-dimensional tracer grinding techniques.

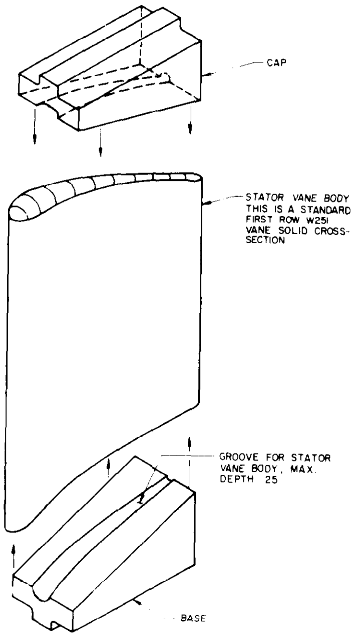
CAP
STATOR VANE BODY THIS IS A STANDARD FIRST ROW W251 VANE SOLID CROSS-SECTION
GROOVE FOR STATOR VANE BODY, MAX. DEPTH 25
BASE

Figure 2-1. Three-Piece Stator Vane Schematic

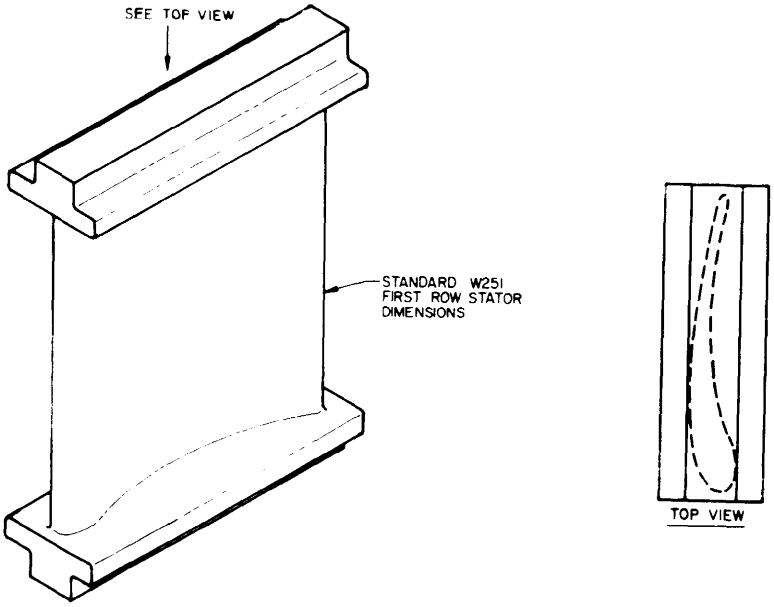
SEE TOP VIEW
STANDARD W251 FIRST ROW STATOR DIMENSIONS
TOP VIEW

Figure 2-2. First Row Stator Vane - Integral Version

2.2 ANALYSIS

Having accepted a generalized vane configuration, a preliminary series of two-dimensional analyses were performed to determine the temperature and stress distributions in the airfoil section of a W251 (30 Megawatt) size, first stage stator vane manufactured from a ceramic material.(1) The transient, thermally-induced tensile stresses were computed in both the cross-sectional plane and the out-of-plane directions of the airfoil since ceramic materials are weakest in the tensile mode. Silicon carbide vanes were analyzed in both hollow and solid cross section because a CVD process had been proposed to develop a hollow silicon carbide airfoil. Silicon nitride was analyzed in solid cross section only. The thermal boundary conditions were established from earlier design programs as verified by test turbine data. Typical values of the heat transfer coefficient, h*, as a function of time during emergency shutdown are given in Figure 2-3. Figure 2-4 establishes the distribution of heat transfer coefficients, h, on the surface of the airfoil. The temperature distributions in the cross-sectional plane were determined by a two-dimensional finite difference program, using the previous temperature solution for each time frame. Out-of-plane tensile stresses were computed by numerical integration from the temperature distribution.

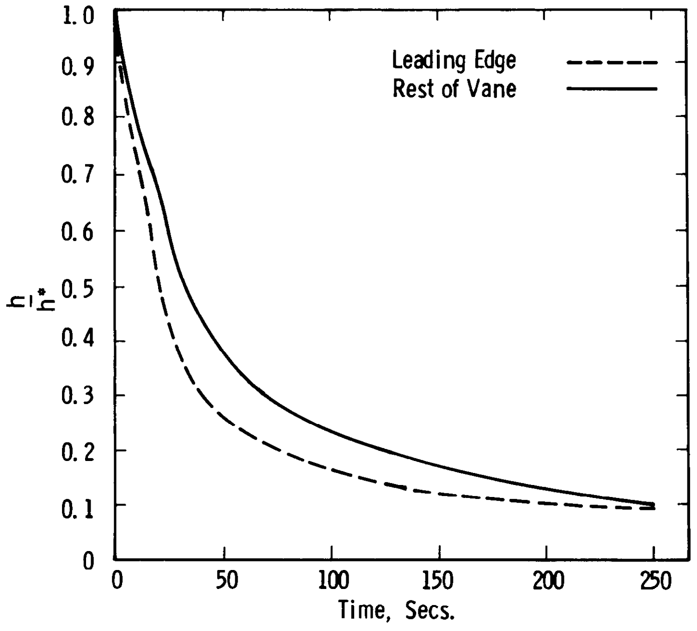

Figure 2-3. Heat Transfer Coefficient Ratios as a Function of Time for a Row 1 Vane Emergency Shutdown Condition

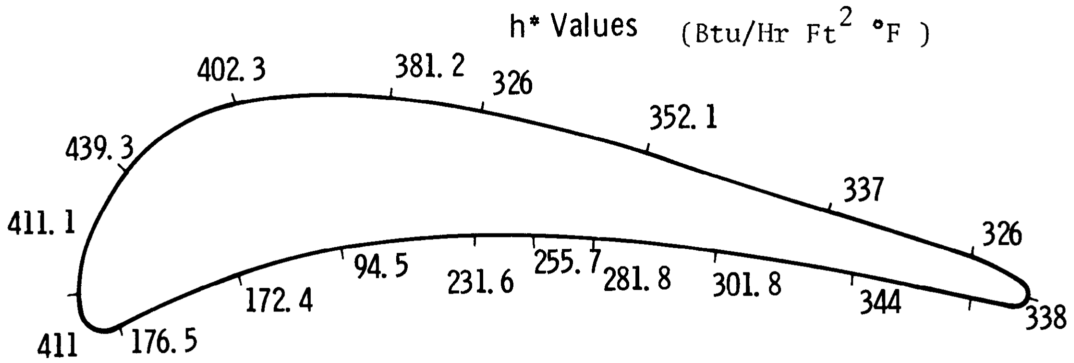

Figure 2-4. Distribution of Maximum Heat Transfer Coefficients around Row 1 Vane for an Emergency Startup and Shutdown Condition

A two-dimensional finite element plane strain program was used to calculate the stresses in the cross-sectional plane. The analytical model (Figure 2-5) treated the airfoil as if its length were infinite, thus eliminating end conditions from consideration.

The maximum out-of-plane tensile stresses were approximately twice the value of the maximum in-plane stresses for both Si_3N_4 and SiC materials as defined in Figure 2-6. Therefore, only the out-of-plane stresses were computed in subsequent calculations to determine the effect of vane size. For the full-size solid vane under shutdown conditions from 2500°F, the maximum tensile stresses were 47,000 psi and 44,000 psi for silicon carbide and silicon nitride, respectively, while full-size, hollow, silicon carbide vane calculations yielded tensile stresses as high as 51,000 psi based on generally accepted values for physical properties. This result was affected by shape factors which contributed to a stress concentration at the inside trailing edge radius even though local thermal gradients were reduced in the thin-wall geometry.

Since thermal gradients are sensitive to mass under transient conditions, airfoil cross section was given primary consideration in the low stress design optimization. For the W251 turbine, vane size (chord length) remained infinitely variable within the practical limits of a

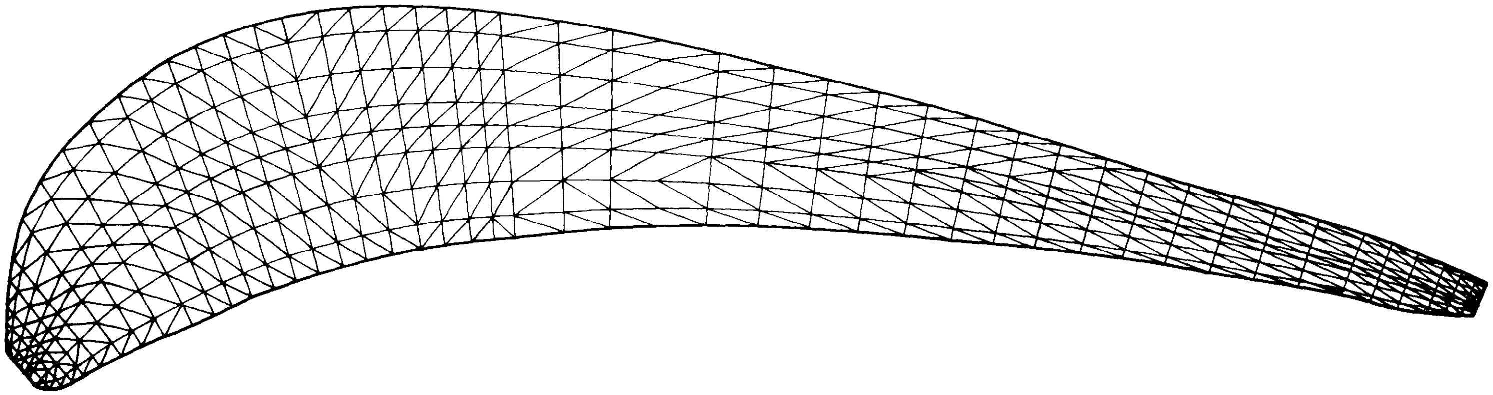

Figure 2-5. Two-Dimensional Finite Element Mesh for Solid Airfoil Section

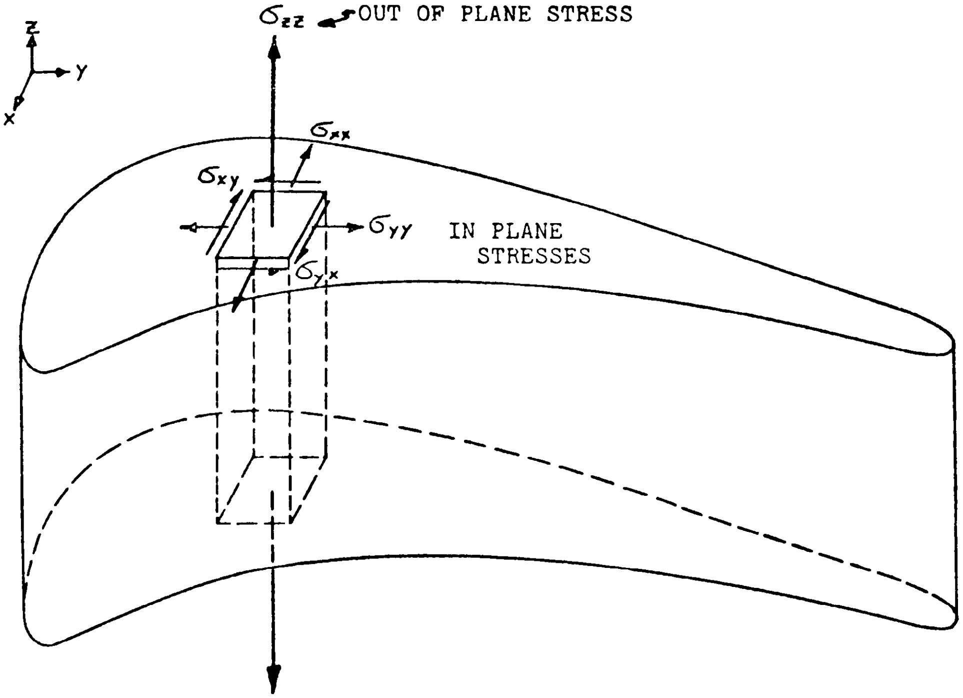

Figure 2-6. Thermal Stress in a Vane

fixed chord to pitch ratio where pitch is defined as vane spacing. Vane height was held constant because it determined turbine inlet area, a performance parameter, for an established diameter. The effect of the chord or vane cross-sectional area on the transient tensile stress history of full- or half-size vanes is illustrated in Figure 2-7 for peak gas temperatures of 1950 to 2500°F.

Gas pressure caused steady-state bending stresses of the order of 1000 psi for the simply supported vane as compared to 3000 psi for the cantilevered full-size vane. Reference to Figure 2-8 indicates that a reduction in the size of the component produced proportionally higher gas bending stresses in the vanes. Furthermore, more vanes were required to complete the stator row under the fixed chord-pitch constraint. The half-size vane offered the best stress compromise considering the number of vanes required. An increase from 40 to 80 vanes appeared to be practical.

Two-dimensional finite element and finite difference programs were used to determine the temperature and stress distribution in the half-size airfoil, using reliable engineering property data for Norton HS130 silicon nitride (Table 2-1).(2) Results from these analyses indicated that the maximum thermal stress at the leading edge of a half-size silicon nitride airfoil approached 41,000 psi, 12 seconds after shutdown from 2500°F.

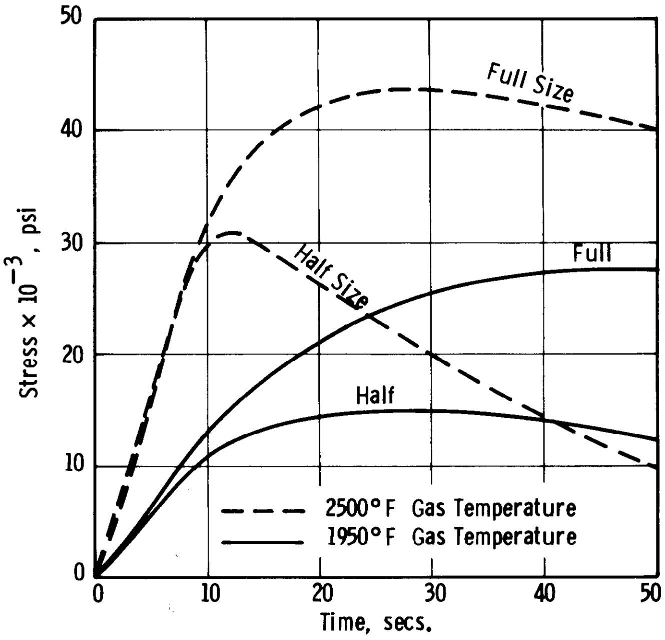

Figure 2-7. Stress History for Si_3N_4 Airfoils from 1950°F and 2500°F

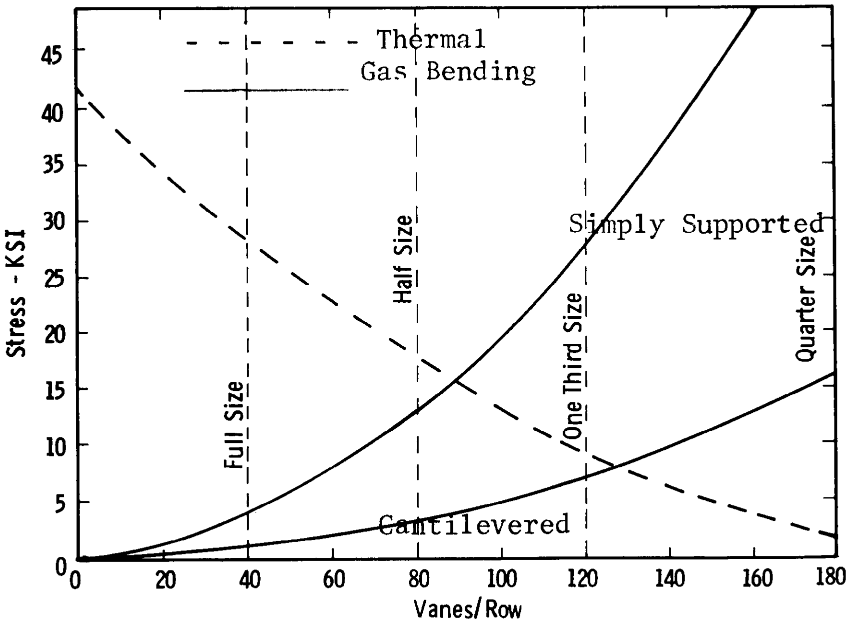

Figure 2-8. Maximum Stresses in Solid Airfoil as a Function of Size

TABLE 2-1

COMPARISON OF Si_3N_4 PROPERTY DATA

Temperature (°F)	Thermal Conductivity (Btu/hr-°F-ft)		Modulus of Elasticity x 10^{+6} psi		Coef of Expansion x 10^{-6} (in/in-F°)		Specific Heat (Btu/lb-F°)	
	Orig.*	BMI**	Orig.	BMI	Orig.	BMI	Orig.	BMI
80	13.5	18.7	41.2	44.	1.7	0.60	0.16	0.16
200	14.0	18.0	41.0	44.7	1.75	0.78	0.18	0.18
400	12.0	16.7	40.8	44.3	1.78	1.07	0.21	0.21
600	11.0	15.7	40.5	44.0	1.80	1.25	0.24	0.24
800	10.5	14.7	40.3	43.8	1.85	1.36	0.25	0.25
1000	10.0	13.7	40.1	43.3	1.87	1.46	0.26	0.26
1200	9.3	12.7	40.0	42.7	1.90	1.55	0.27	0.27
1400	8.8	12.0	39.8	42.0	1.95	1.67	0.28	0.28
1600	8.5	11.0	39.5	41.3	1.97	1.85	0.29	0.29
1800	8.2	10.5	39.3	40.0	2.00	1.93	0.30	0.30
2200	7.7	9.0	39.0	37.5	2.05	2.37	0.31	0.31
2500	7.5	8.3	38.7	29.0	2.15	2.40	0.32	0.32

---

*Accepted values for hot pressed silicon nitride in 1971.
**Initial results of thermal property measurements at Battelle Memorial Institute.(1,2)

This represented a 25 percent increase in calculated stress which was attributed to the material property data base. Temperature and stress distributions are reported in Figures 2-9 and 2-10, respectively. Comparable data were obtained from both the finite element and finite difference programs.(2)

Finally, simple changes in airfoil geometry were analyzed to lower the stress peaks in the leading and trailing edges still further.(2) The effect of blunting the leading and trailing edges of the half-size vane was studied for both silicon carbide and silicon nitride (Figure 2-11).

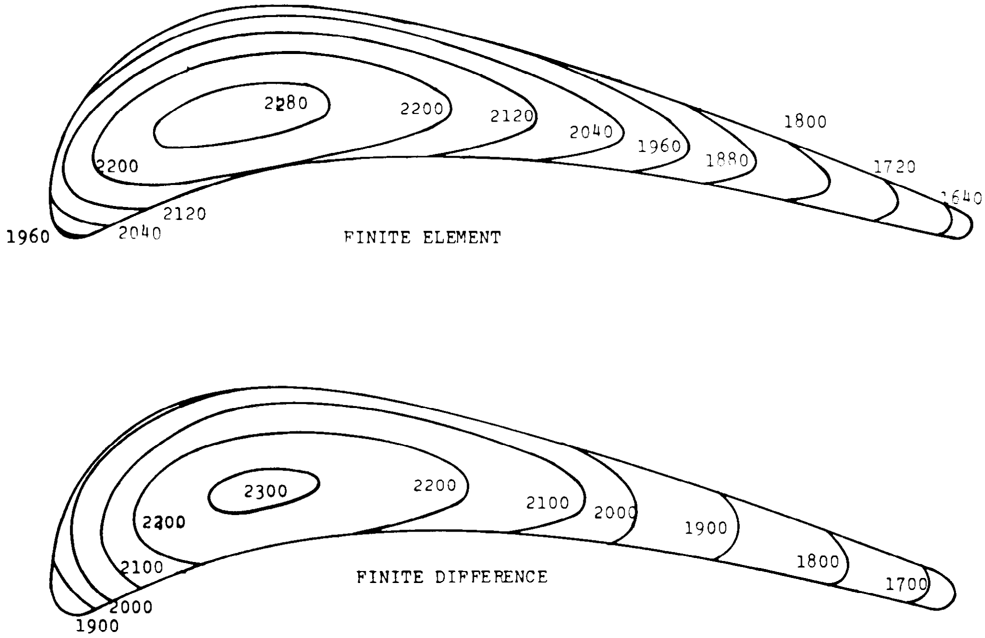

Figure 2-9. Temperature Contours in Solid Half-Size Si$_3$N$_4$ Airfoils (°F)

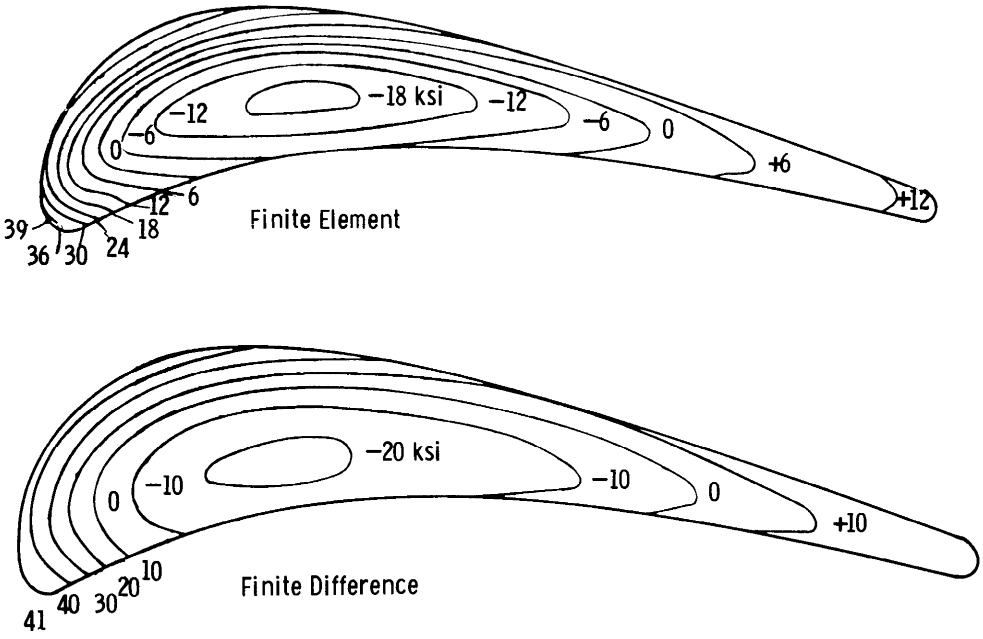

Figure 2-10. Stress Contours in Solid Half-Size Si$_3$N$_4$ Airfoils (Ksi)

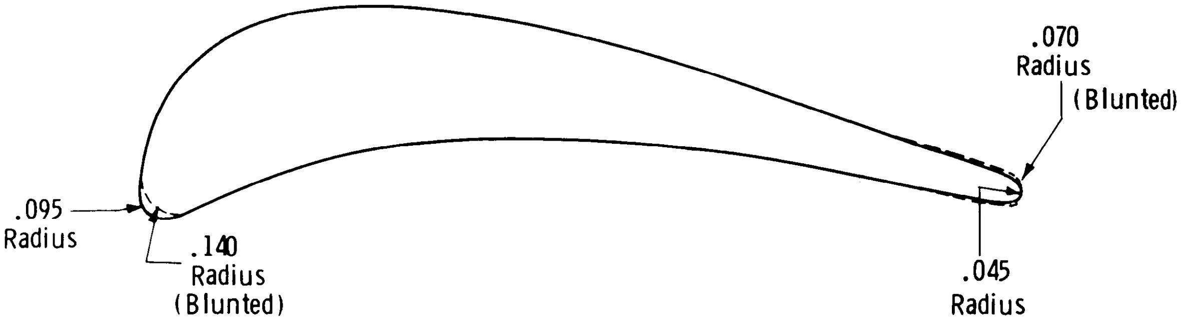

Figure 2-11. Dimensions of Blunted Leading and Trailing Edges of Ceramic Airfoils

An increase of 47 percent in leading edge radius produced negligible results. If the trailing edge radius and thickness were increased by 56 percent, the transient thermal stress would decrease 12 and 21 percent in SiC and Si_3N_4 vanes, respectively. No change in the airfoil profile was made, however, because the maximum stress occurred in the leading edge where the effect of blunting was negligible. Furthermore, any increase in the trailing edge thickness beyond that employed would affect gas flow adversely because of increased turbulence. Since the maximum out-of-plane principal tensile stress in the trailing edge almost equaled that expected to develop in the leading edge, critical stress rather than maximum stress would determine the location of failure initiation if it did occur. Failures, possibly of this type, were observed only on three occasions. The first occured in the trailing edge of preoxidized airfoil 3 during the initial 25 cycles of static rig testing at 2500°F.(8) Trailing edge failure origins were also identified in preoxidized airfoil 6 (cycles 26 - 60)(8) and airfoil 8 at the conclusion of the 2500°F static rig demonstration. No corrective action was taken and none appeared to be warranted.

2.3 CORRELATION OF DESIGN ANALYSIS CODES

The programs used to analyze stress development in vanes were correlated and compared with turbine passage experiments to establish their validity.(2,3) A transient axisymmetric finite element computer program was developed and used to calculate stresses in cylinders subjected to uniform gas cooling from above 1600°F down to 600°F. This axisymmetric program developed the complete state of stress, both in plane 1 and plane 2, as defined in Figure 2-12. The results, from this axisymmetric program correlated well with the computational method, which used a finite difference heat transfer program and numerical integration of stresses, when applied to a uniformly quenched cyclinder. The correlation increased the confidence of applying the existing programs to thermal shock tests in the turbine gas passage and to vane analyses.

Tests on silicon carbide were performed in the turbine passage. When the fuel was shut off, the gas temperature dropped from 2000°F (for example) to 600°F in a few seconds. Large thermal gradients were measured by thermocouples in a second SiC cylinder located beside the test cylinder. The stresses induced by differential thermal expansion caused cracking in the axial direction. Both computer methods predicted that axial stresses should be larger than circumferential stresses, and that circumferential cracks should appear.

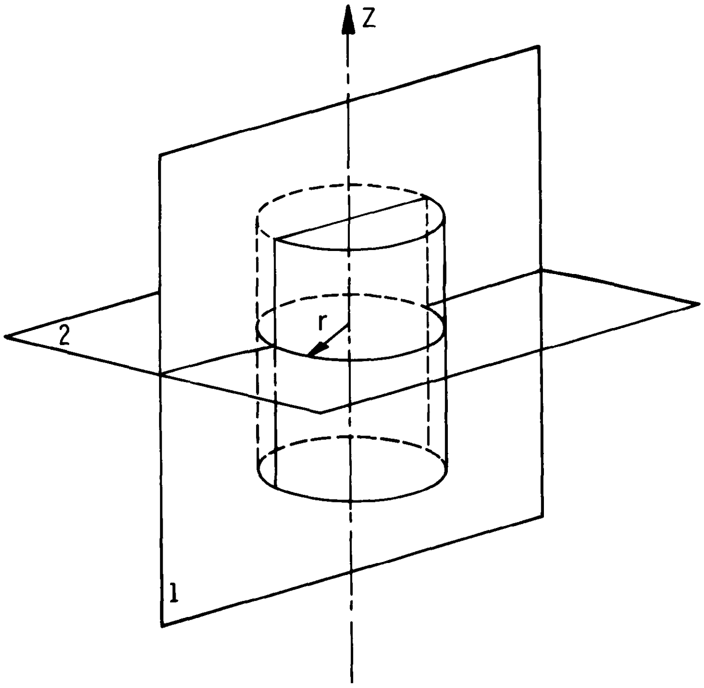

Figure 2-12. Thermal Quench Cylinder Coordinate System

Experiments indicated that quenching was uniform around the cylinder to within 10 to 15°F (Figure 2-13) and that the axisymmetric finite element program was applicable in plane 1 (Figure 2-12). Since the pertinent physical properties (coefficient of thermal expansion, thermal conductivity, elastic modulus and Poisson's ratio) of the SiC were not precisely known, and since the heat flux and loads imposed by the fixture at the ends were not controlled well, the discrepancy between analysis and experiment was anticipated. Figure 2-14 shows some typical results for the thermal quench of medium-strength hot pressed SiC.

Silicon nitride cylinders with accurately measured thermal diffusivity and coefficient of expansion were introduced into the passage to improve the experiment. Thermocouples were placed in wells such that both axial and radial temperature gradients could be measured. By rotating the cylinder, the variation in temperature around the circumference could also be monitored. These improvements provided a better check of computer results, and additional experience on the fixturing and instrumentation for ceramics in a turbine environment.

One-inch diameter by 2-inch high cylinders were heated to a steady-state temperature of 2000°F in a 500 ft/sec combustion gas stream at 3 atmospheres pressure. The fuel supply to the gas passage was interrupted causing the impingement of relatively cool compressor discharge air directly on the cylinder. Figure 2-15 is typical of Si_3N_4 in the test passage thermal

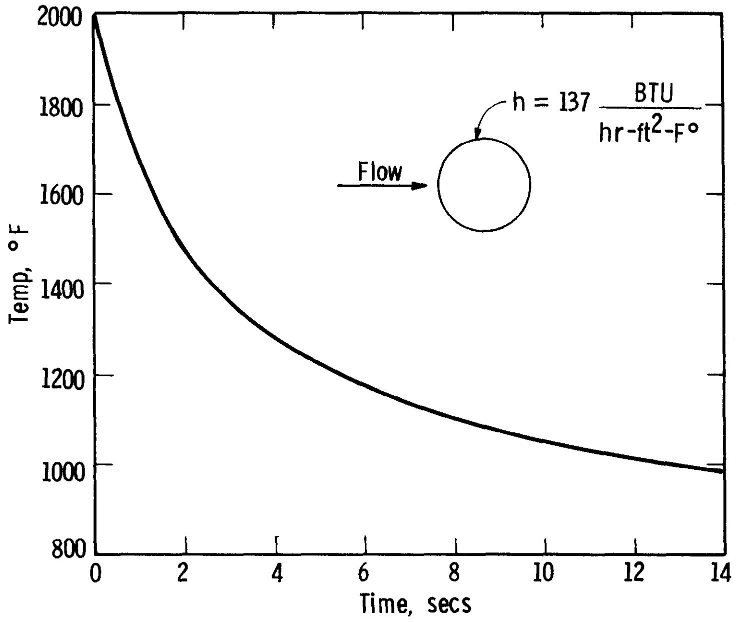

Figure 2-13. Boundary Conditions - Gas Temperature and Film Coefficient

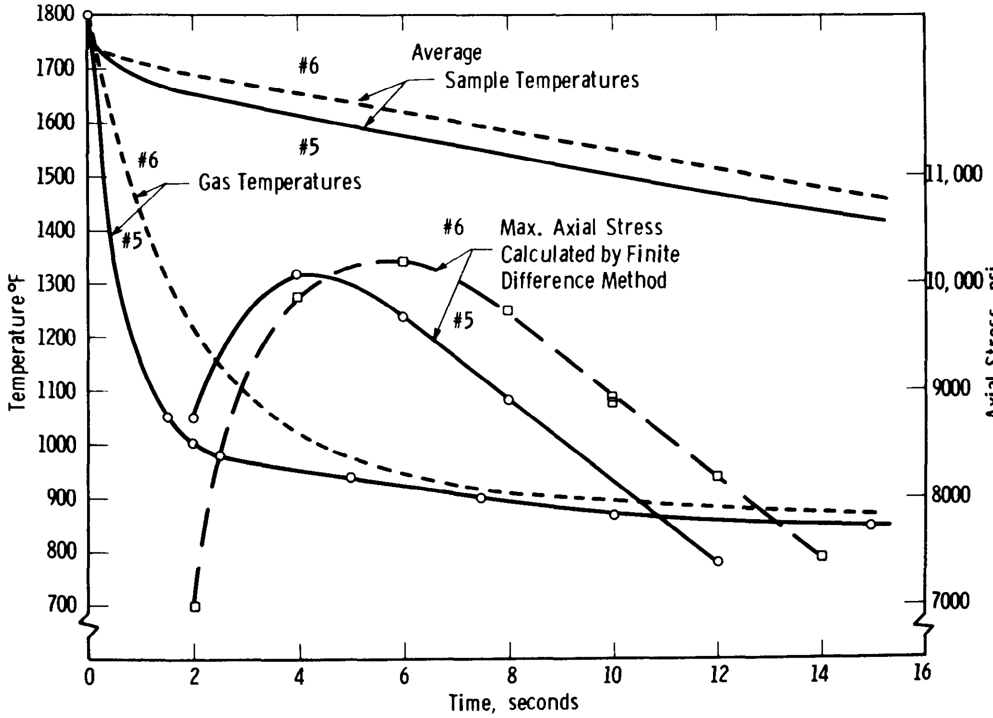

Figure 2-14. Temperature Decay and Maximum Transient Tensile Stress in the Axial Direction for Silicon Carbide Cylinders Cooled in Test Passage

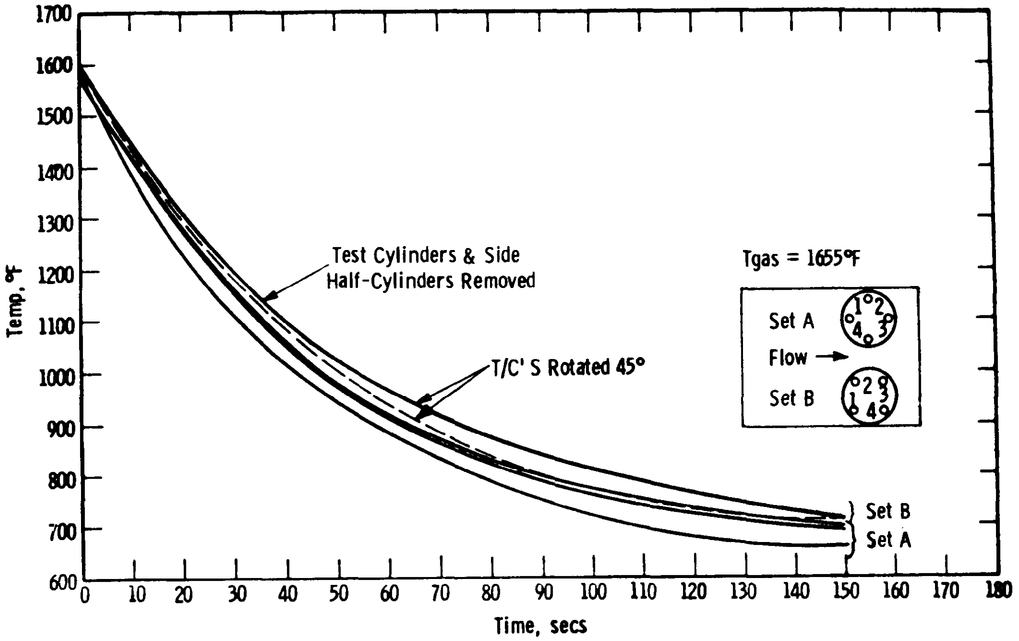

Figure 2-15. Temperature Decay for a Thermocouple at Position No. 3 in Thermally Quenched Cylinders of Si_3N_4

environment for the transient or shutdown mode. The film convection coefficient, h, for the shutdown was calculated from the gas properties, mass flow and physical dimensions of the test passage and cylinder.

Tests in the passage indicated quenching was uniform around the cylinder, i.e., within a 10°F deviation along the circumference. Therefore, an axisymmetric analysis was employed to calculate the temperature and stresses in the cylinder. The finite element models used to treat nonuniform cooling along the axis of the cylinder and the finite difference model used to treat cooling around the circumference of the cylinder are shown at the bottom of Figure 2-16. The top view illustrates the mesh used in the generalized plane strain program. This model was used to verify the axisymmetric thermal stresses and to calculate nonaxisymmetric stresses where required. Thermocouples were placed at various radial and axial locations in the cylinder to monitor thermal response and determine the magnitude of the radial and axial temperature gradients. Typical cylinder response is plotted in Figure 2-17 where actual temperatures as recorded by thermocouples located just below the surface are compared with predicted results from both the finite element and finite difference codes. Both methods predicted temperature response quite well. The finite element method appeared to yield a slightly better correlation.

The maximum tensile stress history generated by the thermal shock is given in Figure 2-18. This tensile stress occurred on the surface of the cylinder as a result of differential thermal contraction caused by the relatively cool gas which washed over it during shutdown. The maximum tensile stress reached a value of 12.8 ksi, well below the rupture strength of the material. Fourteen tests were run on two cylinders, one of which was drilled for thermocouple holes. Neither visual nor X-ray inspection disclosed cracks in either of the Si_3N_4 cylinders. Since the cylinder tests were conducted at the limit of the thermal shock capacity of the test passage, the test specimen configuration was changed to that of a simple teardrop-shaped airfoil. Initial shock tests with the instrumented airfoil produced cracks emanating from the thermocouple hole locations. No stress analysis was performed on the new configuration because better data were forthcoming from static rig tests at 2200°F, using full scale components.

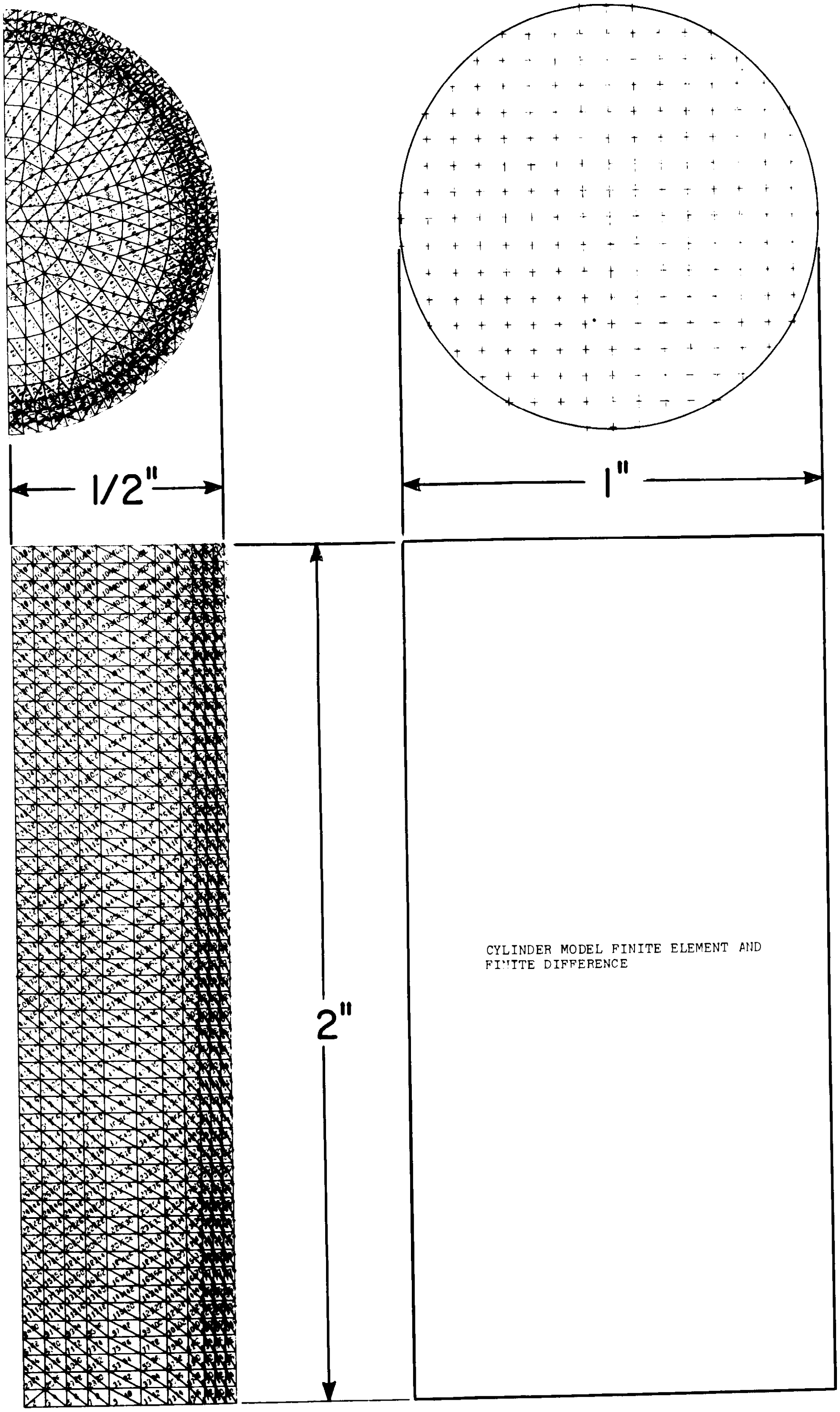
1/2"
1"
2"
CYLINDER MODEL FINITE ELEMENT AND FINITE DIFFERENCE

Figure 2-16. Cylinder Models

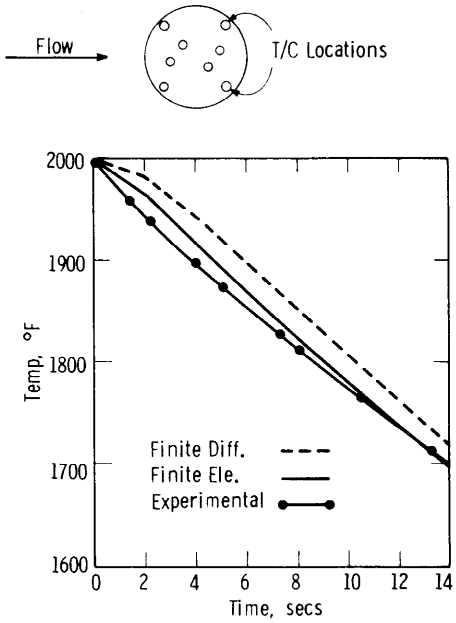

Figure 2-17. Effect of Time on Temperature for Cylinder Thermal Quench Test

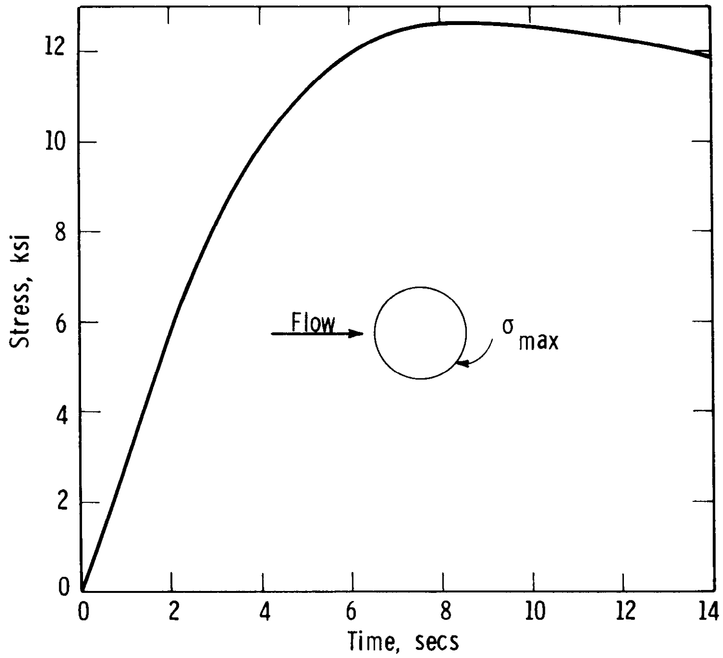

Figure 2-18. Development of Stress in Cylinder Thermal Quench Test

SECTION 3

STATOR VANE SYSTEM DESIGN CONCEPTS

3.1 INTRODUCTION

The ceramic stator vane design task involved the component itself and its incorporation into an existing turbine, the W251 (Figure 3-1). To accomplish this, close attention was paid to the characteristics of the ceramic vane materials and to the vane support structures which had to be developed as well. Three general systems concepts were evaluated initially.

Design concept I (Figure 3-2) utilized a ceramic end cap-to-spring pivot, where respective contact surfaces were spherical. The vane housing (inner and outer ring segments) was shielded from the hot ceramic end caps by an insulator, and the ceramic end caps served as a bridge between the combustor transition and the first rotating row of blades to shield the metal structure from the hot gas environment. As indicated in View C-C, the end caps were designed on an angle similar to the metal

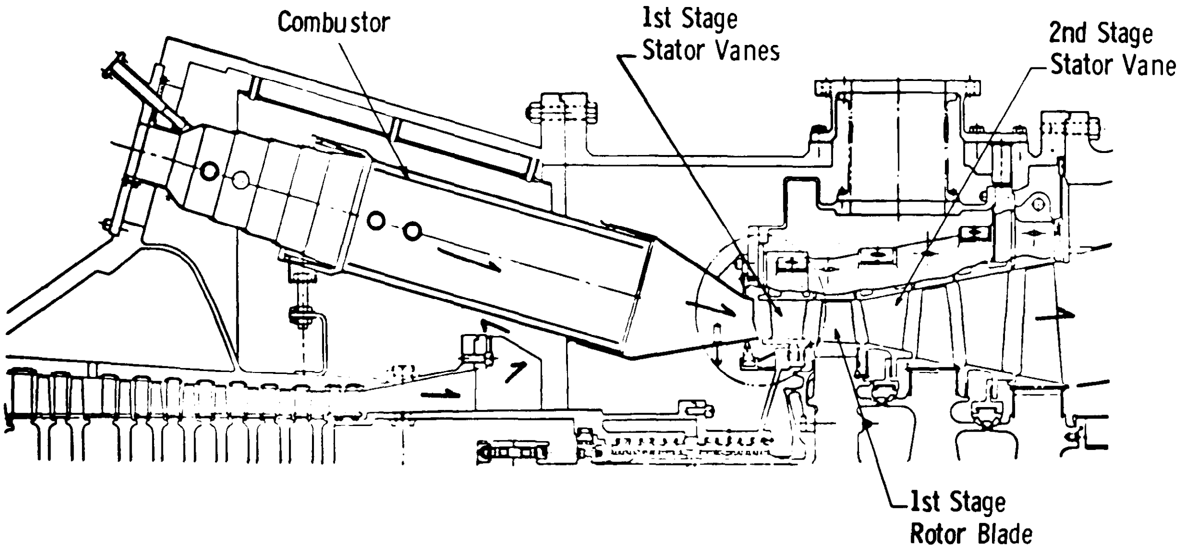

Figure 3-1. 30 Mw Test Turbine Flow Path

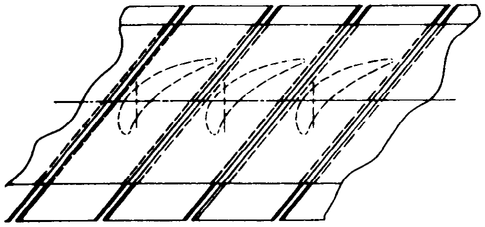

VIEW C-C

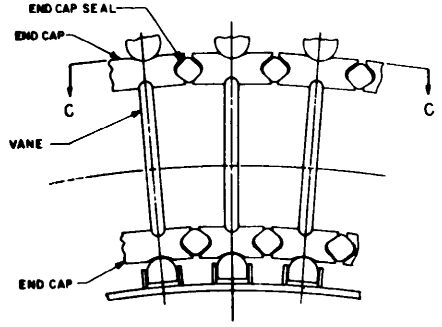
END CAP SEAL
END CAP
C
C
VANE
END CAP

SECTION B-B

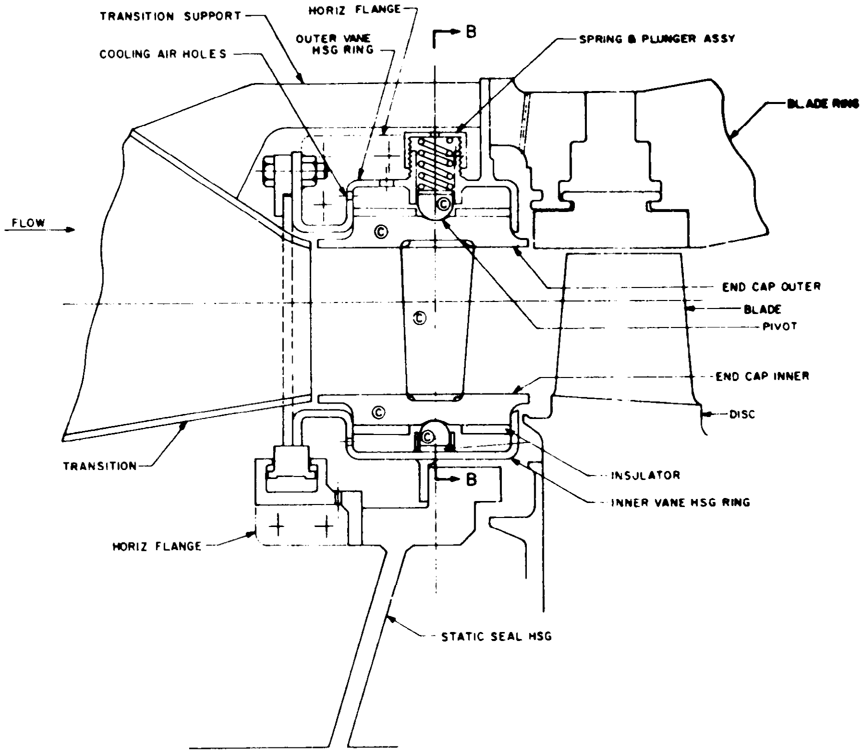
TRANSITION SUPPORT
HORIZ FLANGE
B
OUTER VANE HSG RING
SPRING & PLUNGER ASSY
COOLING AIR HOLES
BLADE RING
FLOW
END CAP OUTER
BLADE
PIVOT
END CAP INNER
DISC
TRANSITION
B
INSULATOR
INNER VANE HSG RING
HORIZ FLANGE
STATIC SEAL HSG

Figure 3-2. Design Concept #1

vane design currently employed. The end cap to end cap radial sealing arrangement is illustrated in Section B-B. The end cap seals were free-floating diamond-shaped ceramic pins which depend on positive pressure differential directed radially inward to force the seals against the end caps.

Design concept II (Figure 3-3) employed a ceramic end cap-to-spring pivot whose respective contact surfaces were also spherical. A metal extension piece was welded to the mouth of the combustor transition. This extension permitted the end cap section to be symmetrical, smaller and more compatible with the half-size vane. The sealing arrangement at the transition mouth was similar to that used in W251B1. Here, the end caps were rectangular (Section C-C) to allow the cylindrical slot to serve as a positive stop for the airfoil tenon (partial airfoil section shaped). The cross-hatched material indicated between the ceramic end caps and metal vane housing rings, and between the ceramic end caps and plungers was a porous weave metallic material used for uniform load distribution and cooling air access between the metal and ceramic.

Design concept III (Figure 3-4) combined a metal shoe pivoting arrangement with a spherical plunger-to-shoe pivot surface. The metal shoe transmitted the compressive spring load to an insulator and ceramic end cap, which in turn transmitted the force to the airfoil. The concept utilized two end-cap/airfoil segments per insulator/shoe, and thus each spring served to load two vane segments. Stability of the system was provided by two spherical pivots mounted in the inner ring housing as shown in Section B-B. Radial sealing between each segment was provided at the shoe location (Section B-B). Depending on established clearances, each end cap was free to slide circumferentially in its respective insulator track. Positive locking was provided at the shoe/insulator surface by a lip on the shoe (Section B-B) and at the insulator end cap surface by a slot that was alternately contained in the insulator and end cap of the adjacent shoe/insulator/end-cap combination.

A fourth and final design iteration (Figure 3-5, Longitudinal View, and Figure 3-6, Radial and Circumferential Views) evolved from careful analysis of the original three.(2,3) The basic element of the design was the three-piece ceramic stator vane assembly represented in Figure 3-7. A concave seat in the end cap was used with a convex vane tenon of compound curvature to provide contact surfaces that were ellipsoidal. The vane assemblies were paired for use with associated support hardware. Two vanes and two end caps were supported at either end by a single insulator and a single metal shoe. The outer metal shoe had a single pivot, plunger and spring, while the inner mechanism was made up of the metal shoe with two pivots and plunger. This arrangement gave three-point circumferential stability to the entire structure. The spring assembly, contained by the outer support ring, maintained the position of the vane assembly with the clamping force provided by the spring. A metal fiber mesh material cushioned and distributed the load between the insulator and the metal shoe. This material was also used as a seal between the insulator and ring housing.

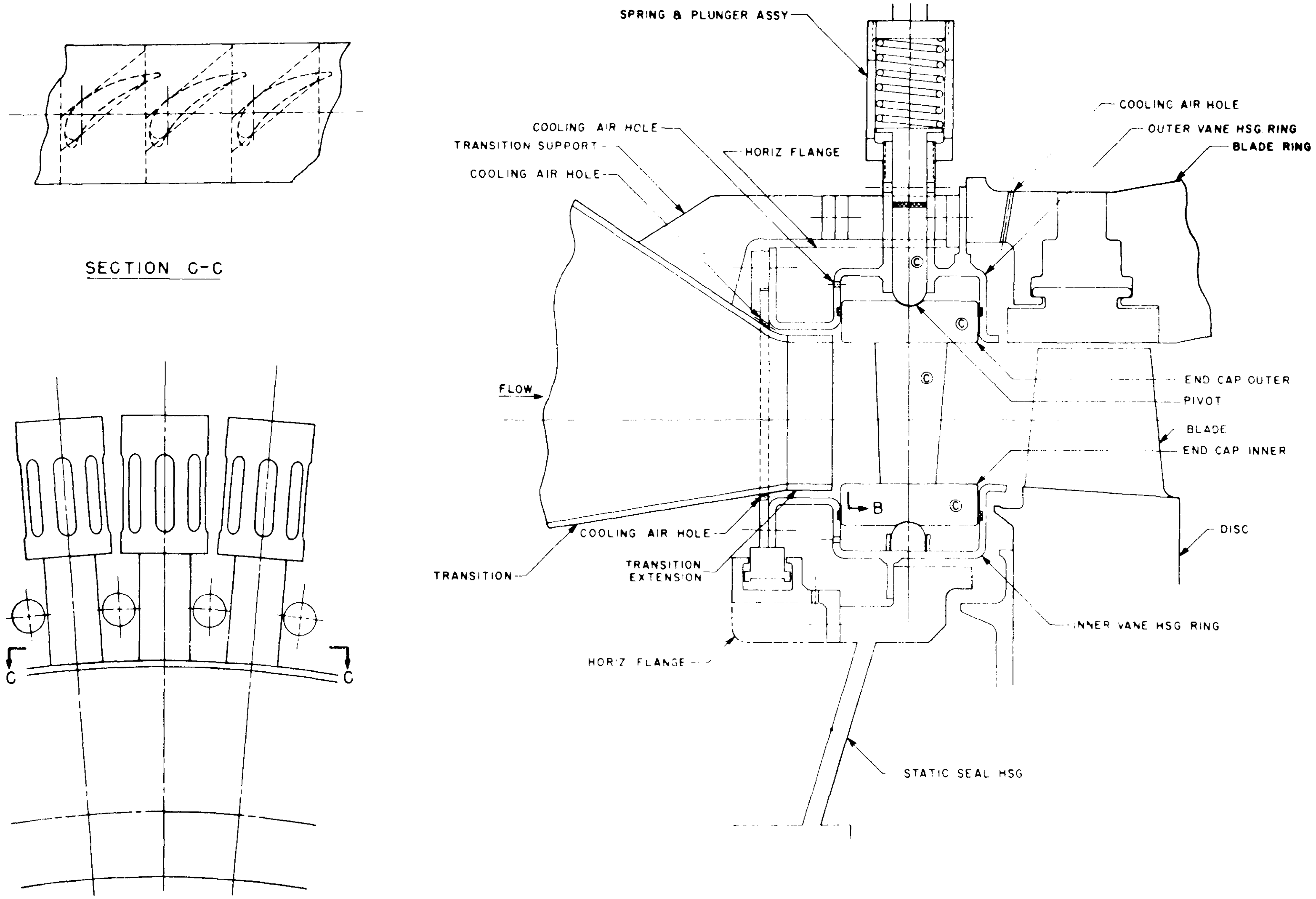
SECTION C-C
C
C
SPRING & PLUNGER ASSY
COOLING AIR HOLE
TRANSITION SUPPORT
COOLING AIR HOLE
HORIZ FLANGE
COOLING AIR HOLE
OUTER VANE HSG RING
BLADE RING
FLOW
END CAP OUTER
PIVOT
BLADE
END CAP INNER
B
DISC
COOLING AIR HOLE
TRANSITION
TRANSITION EXTENSION
INNER VANE HSG RING
HOR'Z FLANGE
STATIC SEAL HSG

Figure 3-3. Design Concept II

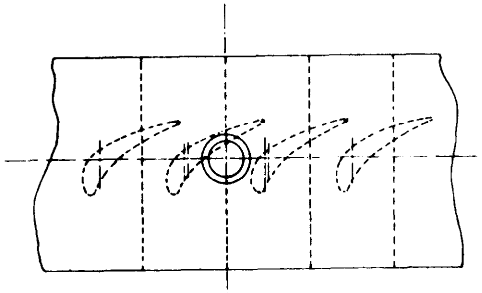

SECTION C - C

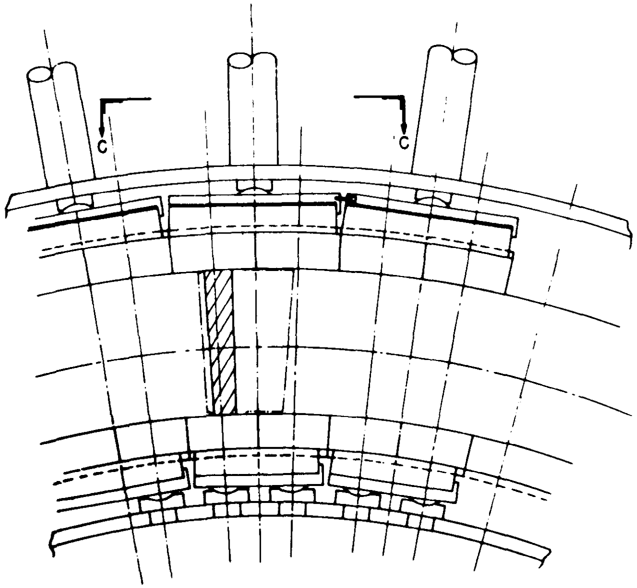

SECTION B - B

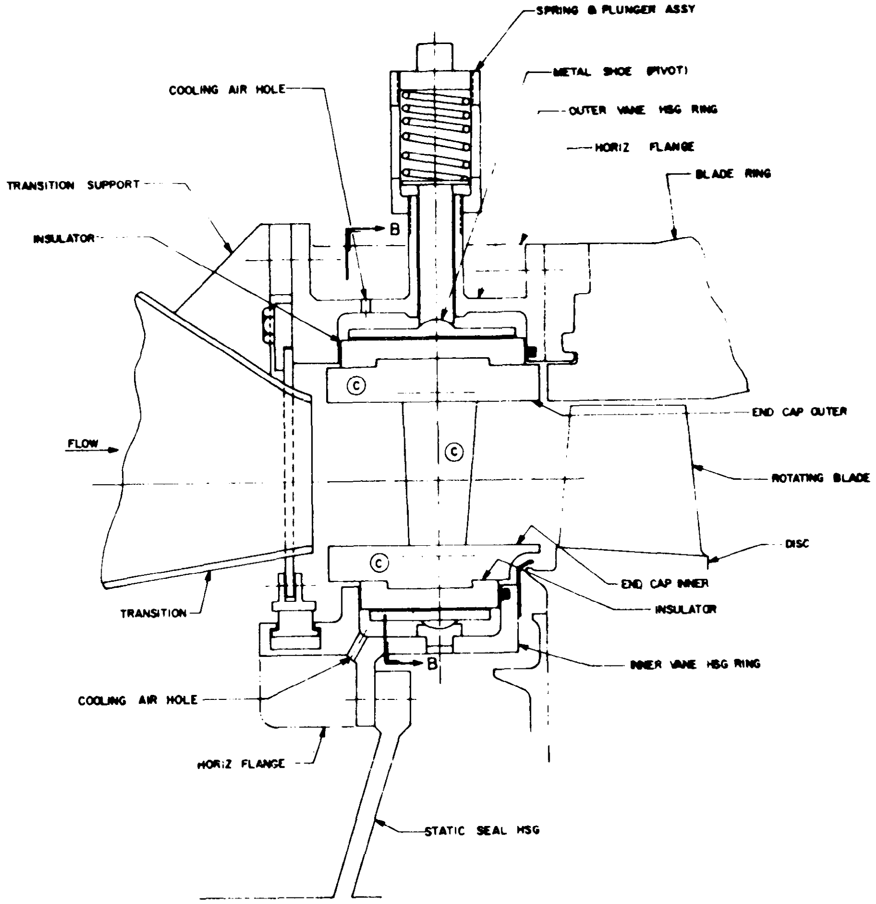

SPRING & PLUNGER ASSY
METAL SHOE (PIVOT)
OUTER VANE HSG RING
HORIZ FLANGE
BLADE RING
COOLING AIR HOLE
TRANSITION SUPPORT
INSULATOR
B
C
C
C
END CAP OUTER
FLOW
ROTATING BLADE
DISC
END CAP INNER
INSULATOR
TRANSITION
INNER VANE HSG RING
B
COOLING AIR HOLE
HORIZ FLANGE
STATIC SEAL HSG

Figure 3-4. Design Concept III

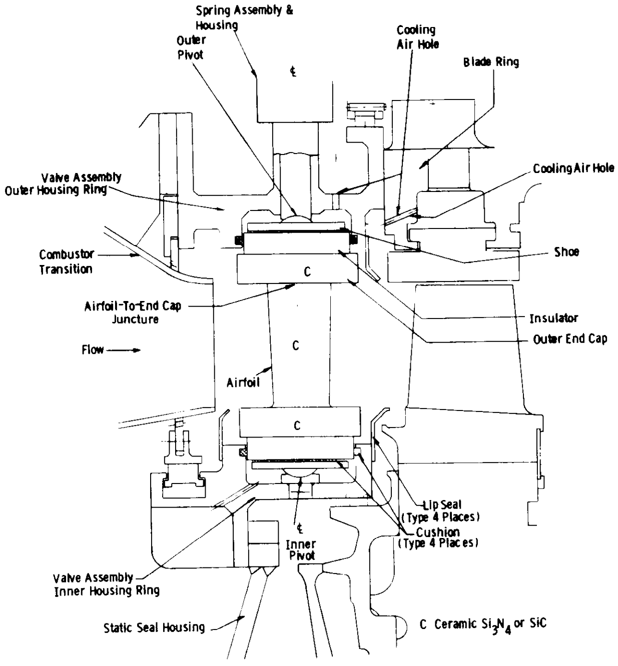
Spring Assembly & Housing
Outer Pivot
℄
Cooling Air Hole
Blade Ring
Valve Assembly Outer Housing Ring
Cooling Air Hole
Combustor Transition
Shoe
C
Airfoil-To-End Cap Juncture
Insulator
Outer End Cap
Flow
C
Airfoil
C
Lip Seal (Type 4 Places)
Cushion (Type 4 Places)
℄
Inner Pivot
Valve Assembly Inner Housing Ring
Static Seal Housing
C Ceramic Si3N4 or SiC

Figure 3-5. First Row Ceramic Stator Vane Assembly - Longitudinal View (First Generation Static Rig Test Configuration)

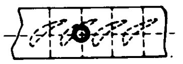

Radial View

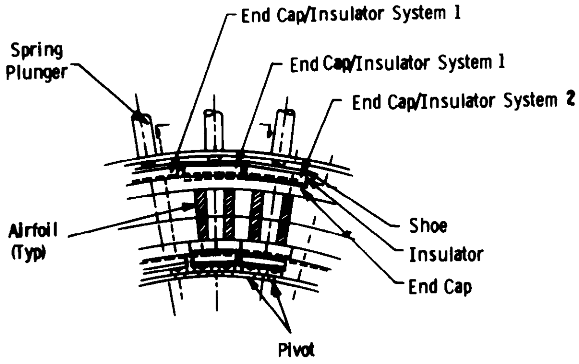
End Cap/Insulator System 1
Spring Plunger
End Cap/Insulator System 1
End Cap/Insulator System 2
Airfoil (Typ)
Shoe
Insulator
End Cap
Pivot

Circumferential View

Figure 3-6. First Row Ceramic Stator Vane Assembly - Radial and Circumferential Views (First Generation Static Rig Test Configuration)

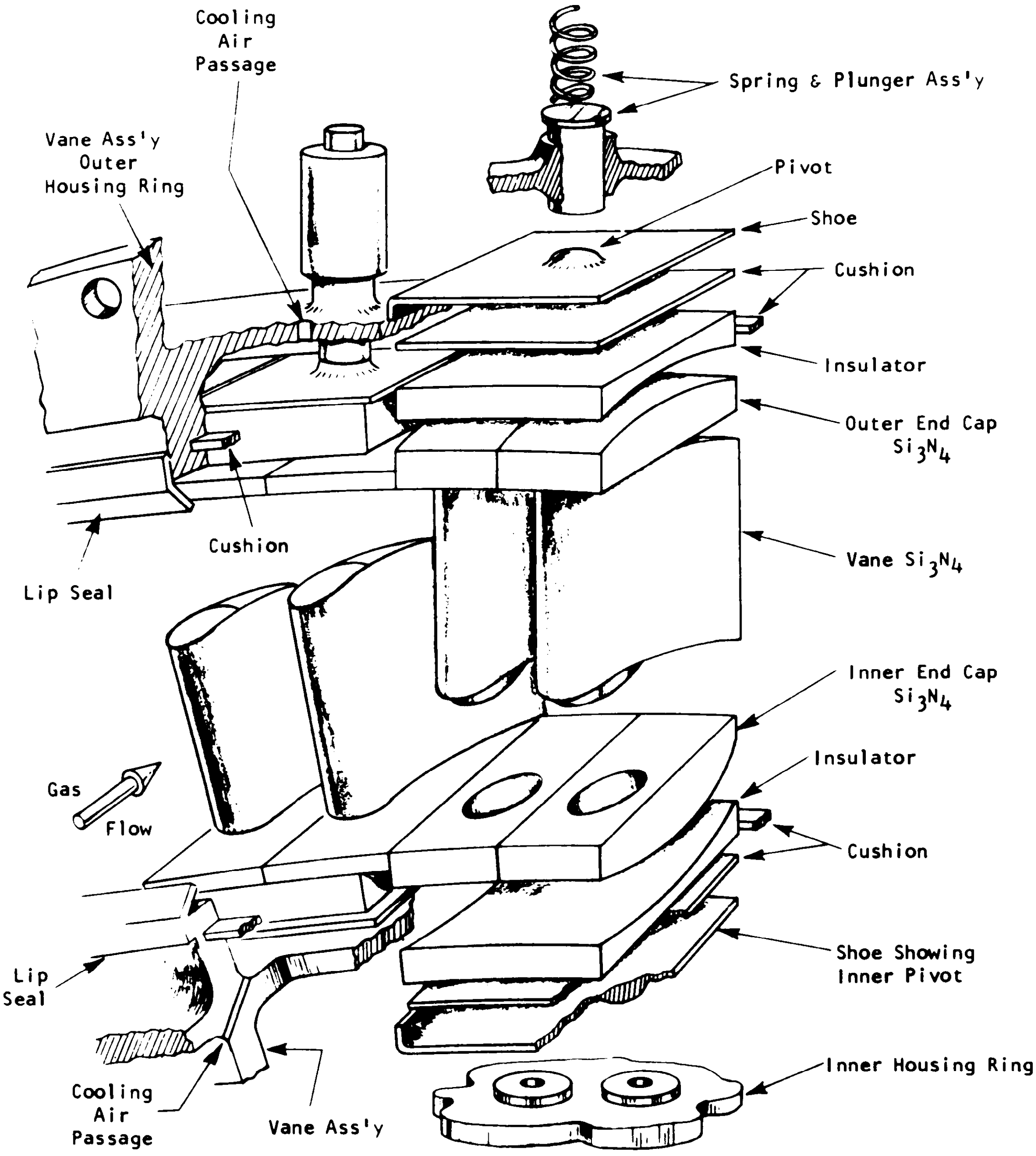
Cooling Air Passage
Spring & Plunger Ass'y
Vane Ass'y Outer Housing Ring
Pivot
Shoe
Cushion
Insulator
Outer End Cap Si_3N_4
Cushion
Lip Seal
Vane Si_3N_4
Inner End Cap Si_3N_4
Insulator
Gas Flow
Cushion
Shoe Showing Inner Pivot
Lip Seal
Inner Housing Ring
Cooling Air Passage
Vane Ass'y

Figure 3-7. Ceramic Vane and Support Hardware Assembly

Special attention was given to the fine details in the design. For instance, a lip on the metal shoe was provided to prevent insulator segments from slipping in the circumferential direction. Positive locking of the end cap pairs was accomplished by an end cap thickness change. End cap pairs were matched with insulator segments of appropriate dimension to keep the combined end cap insulator thickness constant.

Airfoil alignment and locking were controlled by airfoil and tenons which fitted into close tolerance cavities in the end caps. Within the limits of established clearance, each end cap was free to move circumferentially in its respective insulator tract. Therefore, both adjustment of the airfoils with respect to the end caps and vane assembly motion relative to the support structure were possible.

Axial gas loads were transmitted from the airfoil to the end caps and insulator and finally across the cushion material at the downstream end face of the insulator. Tangential gas loads were transferred from the pressure surface of the airfoil, through the end cap and insulator, to a lip on the inner and outer shoes and finally at the shoe pivots.

Small, rectangular-shaped end caps were used to minimize thermal stress generally. The use of sheet metal ring lip seals made this end cap size reduction possible. Contoured contact surfaces were specified to minimize contact stresses. Radial sealing was accomplished by the free floating strip seals which separated the metal shoes.

Compressor discharge air at 650°F was used to cool the combustor transition, static seal housing, combustor transition support, turbine cylinder, blade ring, and vane housing ring segments.

3.2 FIRST GENERATION STATOR VANE ASSEMBLY DESIGN

The foregoing discussion pertains to the first stage stator vane system designed for static rig and turbine testing. The actual ceramic vane structure is described in general terms only. Emphasis was placed on the mechanical aspects of a ceramic component in the first generation design iteration(2,3) illustrated in Figure 3-8. A nontwisted parallel-sided airfoil was specified to simplify manufacture since the parts were designated for static rig testing only. The intent was to establish a brittle material's ability to survive in a high temperature gas turbine environment and to demonstrate design viability. Neither required a tapered-twisted airfoil.

The airfoil-to-end cap juncture is critical in this three-piece ceramic stator vane design. Steady-state contact stresses develop at the interface as a result of:

1. A 400 lb compressive spring load, directed radially with respect to the turbine axis
2. A 200 lb axial gas pressure load
3. A 100 lb tangential gas pressure load
4. A 60 in-lb gas pressure twisting moment

A simply supported design criterion was established to provide airfoil-to-end cap adjustment to gas loads (bending and twist). Care was taken to minimize stress concentration as well as steady-state and transient thermal stresses. The circumferential interlocking feature of the end cap pairs with alternating insulators of different thickness is shown in Figure 3-9.

The end cap design is defined precisely in Figure 3-10. A compound curvature locking concept (Figure 3-11) is used to prevent the airfoil end support from ratcheting out of the end cap groove. Contact stresses are minimized by a torroidal shaped pivot-to-seat configuration. The pivot portions of the airfoil are described in terms of major and minor radii in Figure 3-12. The torroidal groove, ground to conform to the airfoil tenon geometry, is presented as an ellipse at the surface of the end cap (Figure 3-10, radial view). Therefore, the contact stresses resulting from the normal and tractive loads on the airfoil and end cap develop along an ellipsoidal surface.

Component dimensions and tolerances are critical. For example, if the major radius of the pivot were made equal to one-half the total airfoil height (i.e., R_a = 2.55 inches, Figure 3-11), rotation about

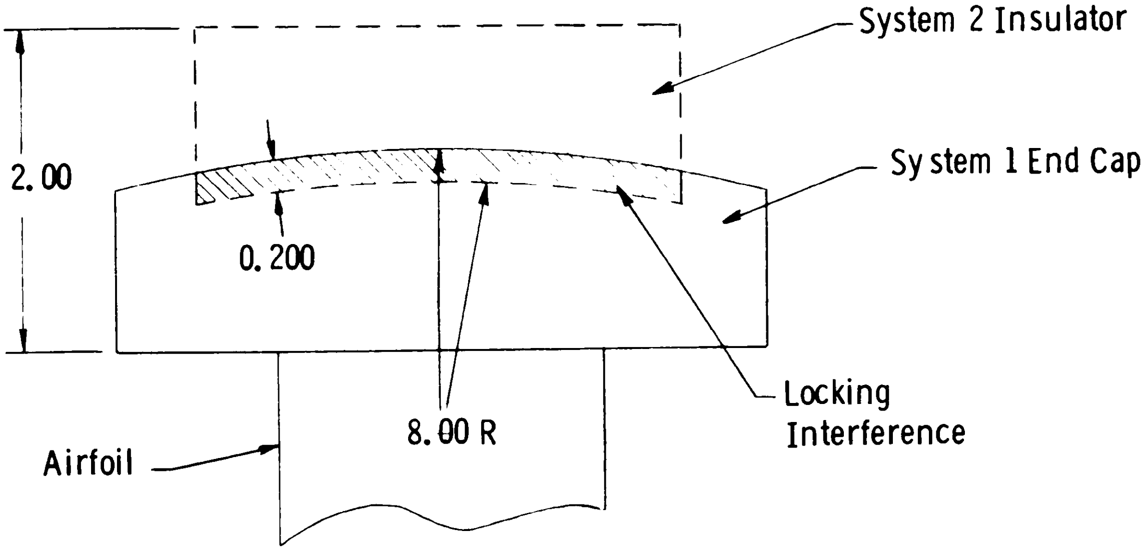
System 2 Insulator
System 1 End Cap
2.00
0.200
8.00 R
Locking Interference
Airfoil

Figure 3-8. First Generation, First Row Ceramic Vane Assemblies with Airfoil, End Caps and Insulators - Systems 1 and 2 Provide Circumferential Locking

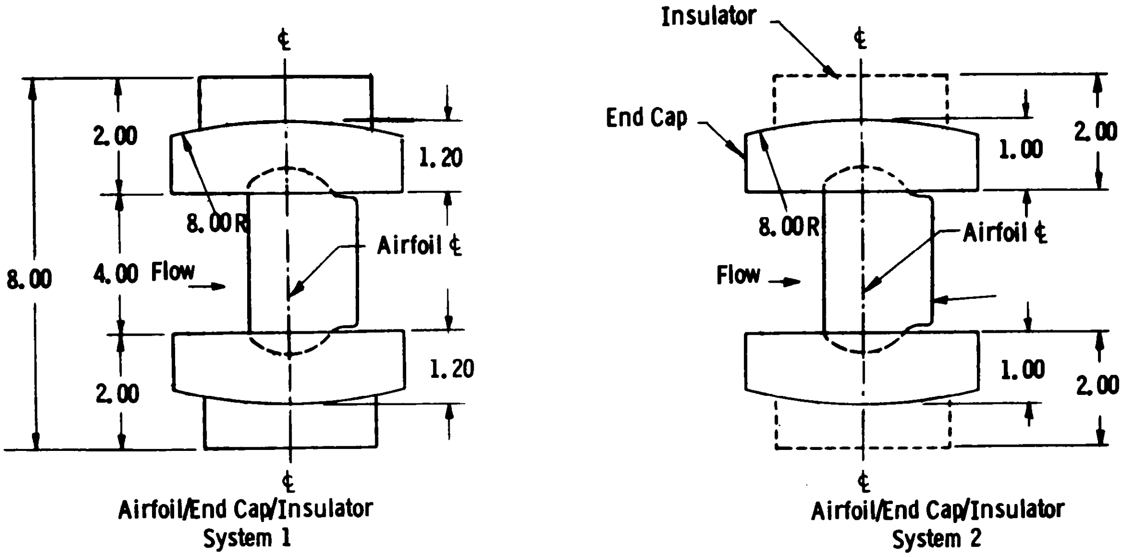
℄
2.00
1.20
8.00R
Airfoil ℄
8.00
4.00
Flow
2.00
1.20
℄
Airfoil/End Cap/Insulator
System 1
Insulator
℄
End Cap
1.00
2.00
8.00R
Airfoil ℄
Flow
1.00
2.00
℄
Airfoil/End Cap/Insulator
System 2

Figure 3-9. First Generation Ceramic Vane End Cap to Insulator Circumferential Locking Arrangement

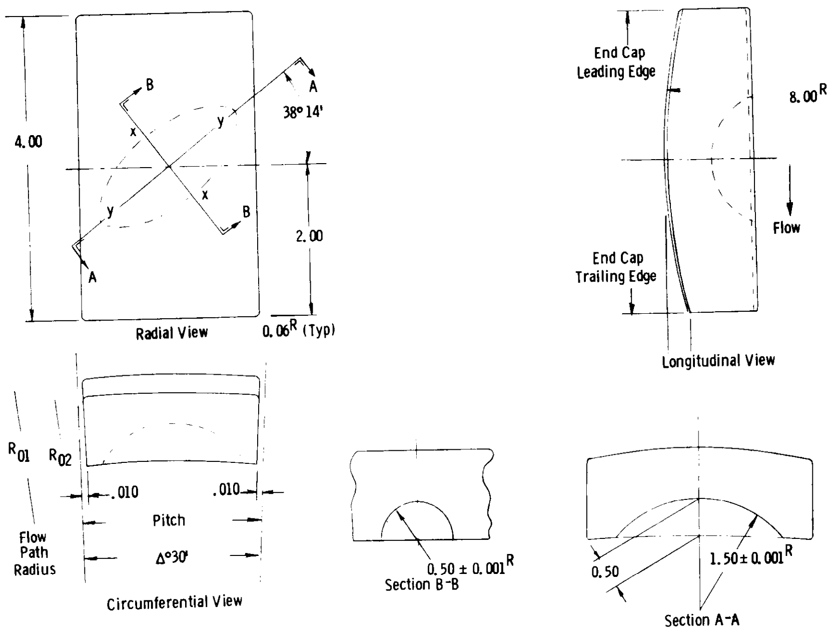
4.00
B
A
38° 14'
x
y
y
x
B
A
2.00
Radial View
0.06R (Typ)
End Cap Leading Edge
8.00R
Flow
End Cap Trailing Edge
Longitudinal View
R01
R02
.010
.010
Pitch
Flow Path Radius
Δ°30'
Circumferential View
0.50 ± 0.001R
Section B-B
0.50
1.50 ± 0.001R
Section A-A

Figure 3-10. First Generation Ceramic End Cap Configuration

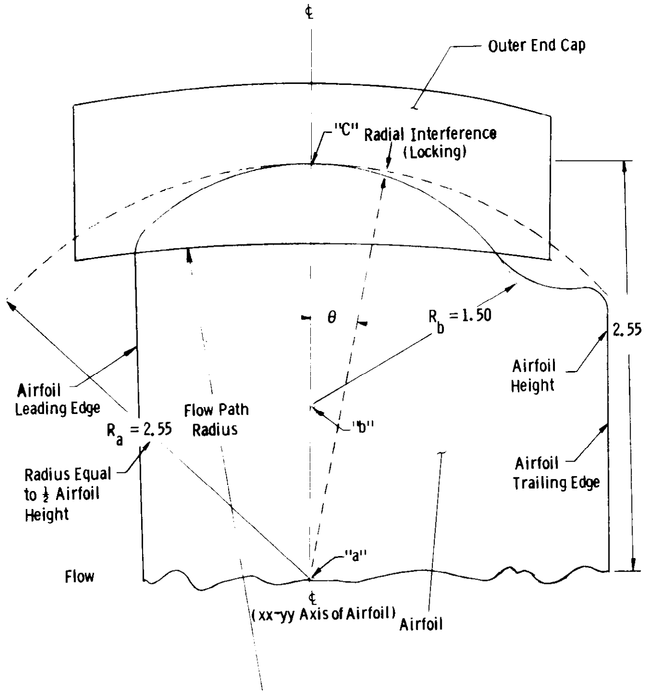
℄
Outer End Cap
"C" Radial Interference (Locking)
θ
Rb = 1.50
2.55
Airfoil Height
Airfoil Leading Edge
Flow Path Radius
Ra = 2.55
"b"
Radius Equal to ½ Airfoil Height
Airfoil Trailing Edge
"a"
Flow
℄ (xx-yy Axis of Airfoil)
Airfoil

Figure 3-11. First Generation Airfoil-to-End Cap Juncture - Compound Curvature Locking Concept

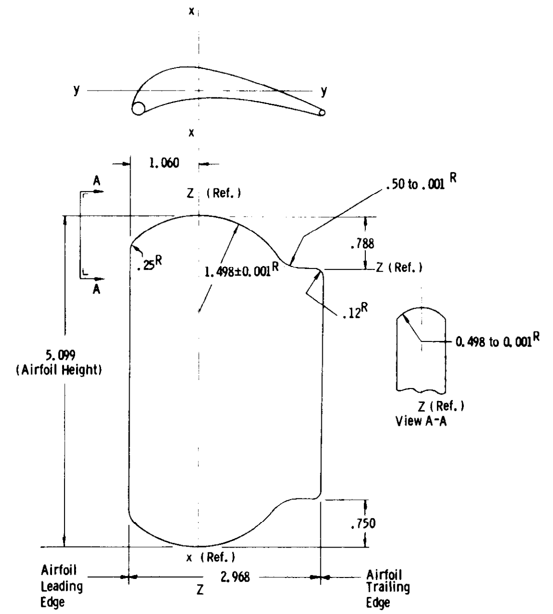
x
y
y
x
1.060
A
A
Z (Ref.)
.50 to .001 R
.788
Z (Ref.)
.25R
1.498±0.001R
.12R
0.498 to 0.001R
5.099
(Airfoil Height)
Z (Ref.)
View A-A
.750
x (Ref.)
Airfoil
Leading
Edge
2.968
Z
Airfoil
Trailing
Edge

Figure 3-12. First Generation Ceramic Airfoil End Configuration

point "a" is possible and the airfoil may ratchet into misalignment or out of the blade path. These possibilities are precluded by making the major radius R_b = 1.50 inches, with the center at point "b." The amount of locking under these conditions is determined by the radial interference at angular position Θ. As the airfoil tends to rotate about point "a" and slide at point"c" (assuming the end cap is fixed to resist rotation), the radial interference which develops offers increasing resistance to rotation.

3.3 FIRST GENERATION STATOR VANE ANALYSIS

Considerable effort was expended in the analysis of stresses at the critical interfaces which are inherent in the first generation stator vane assembly design.(3,4) The vane assembly and support structure are subjected to two principal loads acting against each other. The compressive spring load must be great enough to neutralize the three components of the gas load if the airfoils are to remain stable in a high velocity gas stream. Since the stator vane function is to turn the gas stream and since the individual elements of the vane assembly are joined at curved interfaces, the three components of the gas load are defined as:

1. The pressure force against the vane action 28° from the axial direction
2. The radial compressive force directed ultimately against the spring-loaded shoe
3. The twisting moment about the radial axis of the vane

The stress calculations were performed using conventional two-dimensional finite element and finite difference computer codes which were expanded to handle specific geometries and conditions.

Si_3N_4 and SiC exhibit very little or no plastic response prior to fracture at temperatures below 2300°F. Therefore, the maximum tensile stress at all points of contact must be defined explicitly so that a reasonable safety factor can be applied to avoid the generation and catastrophic propagation of localized cracks.

The four load types are defined with respect to the sandwiched vane in Figure 3-13. The radially compressive spring load is a design parameter that remains essentially constant over the cycle of operation. The components of the gas load rise to peak values during operation after short transients. Each of the interfaces associated with the design represents an interdependent system with respect to both radial and friction-reacted tangential loads. This condition complicated the optimum choice of geometry, surface finish and applied spring load.

Curved surfaces are in area contact at the airfoil-end cap interface. The contact stress field was analyzed by superimposing the two stress fields derived from normal and tangential loads. Standard elasticity theory was used to calculate normal loads. Stresses due to tangential loads were determined by the extension of a cylindrical analogy method for simple cylindrical contacts to the actual situation. The normal load pressure surface was sectioned in the plane of the tangential load so that incremental parts of the semiellipse could be modeled by an

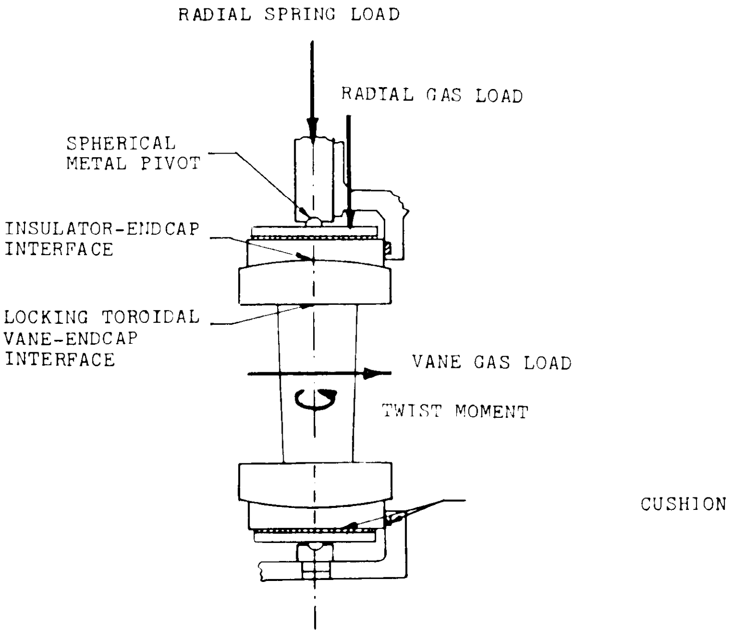
RADIAL SPRING LOAD
RADIAL GAS LOAD
SPHERICAL METAL PIVOT
INSULATOR-ENDCAP INTERFACE
LOCKING TOROIDAL VANE-ENDCAP INTERFACE
VANE GAS LOAD
TWIST MOMENT
CUSHION

Figure 3-13. Loads and Interfaces

appropriate hemicylinder as described in Figure 3-14. For this particular situation, L was chosen such that B = b and $Q_o = q_o$. Thus, the stresses along the minor axis LM, due to tangential load only, were identical to those along line NP. Generalized computer codes indicating location and maximum stress components due to combined loading were prepared for use in a parametric study to optimize the design. The analysis indicated:

Compressive stress, σ_{cmax}, = 11,700 psi

Tensile stress, σ_{Tmax}, = 6,100 psi without friction

Shear stress, σ_{Smax}, = 4,500 psi

at the airfoil-end cap interface. The state of stress due to contact is superimposed upon the maximum transient and steady-state thermal stresses acting on the airfoil tenon and end cap, however.

Another very important aspect of curved interfaces is their kinetic behavior as a function of load and friction.(4) When the gas load is applied at turbine startup, the center of the contact rotates through some angle Φ. Figure 3-15 shows a simple one-dimensional force

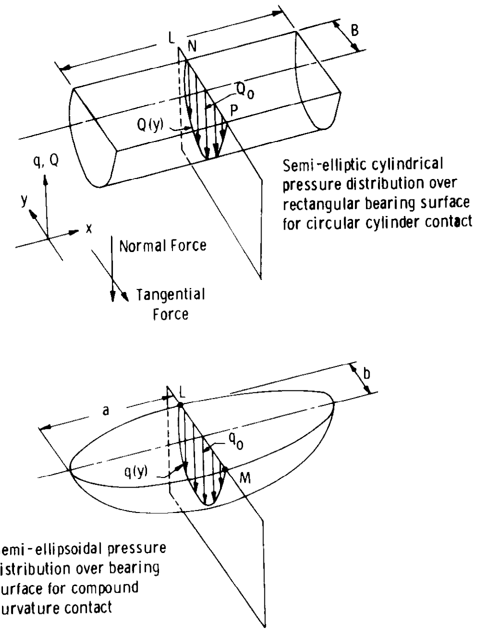
L
N
B
Q_0
P
Q(y)
q, Q
y
x
Normal Force
Tangential Force
Semi-elliptic cylindrical pressure distribution over rectangular bearing surface for circular cylinder contact
b
L
a
q_0
q(y)
M
Semi-ellipsoidal pressure distribution over bearing surface for compound curvature contact

Figure 3-14. Cylindrical Contact Analogy for the Determination of Stresses Due to Tangentially Applied Tractive Loads on a Body with Compound Curvature

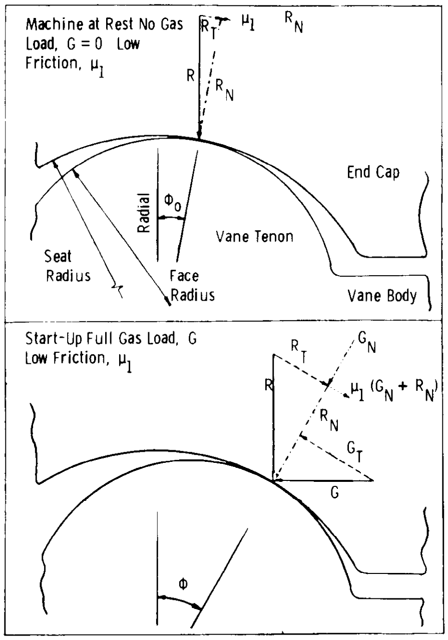
Machine at Rest No Gas Load, G = 0 Low Friction, μ_1
R_T
μ_1
R_N
R
R_N
End Cap
Radial
Φ_0
Vane Tenon
Seat Radius
Face Radius
Vane Body
Start-Up Full Gas Load, G Low Friction, μ_1
R_T
G_N
R
$\mu_1 (G_N + R_N)$
R_N
G_T
G
Φ

Figure 3-15. One-Dimensional Force Equilibrium Diagram for the Airfoil-End Cap Interface

equilibrium diagram for a situation which corresponds to a turbine at rest and just after start. R identifies the radial compressive loads while G represents the vane gas load where the subscripts T and N refer to the tangential and normal components, respectively, defined with respect to the interface. The net normal load on the interface is $G_N + R_N$, while the net tangential load is $\mu l \ (G_N + R_N)$. Maximum tensile stress is a function of the startup coefficient of friction for the vane end cap interface as shown in Figure 3-16.

Another subroutine was generated to define the elastic contact surface at the end cap groove-airfoil tenon interface more fully. The radial spring force is applied to prevent the tenon from moving out of the end cap groove. Any displacement of the contact center that is large enough to reduce the actual contact area, i.e., where the nominal contact surface is moved to extend beyond the pieces in contact or any drastic rearrangement of the pressure surface to compensate for such movement, results in a much higher stress field or region of contact singularity.

The results of this stress analysis(4) appear in Figures 3-17, 3-18 and 3-19, where the position of the contact area with respect to the airfoil perimeter and the maximum tensile stresses during startup and shutdown are indicated. Even at very low coefficients of friction

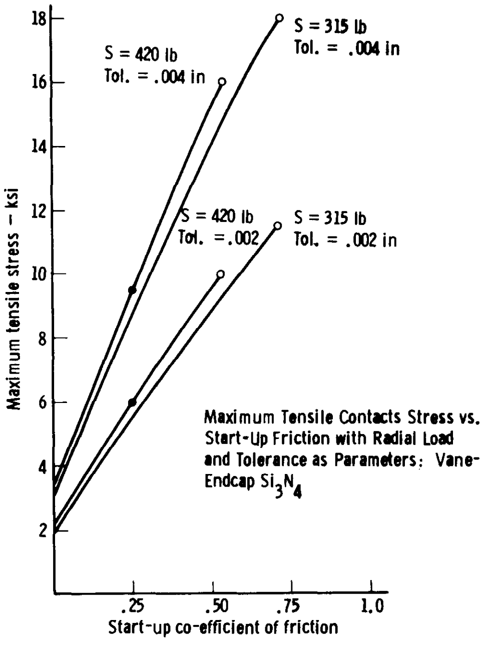

Figure 3-16. The Effect of Friction on Maximum Contact Stress at the Airfoil-End Cap Interface

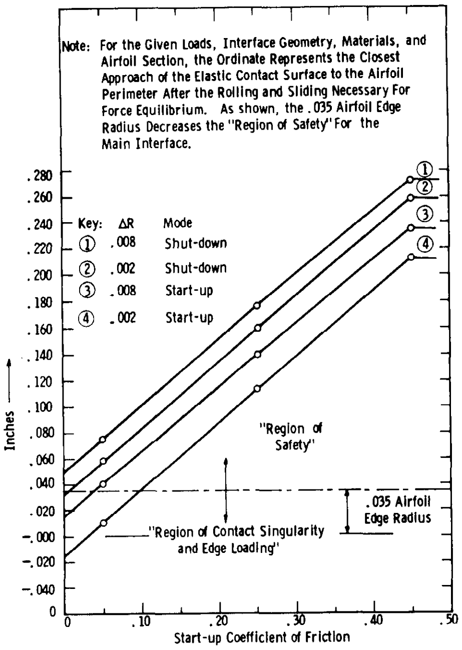

Figure 3-17. Interface Edge Loading Analysis Airfoil-End Cap

(Figure 3-17), the worse possible shift or rearrangement at the interface will not bring the actual load-bearing contact area dangerously close to the edge of the airfoil section for any of the four conditions cited. ΔR represents the difference in radii between the airfoil tenon and the end cap groove or the relative fit of the airfoil with respect to the end cap. The region of safety extends from 0.035 inch. If the contact area moves within 0.035 in of the airfoil edge, edge loading will persist in a region of contact singularity. Figures 3-18 and 3-19 show the effects of radial difference (ΔR) and the coefficient of friction, independently, on the maximum contact tensile stress developed at the interface for the startup and shutdown conditions, respectively. The stress increases directly with radial difference at constant load because the contact area decreases. For the actual case, where part tolerances establish ΔR = 0.004 inch and the measured value of friction is $\mu = 0.25$, the maximum tensile stresses are 8240 psi for startup and 5180 psi for shutdown.

Load transmission at the end cap-insulator interface resembles planar contact because of the large radii. That is, there is little curvature to allow the trade-off of normal and tangential load. Since the vane gas load is reacted almost solely by friction, the spring load is established as a function of friction at the end cap-insulator

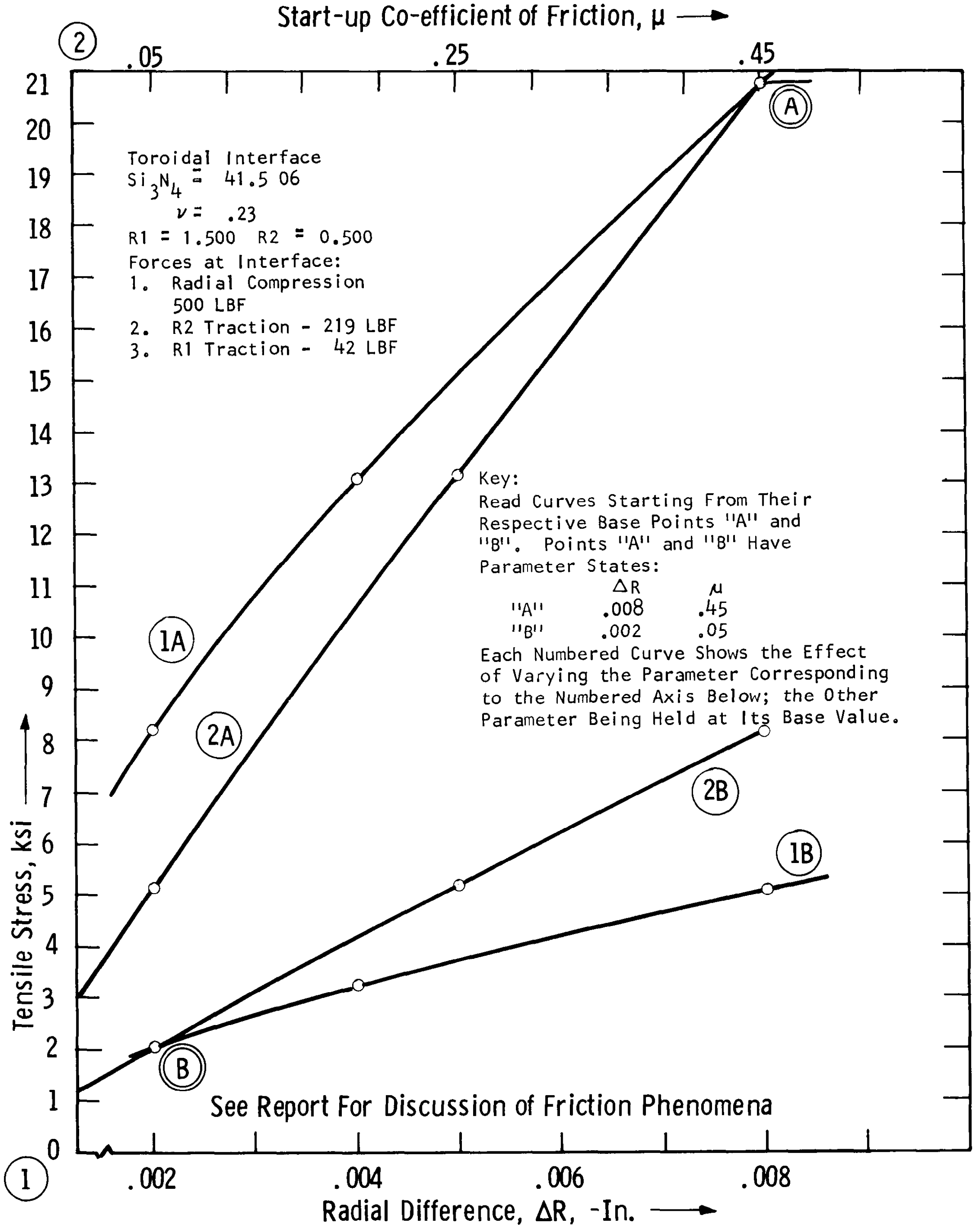

Toroidal Interface
Si_3N_4 = 41.5 06
ν = .23
R1 = 1.500 R2 = 0.500
Forces at Interface:
1. Radial Compression 500 LBF
2. R2 Traction - 219 LBF
3. R1 Traction - 42 LBF

Key:
Read Curves Starting From Their Respective Base Points "A" and "B". Points "A" and "B" Have Parameter States:

	ΔR	μ
"A"	.008	.45
"B"	.002	.05

Each Numbered Curve Shows the Effect of Varying the Parameter Corresponding to the Numbered Axis Below; the Other Parameter Being Held at Its Base Value.

See Report For Discussion of Friction Phenomena

Figure 3-18. Startup Tensile Contact Stress at the Airfoil-End Cap Interface Showing the Effects of Parameter Variation

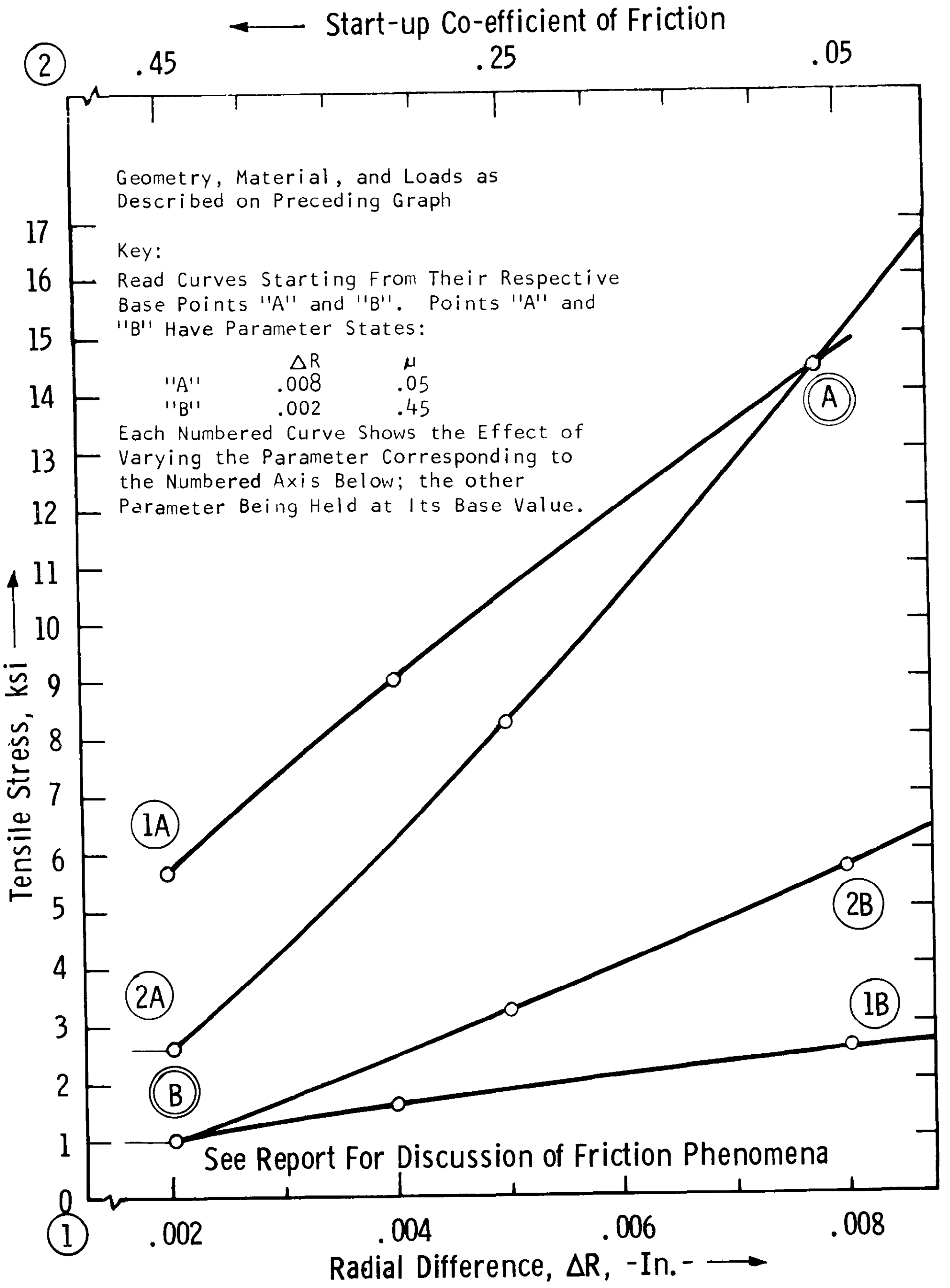

Figure 3-19. Shutdown Tensile Contact Stress at Vane/End Cap Interface Showing Effects of Parameter Variation

interface. The magnitude of stresses generated during thermal transient periods is of concern at the end cap-insulator interface because two dissimilar materials are in contact here without being cushioned by a metal weave. Because of the difference in values of thermal expansion coefficients, a considerable tractive shear force can develop at this surface. The cylindrical analogy was used to estimate an upper bound for this shear and also to define the maximum value of tensile stress. The bound is proportional to the friction coefficient and the maximum Hertzian pressure developed at the interface. The nearly planar nature of the interface makes the Hertzian stress quite small. Therefore, the upper bound is also small.

A combined kinematic and contact stress analysis at the interacting interfaces of four end caps with two insulators was made. The major interface in this system (the contact between the top surface of an outer end cap with the bottom surface of an outer insulator, for example) was considered. The design depends upon friction along a curved surface for positional stability. Since simple contact had to be preserved, the minor radius of curvature was selected within the constraints of friction coefficient. From Figure 3-20 it is clear that a 3.0 inch radius makes the design practically independent of frictional effects, while a 10 inch radius requires a coefficient of friction >0.35 to avoid contact singularity and edge loading. Furthermore, the combined effect of curvature and friction may not be great enough in the case of a large minor radii to prevent movement of the stator vane assembly downstream toward the first stage rotor.

The state of stress at the interface is determined by the minor axial radius (R_2), the end cap/insulator radial difference (ΔR) and the coefficients of friction (μ) between the end cap and insulator materials. The effects of these parameters on the maximum contact tensile stress are plotted independently in Figures 3-21 and 3-22 for turbine startup and shutdown, respectively. Even though the stress varies inversely with the minor axial radius of curvature, stress maxima will only approach 500 psi in the insulator under the least favorable conditions of friction and radial difference ($\mu = 0.15$ and $\Delta R = 0.008$ inch). Contact stresses in the end cap remain lower still.

The first generation stator vane assembly was designed with a large minor radius of curvature at the end cap/insulator interface. When the coefficient of friction between silicon nitride and the insulator material was found to be $\sim$0.10 rather than >0.35, the radius of curvature was reduced on some pieces of test hardware. Several other modifications were also made as a result of this analysis. Analogous to the practice of crowning steel rollers (blending large radii to taper the ends), 0.250 inch edge radii were introduced to alleviate the contact singularities discussed.

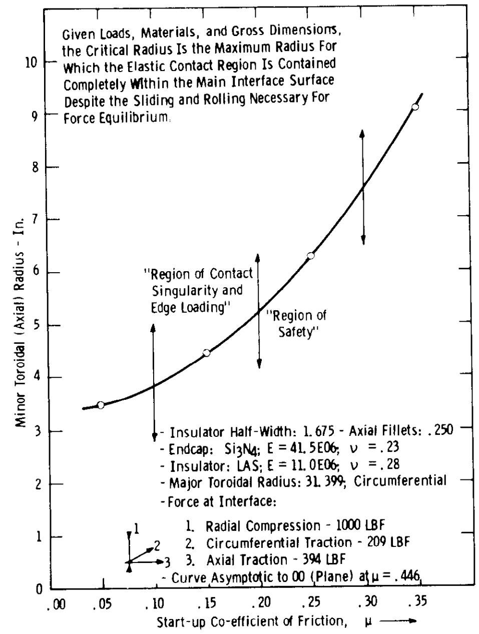

Figure 3-20. Critical Axial Radius vs Startup Coefficient of Friction at End Cap/Insulator Interface

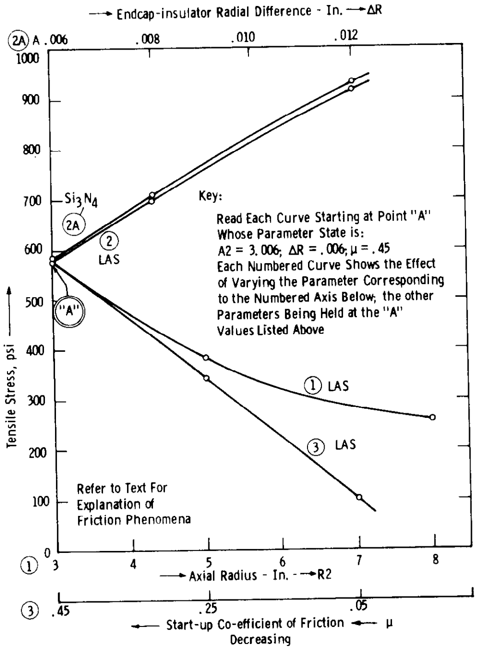

Figure 3-21. Startup Tensile Contact Stress at the End Cap/ Insulator Interface Showing Effects of Parameter Variation

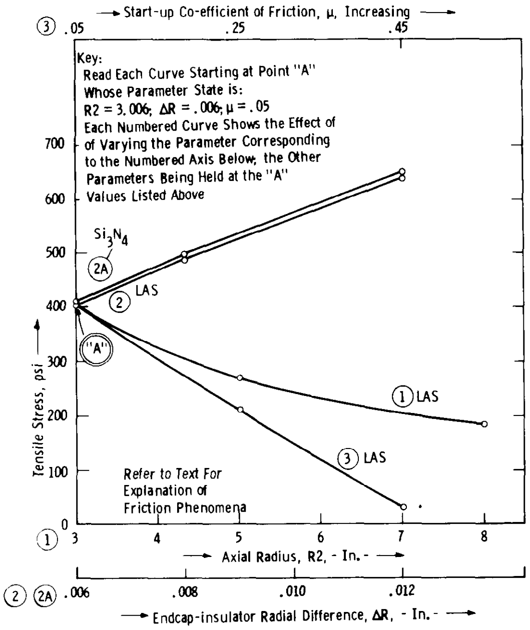

Figure 3-22. Shutdown Tensile Contact Stress at the End Cap/ Insulator Interface Showing the Effects of Parameter Variation

A reduction in the minor axial radius (R_2) eliminated the need for an exact analysis of the contact stress field in the vicinity of a second-order discontinuity (as at the boundary between the end cap and the insulator edge radius). Several qualitative comments may be made, however. Since the Hertzian stress on the fillet side (insulator) must be greater than the main radius side (end cap), the stress field from the friction-reacted tractive loads are expected to be skewed considerably. For the specific case of the simple rolling cylinders, the in-plane stress field, normally associated with traction at the surface, is symmetric with respect to the line of contact. Compressive and tensile stresses develop fore and aft, respectively, in this situation. Whenever the stress field becomes asymmetric as a result of traction applied toward the high pressure side for example, the tensile component increases modestly while the compressive component rises dramatically. The compressive stress at the downstream edge of the 0.250 inch fillets on the insulators may approach 30 ksi in the event of partial edge loading.

Two-inch spherical radius ceramic buttons were inserted within the downstream lip seals to act as final stops to preclude any possibility of sliding (Figure 3-5).

Contact stresses are generated as the thick end caps slide circumferentially to interlock with the thick insulators. The edge locking interference in this case is 0.200 inch, with the circumferencial component of the gas load being transmitted across the flat edge. The load at these interlocks is inversely proportional to the amount of circumferential traction reacted by friction at the major end cap/insulatoror interface. For the lowest coefficient of friction, μ = 0.10, the normal load at the interlocking interface reaches a maximum. Figure 3-23 illustrates the effect of edge radius on the development of contact tensile stresses under these least favorable conditions where the interlock is so skewed that it causes full edge loading.

The metal pivots represent the terminal resistance to the entire circumferential component of the vane gas load. Under the worst condition of tolerance and loading, the maximum shear stress due to pivot contact is 18,700 psi. Two other locations of contact occur, 1) between the insulator and the shoe and 2) between the insulator and the housing ring. Since these areas are cushioned by metal weave material, stresses equal P/A and are considered negligible.

A steady-state thermal stress analysis of the end cap was performed utilizing a plane-wise symmetric finite element plate program. The mesh and loading are shown in Figure 3-24. Although the end cap actually

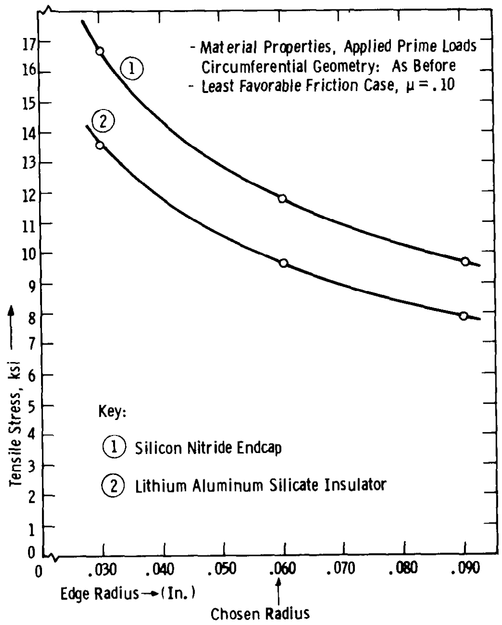

Figure 3-23. Circumferential Edge Loading Analysis of Hertzian Contact Stresses (Tensile) at Thick-Thin End Cap/ Insulator Interlocks

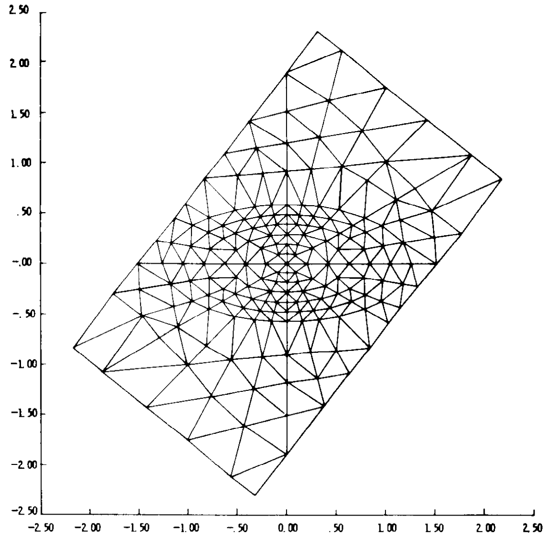

Figure 3-24. Finite Element Geometry - End Cap With Torroidal Groove

had radial sides and a groove with a fourth-order surface perimeter, it was modeled as a rectangular block with an ellipsoidal groove. This model was chosen to approximate both the inner and outer end caps with cavity geometry variable as a function of groove depth. Thermal loading was programmed to reflect temperature drops ranging from 200 to 300°F across the end cap radially. Temperature distribution reflected end cap geometry and was skewed with respect to the sides to present the worst case. The end cap was simply supported at three corners and free at the fourth. It was restrained from thermal bending by a uniform pressure of 8000 psi, the compressive spring load distributed evenly over the contact area.

Six cases were analyzed. The first three were run to determine the effect of end cap groove depth. The maximum principal stress dropped significantly as the limit of the simple rectangular block was approached, as shown in Figure 3-25, where the maximum tensile stress at the center of the groove is plotted versus the thickness of the end cap at that point. Since a symmetric model was used, the finite element results were corrected to account for asymmetry as it actually existed. The correction factor was simply the ratio of stress concentration factors in bending for flat plates which were grooved. The effect is actually

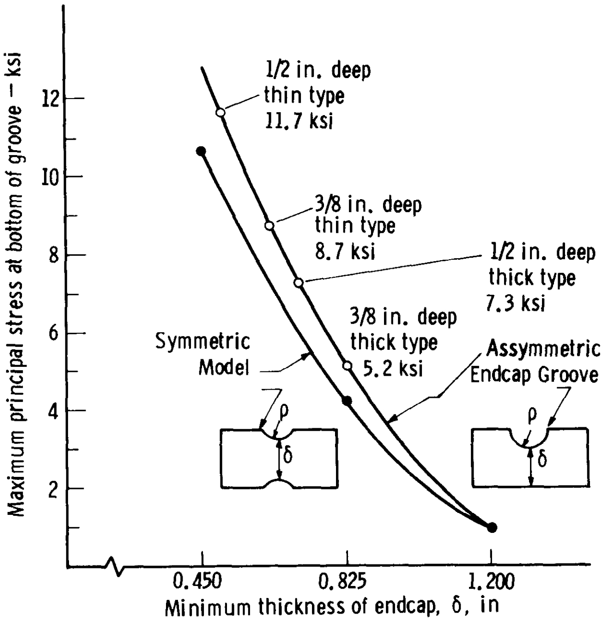

Figure 3-25. Maximum Plate Stress in Outer End Cap Under Thermal Steady State Showing Groove Depth Effect and Adjustment for Asymmetry

more pronounced since the analysis used the same temperature gradient regardless of thickness. From the standpoint of steady-state thermally derived plate stress, a reduction of groove depth from 1/2 to 3/8 inch is desirable. Although an increase in spring load with a corresponding increase in contact stress would be required, the net effect seems beneficial.

The fourth case modeled the stress state in adjacent end caps under a single insulator with temperature loading which represented the mirror image of that previously shown. In case five, the effect of reducing the spring load as a constraint to thermal loading was studied. The results of these runs showed end cap position and spring load to be insignificant as design parameters. Stress reductions of only several hundred psi were realized.

The sixth case compared the stress at the groove bottom to the stress at the thin portion of the end caps defined by the groove perimeter and the end cap edge. Without the groove the maximum tensile stress occurred at the outer periphery of the end cap. The addition of a groove decreased this stress as a function of groove depth, but the maximum stress now occurred at the groove bottom. Since the tensile stress maximum was four times the peripheral stress for useful groove depths, peripheral stresses did not influence the choice of groove depth greatly.

In the area of transient thermal stress analysis, the required cooling flows, inherent leakages, and their effect on the convection coefficients were determined. The design process was iterative because a set of plausible inputs was formulated to produce a temperature-time profile. Where the cooling flow inputs were adjusted to produce a new temperature field which was less severe, the flow adjustments were considered beneficial. The temperature fields of interest were substituted into the finite element plate program to evaluate transient, thermal in-plane stresses. Appropriate superposition of contact and steady-state thermal stresses indicated values of 21,200 psi for the 1.0 inch thick end cap and 16,700 psi for the 1.2 inch thick end cap. Maximum tensile stress occurred near the bottom center of the groove. Stress levels of this magnitude are acceptable for silicon nitride or silicon carbide.

An accurate analysis of heat transfer and the associated stress field within the layered ceramic shroud (end cap, insulator, metal shoe) for both the steady-state and shutdown transient modes was completed for a turbine operating at a gas temperature of 2500°F(4). Gas temperatures were programmed to drop to compressor discharge levels (650°F) in 2.5 seconds followed by an exponential decay to ambient temperature. The heat transfer coefficients were ramped and decayed similarly. External body temperatures were adjusted for heat capacity and also allowed to equilibrate to the surroundings, normally.

For the purposes of the two-dimensional finite element technique employed, temperature gradients across the interfaces were not considered. This approach was taken to present a conservative (high stress bias) view. The interfacial gradients, radially, are high and there are methods of calculating them for use with 2-D steady-state heat transfer analysis. To employ them would serve only to lower the radial temperature gradients in the various component members of the system, thereby reducing the resultant stress levels without affecting the stress distributions appreciably. Convection, conduction and radiation boundary conditions were applied as required, however.

Thermal loading for the calculation of steady-state and transient thermal stress was obtained from a three-dimensional map of temperature versus time. The map itself was constructed from two-dimensional thermal contour sections, representing five radial slices through the shroud stack from leading to trailing edge. The R-Z plane sections: AA, BB, CC, DD, and EE, shown in Figure 3-26, model the end cap with a representative groove, the insulator and the metal shoe. Seventeen heat transfer coefficients, seven gas temperatures and six external body temperatures versus time functions were specified. These functions were derived from

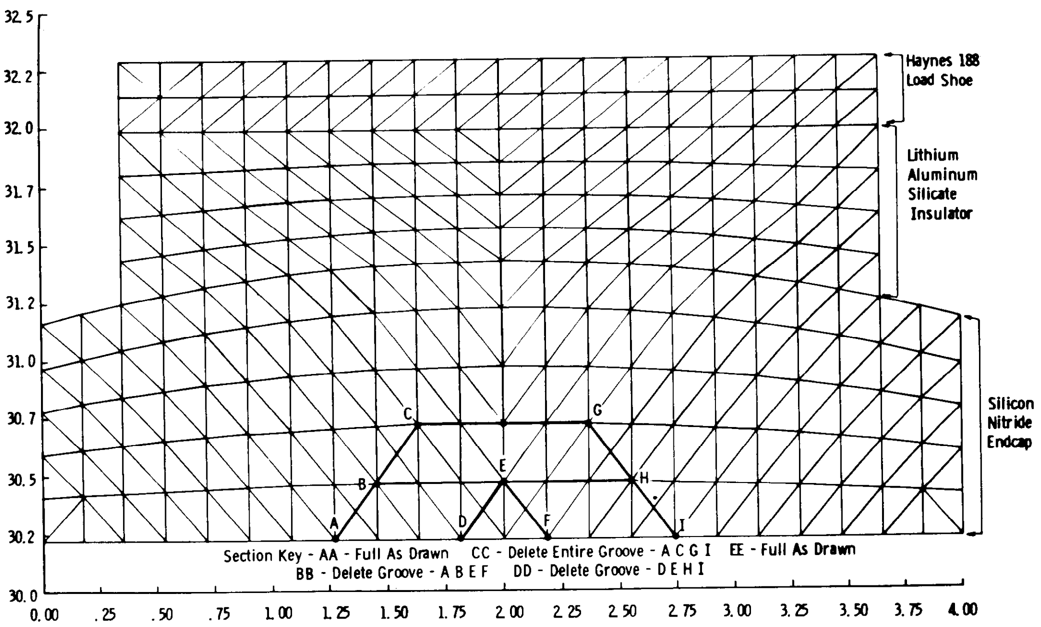
32.5
32.2
32.0
31.7
31.5
31.2
31.0
30.7
30.5
30.2
30.0
0.00
.25
.50
.75
1.00
1.25
1.50
1.75
2.00
2.25
2.50
2.75
3.00
3.25
3.50
3.75
4.00
Haynes 188 Load Shoe
Lithium Aluminum Silicate Insulator
Silicon Nitride Endcap
A
B
C
D
E
F
G
H
I
Section Key - AA - Full As Drawn CC - Delete Entire Groove - A C G I EE - Full As Drawn
BB - Delete Groove - A B E F DD - Delete Groove - D E H I

Figure 3-26. Two-Dimensional Finite Element Mesh for Heat Transfer in the End Cap Sections AA, BB-CC-DD and EE

theoretical considerations or from appropriately scaled turbine conditions. The thermal property data, i.e., emissivity, specific heat and conductivity, were used as functions of temperature.

Thermal contour maps for a typical end cap under steady-state, 5 seconds after shutdown and 60 seconds after shutdown, are shown in Figures 3-27 through 3-32. Sections AA and CC are used to illustrate the influence of the groove on the temperature gradient with respect to time. For the steady-state condition (Figures 3-27 and 3-28), the most severe gradients occur downstream of the groove. This is due, in part, to the turbulent decay of film cooling as it flows over the leading edge to wash across the hot face of the end cap. The cooling air flow on the cool surface is also greater at the trailing edge because a significant pressure drop occurs across the stage. The relatively small thermal gradient appearing between the groove and the insulator results from the boundary condition assumption that the rate of heat flow through the shroud is dominated by convection through the end cap rather than conduction across the interface.

Figures 3-29 and 3-30 describe the stack 5 seconds after quench. Tensile stresses have developed in the lower surfaces as a hot spot

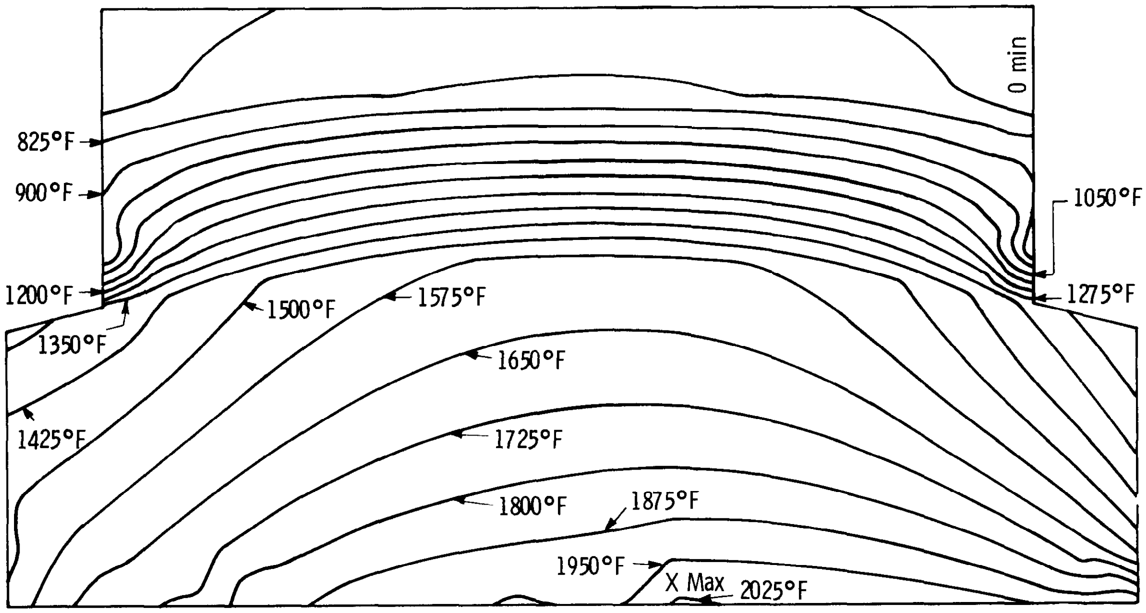
0 min
825°F
900°F
1050°F
1200°F
1275°F
1350°F
1425°F
1500°F
1575°F
1650°F
1725°F
1800°F
1875°F
1950°F
X Max
2025°F

Figure 3-27. Steady-State Thermal Contour Representation Through End Cap Section AA

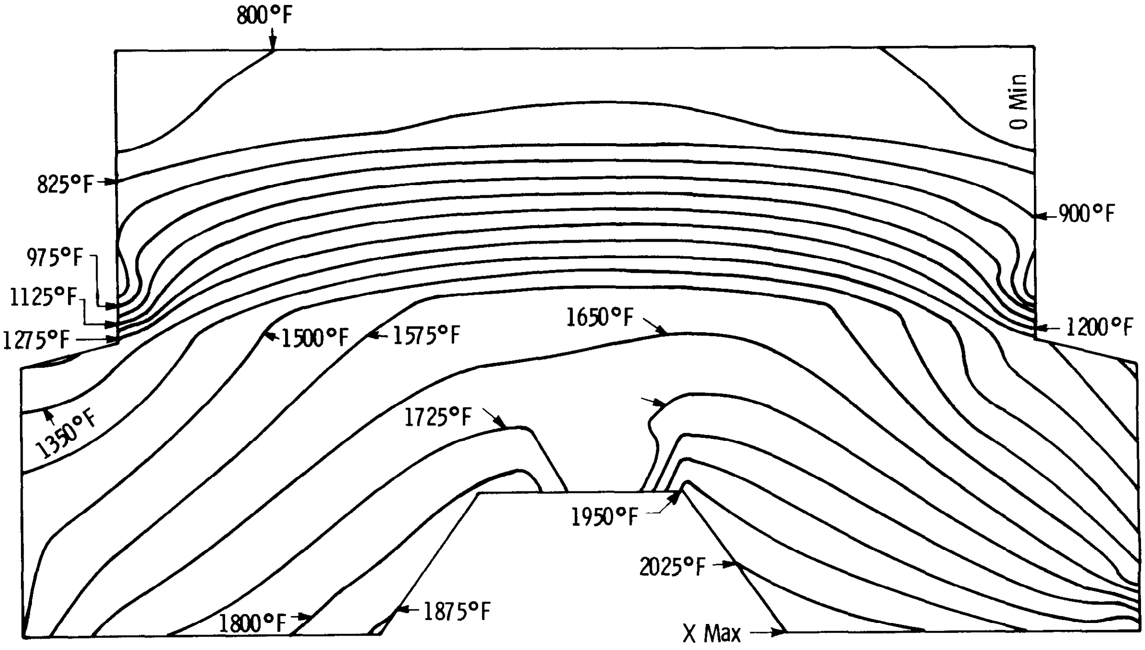
800°F
0 Min
825°F
900°F
975°F
1125°F
1275°F
1200°F
1350°F
1500°F
1575°F
1650°F
1725°F
1950°F
2025°F
1800°F
1875°F
X Max

Figure 3-28. Steady-State Thermal Contour Representation Through End Cap Section CC

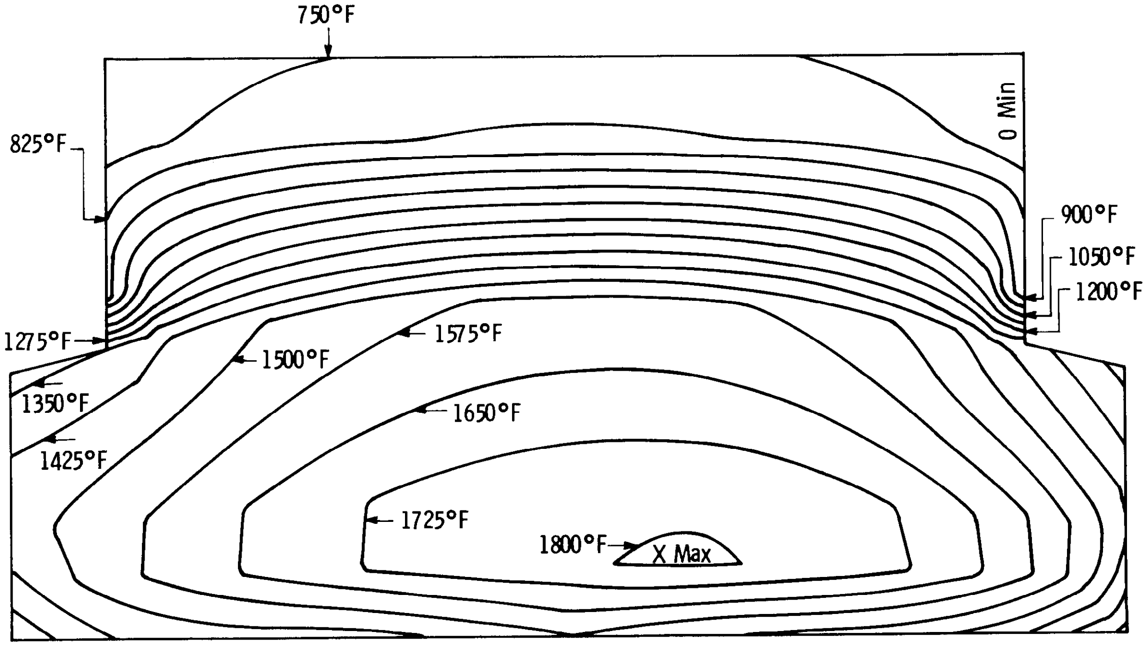
750°F
825°F
0 Min
900°F
1050°F
1200°F
1275°F
1350°F
1425°F
1500°F
1575°F
1650°F
1725°F
1800°F
X Max

Figure 3-29. Thermal Contour Representation Through End Cap Section AA 5 Seconds After Shutdown

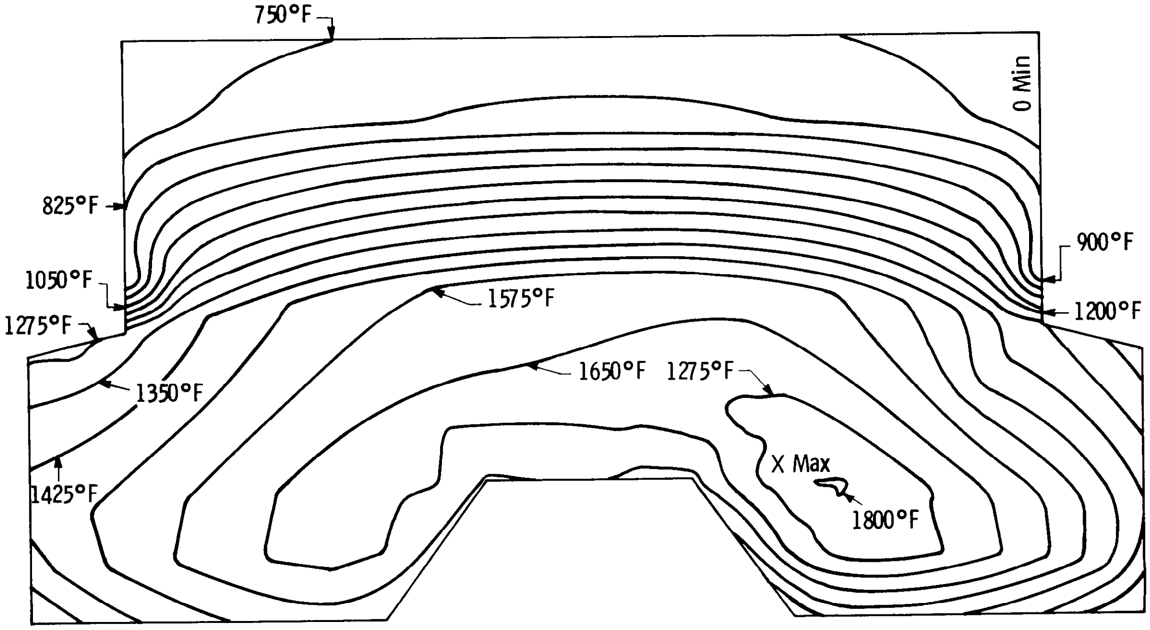
750°F
0 Min
825°F
1050°F
1275°F
900°F
1200°F
1575°F
1650°F
1275°F
1350°F
1425°F
X Max
1800°F

Figure 3-30. Thermal Contour Representation Through End Cap Section CC 5 Seconds After Shutdown

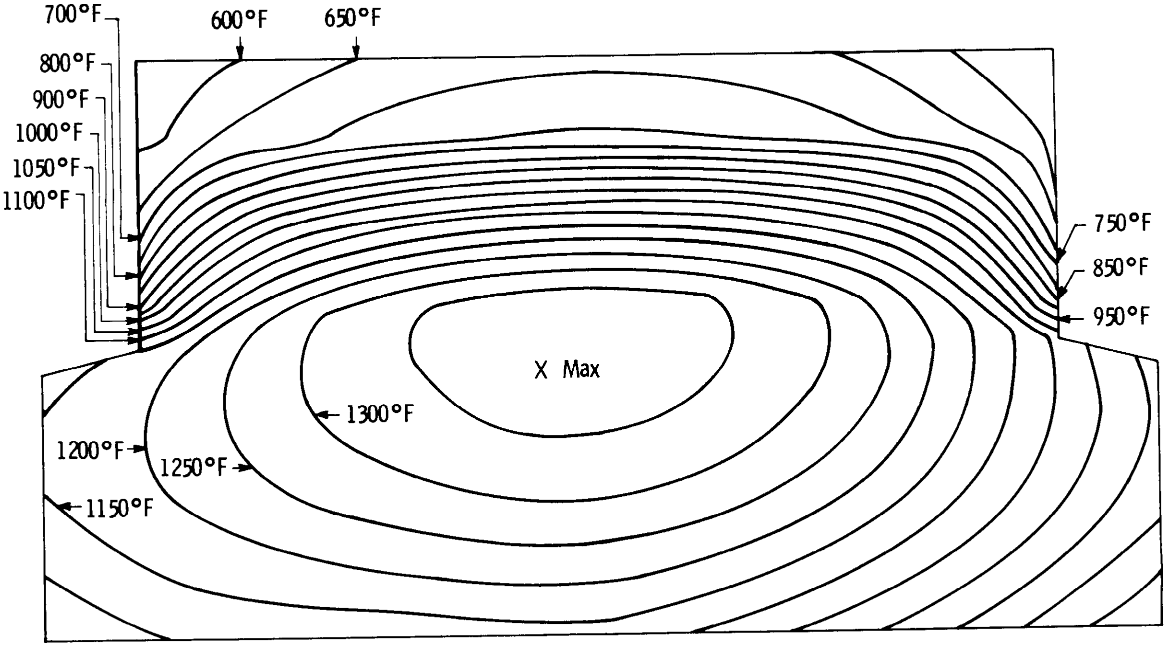
700°F
600°F
650°F
800°F
900°F
1000°F
1050°F
1100°F
750°F
850°F
950°F
X Max
1300°F
1200°F
1250°F
1150°F

Figure 3-31. Thermal Contour Representation Through End Cap Section AA 60 Seconds After Shutdown

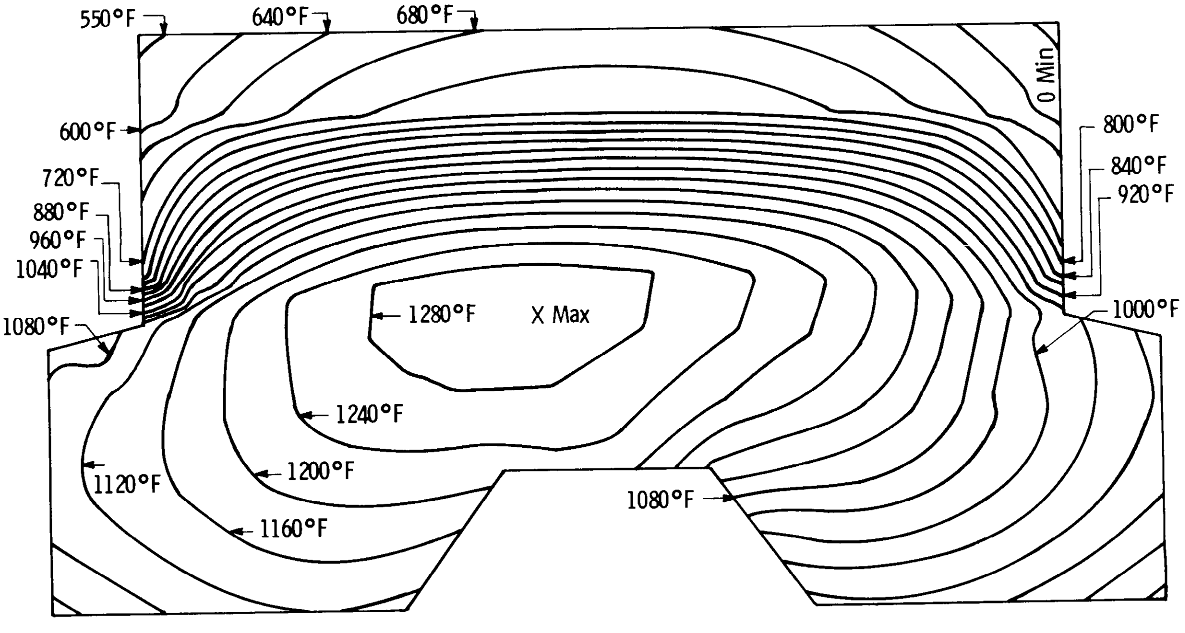
550°F
640°F
680°F
0 Min
600°F
800°F
840°F
920°F
720°F
880°F
960°F
1040°F
1080°F
1280°F
X Max
1000°F
1240°F
1200°F
1120°F
1080°F
1160°F

Figure 3-32. Thermal Contour Representation Through End Cap Section CC 60 Seconds After Shutdown

emerges in a central location. Thermal relaxation occurs after 60 seconds (Figures 3-31 and 3-32) as shown by the general cooling and the slow rise of the hot spot to the end cap/insulator interface.

Because the heat transfer program was, in reality, a two-dimensional axisymmetric representation operating in the R-Z plane, the five sections yield a five-row grid of temperature versus time in the θ-Z plane (normal to the radial axis) in any of the element layers. Unfortunately, this five-row grid does not correspond geometrically to the end cap element mesh, which was chosen to model the groove. Clearly, some rearrangement of temperature values was required to make the two finite element programs compatible. To accomplish this, a two-dimensional Lagrangian interpolating routine was employed to find the exact value of a function of two variables continuously within the region of interest when the function surface was specified by a rectangular grid and was of an order less than or equal to five. This capability was particularly useful for the determination of temperature at points on the hot surface of the end cap in the vicinity of the airfoil and groove where a rather abrupt change occurred from the pressure to suction sides.

Final stress calculations were made from the complete complement of thermal maps. The results of thermal loading in steady-state are plotted as principal isostress lines in the θ-Z plane at the midpoint of the end cap in Figure 3-33. Since the groove region was predominantly in compression, the superposition of the contact stress field did not present a severe problem. Significant tensile stresses occurred in the downstream half of the end cap and in the areas between the edge and the major groove diameter. Fortunately, the magnitude of stress due to contact and thermal loads for steady-state were well below the reported strength of silicon nitride and silicon carbide at the operating temperature.

Final design drawings were prepared for the first generation stator vane assembly. Norton manufactured twenty vane assembly sets from HS130 silicon nitride billets. The first five airfoils of these twenty were not completed with respect to the tenon geometry. They served as demonstration pieces. Eight stator vane assemblies were fabricated from NC203 silicon carbide.

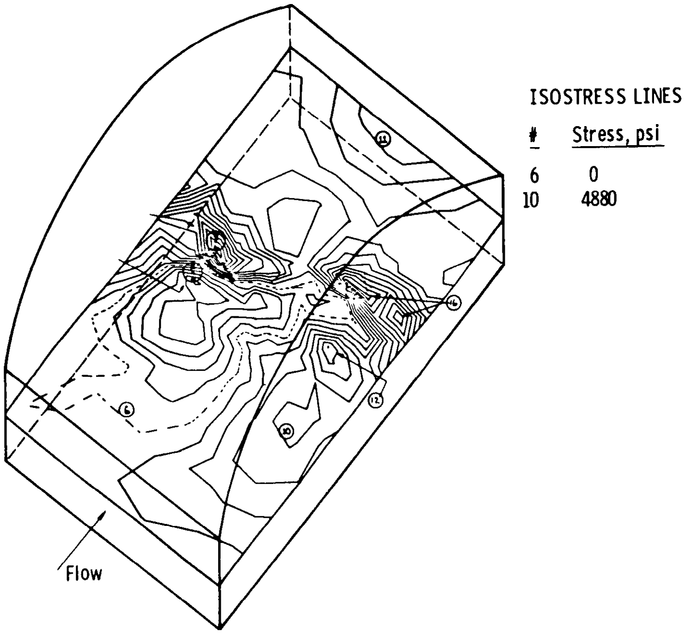
ISOSTRESS LINES
# Stress, psi
6 0
10 4880
11
16
12
10
6
Flow

Figure 3-33. Thermal Stress Distribution in Ceramic End Caps Under Steady-State Conditions

3.4 INSULATOR ANALYSIS - PRELIMINARY DESIGN REQUIREMENTS

A series heat transfer analysis using a one-dimensional model (Figure 3-34) was performed to define the insulator requirements for the vane assembly system. An insulator was necessary to reduce heat transfer by conduction radially outward from the gas stream through the end cap to the metal support and loading structure. The thermal conductivity of either silicon nitride or silicon carbide end caps was too high to prevent excessive heating of the metal substructure indirectly by the gas stream. Permitting air-cooled metal components to be in direct contact with the end caps would impose severe gradients, resulting in steady-state and transient thermal stresses beyond the allowable strength of the end cap materials.

The results of the insulator analysis are presented in parametric form as a function of insulator thickness, t_c, in Figures 3-35 and 3-36. A gas inlet temperature (T_1) of 2500°F was selected. The cooling air temperature (T_6) in the region of the shoe was 800°F. These established an overall gradient ($T_1 - T_6$) of 1700°F through the system. Since the convective heat transfer coefficient (h_a) at the gas end cap surface varied from 100 Btu/ft^2-hr-°F at the leading edge of the airfoil to 400 Btu/ft^2-hr-°F at the trailing edge and the convective heat transfer coefficient (h_e) at the shoe location can be controlled by special nozzling to yield values from 25 to >100 Btu/ft^2-hr-°F, a conservative approach was taken by selecting h_a = 400 Btu/ft^2-hr-°F and h_e = 100 Btu/ft^2-hr-°F, with values for thermal conductivity from Figure 3-37 as follows:

End Cap (Si_3N_4), K_b(min) = 85 Btu inch/hr-ft^2-°F

Insulator, K_c(max) = 18 Btu inch/hr-ft^2-°F

Shoe, K_d(max) = 200 Btu inch/hr-ft^2-°F

The heat flux, Q = 25,500 Btu/ft^{2}hr, remained constant through all components.

Under steady-state conditions, the hot face of the end cap reached 2435°F in a 2500°F gas stream. A 300°F thermal gradient was sustained across the 1-inch thick silicon nitride end cap to produce a temperature of 2135°F at the end cap/insulator interface. The temperature at the surface of the shoe in contact with 800°F cooling air was 1055°F, but a small gradient across the shoe (35°F for 0.25 inch thickness) raised the temperature at the shoe-insulator interface to 1090°F. Therefore, a maximum thermal gradient of 1045°F was established across the insulator.

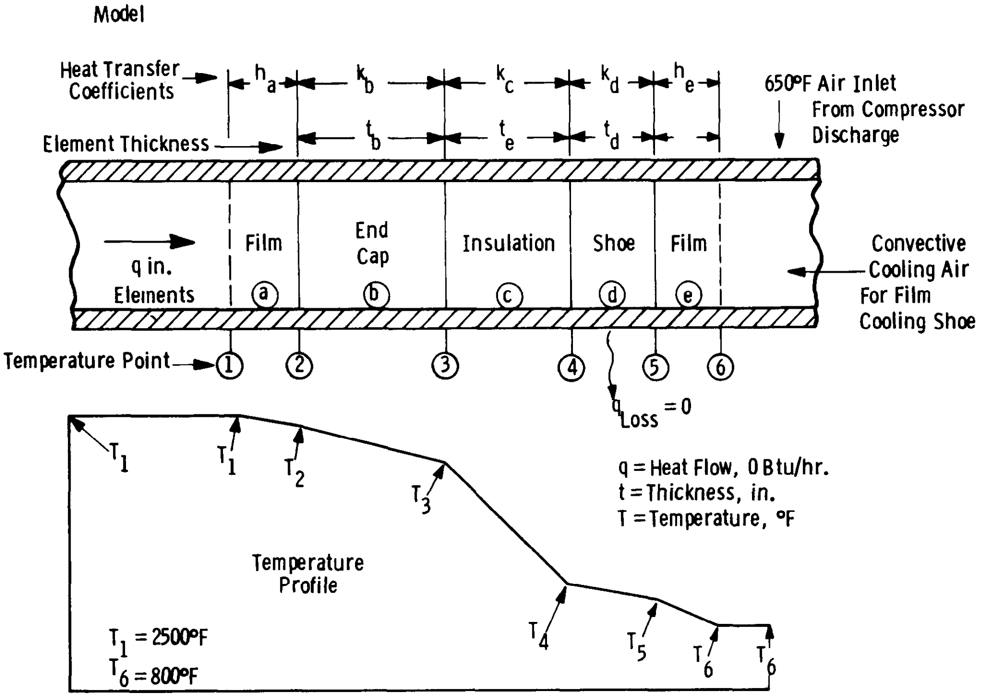

Model
Heat Transfer Coefficients
h_a
k_b
k_c
k_d
h_e
Element Thickness
t_b
t_e
t_d
650°F Air Inlet From Compressor Discharge
q in.
Elements
Film
(a)
End Cap
(b)
Insulation
(c)
Shoe
(d)
Film
(e)
Convective Cooling Air For Film Cooling Shoe
Temperature Point
①
②
③
④
⑤
⑥
$q_{Loss} = 0$
T_1
T_1'
T_2
T_3
T_4
T_5
T_6
T_6'
q = Heat Flow, 0 Btu/hr.
t = Thickness, in.
T = Temperature, °F
Temperature Profile
T_1 = 2500°F
T_6 = 800°F

Figure 3-34. Preliminary 1-D Radial Steady-State Conduction/Convection Heat Transfer Analysis - Simplified Ceramic Vane Assembly Model and Temperature Profile

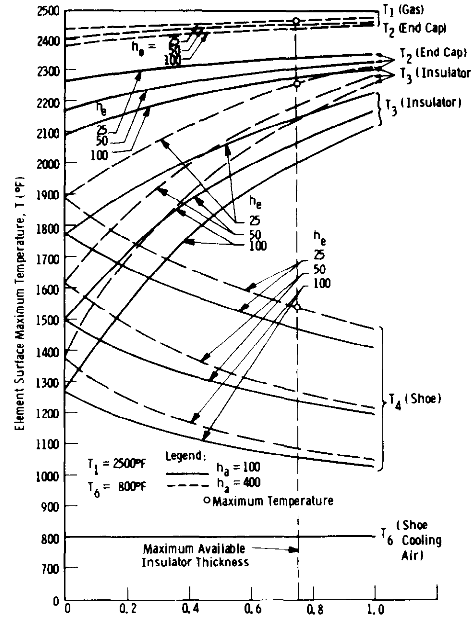

Figure 3-35. Preliminary 1-D Radial Steady-State Conduction/ Convection Heat Transfer Analysis - Effect of Insulator Thickness on Surface Temperature

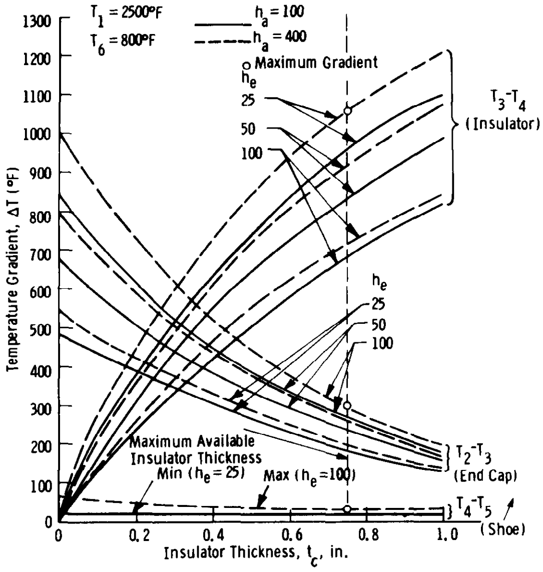

Figure 3-36. Preliminary 1-D Radial Steady-State Conduction/Convection Heat Transfer Analysis - Effect of Insulator Thickness on Temperature Gradients Within Components

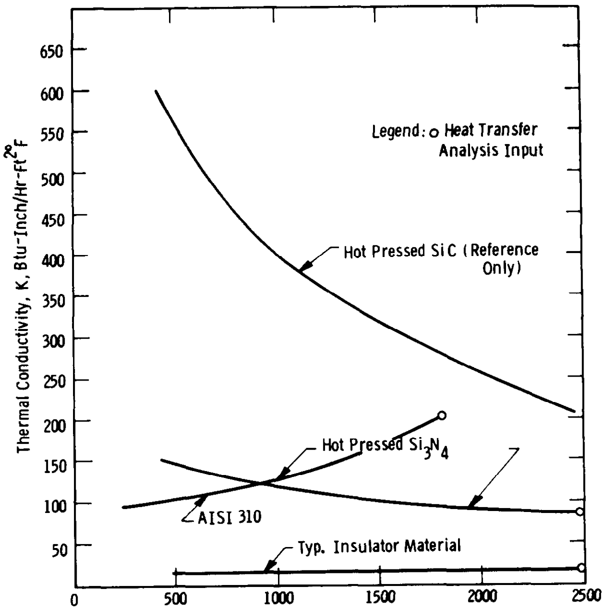

Figure 3-37. Thermal Conductivity of End Cap, Typical Insulator and Shoe Materials

A cursory review of low conductivity materials indicated that reaction sintered silicon nitride or high density stabilized zirconia would meet the insulator requirements. Other porous refractories were considered too friable for gas turbine applications. LAS (lithium aluminum silicate) did not appear to be a viable candidate, considering temperatures at the end cap/insulator interface, even though its low coefficient of thermal expansion would ensure a state of low thermal stress in the insulator under steady-state and transient conditions.

3.5 THE KINEMATIC MODEL

With the system design established and the first generation stator vane design finalized, Westinghouse decided to build a full-scale kinematic model(3) to demonstrate design viability before proceeding to the preliminary design of hardware for the 2200°F static rig tests. The model is shown in Figure 3-38. All components are represented including 1/8th segments of the inner and outer support rings which complete the

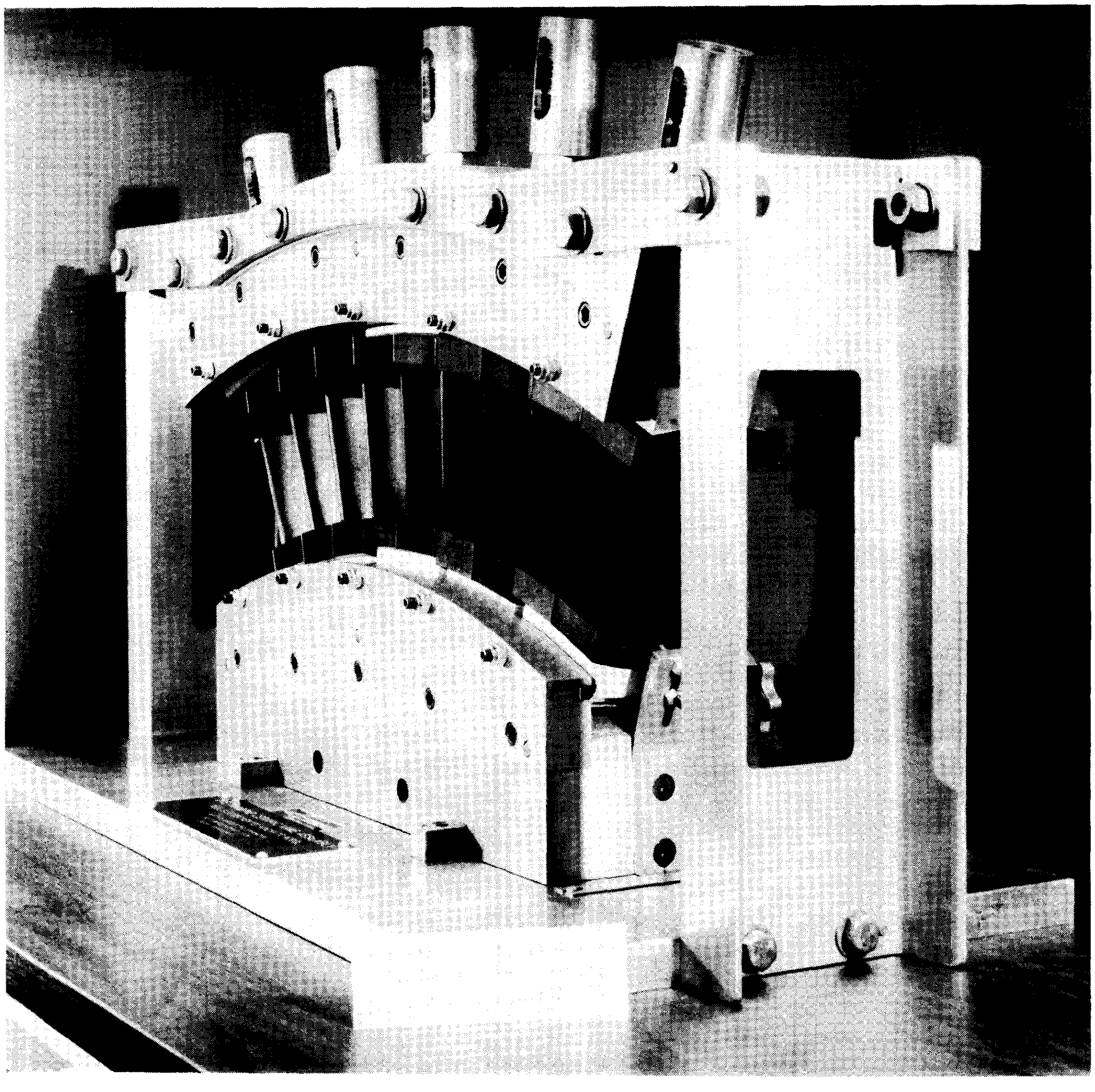

Figure 3-38. Kinematic Model of the Three-Piece Ceramic Vane Design with Support Structure

ten-vane sector configuration of a gas turbine supplied with hot gas from one of eight combustors normally located in a circumferential array. The stator vane airfoil elements were molded from plastic. End caps and insulator components were machined from aluminum and anodized to simulate appropriate color. Shoes, pivots, springs and ring segments were made from mild steel. Specifications and established tolerances were maintained throughout all aspects of fabrication and assembly. Lighter springs were employed to reduce spring loading greatly from the specified 600 lb bundling force. This was done to avoid deformation and damage to the plastic airfoils. Function remained unaffected by the change, however.

The model demonstrates the unique feature of the three-piece design, a freedom of motion at the critical transition location (end cap/airfoil interface) to compensate for differential thermal expansion of the inner and outer support rings without imposing residual stresses on the airfoils. An adjustment screw and scale were provided to permit controlled axial movement of the inner support. The assembly can be moved 0.50 inch or five times the maximum displacement expected in turbine operation without disturbing the integrity of the design. By eliminating the transition from airfoil to shroud, thermal stresses were reduced significantly because temperatures and thermal gradients in both the end caps and airfoils were separated within individual elements of simple, relatively uniform cross section. End caps and airfoils were made, essentially, mutually exclusive with respect to thermal stress and thermal strain by virtue of the interface except for the effect of conductive heat transfer across the interface. Thermal strain was accommodated within the individual element with little or no residual effect on the element adjacent to it radially or circumferentially.

The ten-vane segment configuration used in the kinematic model represented the first generation Si_3N_4 airfoil and end cap assembly scheduled for initial static rig testing. It is obvious from the large gaps which appear at the trailing edges of the nontapered, nontwisted airfoil sections that aerodynamic performance was not of primary concern in this first generation design. Emphasis was placed exclusively on the mechanical aspects of the stator vane design concept in an effort to establish a brittle material's capacity for survival in a high temperature gas turbine environment. Tolerances were carefully selected to avoid making contact between the airfoil tenon area and the edge of the end cap groove. Generous radii were provided throughout to eliminate possible areas of stress concentration.

The model subsequently served as a convenient assembly checkout device for actual static rig test component hardware.(7) It was assembled using end caps and insulators with major radii of 3 inches rather than 8 inches, for example. Airfoils and end caps of second and third generation design were inserted to assess the effect of end cap groove depth and airfoil tenon geometry changes on the freedom of relative motion and accommodation at the interface.

3.6 SECOND GENERATION VANE ASSEMBLY DESIGN

The second generation ceramic stator vane assembly design(4,5) (Figure 3-39) represented an early attempt to correct aerodynamic deficiencies inherent in the first generation design. A tapered-twisted airfoil section was specified to provide uniform gas flow in a full scale rotating turbine. The tenons at both ends of the airfoil were developed more fully in the fashion of a dog bone to eliminate unfilled portions of the end to cap cavities. In effect, the minor tenon radius was extended beyond the airfoil surface boundary to fit and fill the entire end cap cavity. The major airfoil tenon radius was increased to one-half the appropriate chord width at either end to provide for the uniform blending of the tenon into the trailing edge. Without the requirement for trailing edge relief, the prominent slot between end cap and airfoil was eliminated. These changes in the airfoil tenon geometry accounted for a subtle but significant difference in the position of the airfoil loading axis.

Mechanical improvements were also initiated as a result of stress analysis and friction measurements. The depth of the groove in the end cap, for example, was reduced approximately 12 percent or 1/8 inch to ∿3/8 inch to decrease the maximum principal stress at the bottom of

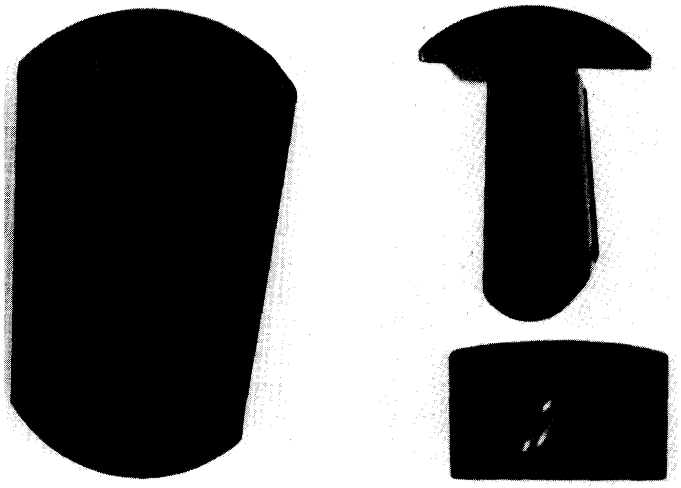

Figure 3-39. The Second Generation Ceramic Stator Vane Assembly Design

the groove from 11,700 to 8700 psi. The major radius of curvature at the end cap/insulator interface was reduced from 8 inches to 3 inches to ensure stability irrespective of the friction coefficient of silicon nitride or silicon carbide with the insulator material. Since both axial and torsional components of the gas load act upon this interface, positive location must be maintained for proper stator vane alignment.

The airfoil/end cap interface was designed to prevent edge loading, a probable cause of catastrophic failure in either an airfoil or end cap.(6) Edge loading can occur whenever displacements of contact center are large enough to reduce the actual contact area. For example, if the nominal contact surface moves beyond the extent of pieces in contact in an effort to achieve kinematic equilibrium under load, a much higher stress field or region of contact singularity will be created. To preclude any such singularity, the center of contact under conditions of zero load must be located within the airfoil cross section to provide adequate vane area for full area contact after displacement. The contact conditions most likely to cause the edge loading effect for any interface geometry are the two extremes in the coefficient of sliding friction, i.e., $\mu_{su} = 0.45$ and $\mu_{su} = 0.05$. If the friction coefficient is high, the condition which occurs when the interface is hot, the center of contact tends to remain at the zero load position with the contact area on the concave side of the airfoil. When the friction coefficient is low, a larger increment of the gas load is reacted by normal forces across the interface and large shifts in the center of contact occur. In this case, the contact area moves toward the convex side of the airfoil.

Elliptical contact areas are projected against the vane cross section of an inner interface position in Figure 3-40 where $\Delta R = 0.002$ inch, the minimum design difference in the vane and end cap torroidal radii is represented. Here, the center of contact at zero load is located in the wider section of the airfoil near the leading edge where there is enough vane area to prevent edge loading of the vane on either the concave or convex side. At higher values of ΔR, the contact area becomes smaller. This establishes greater distance between the contact area and the airfoil perimeter. The hot contact tensile stresses increase directly as a function of the radial difference of contact area. The effect of sliding friction coefficient and radial difference of contact area on the maximum tensile stress due to contact is shown in Figures 3-41 and 3-42, where maximum and minimum stress for the conditions specified appear at points A and B, respectively. The maximum value of contact tensile stress under startup conditions is 16,500 psi for $\mu_{su} = 0.25$ and $\Delta R = 0.008$. At shutdown, the maximum anticipated value of contact tensile stress is 17,000 psi where $\Delta R = 0.008$ and $\mu_{su} = 0.05$. The design was predicated on the highest allowable contact stress to preclude any possibility of edge loading in the vane assembly. Because of manufacturing considerations and a request from the vendor, the

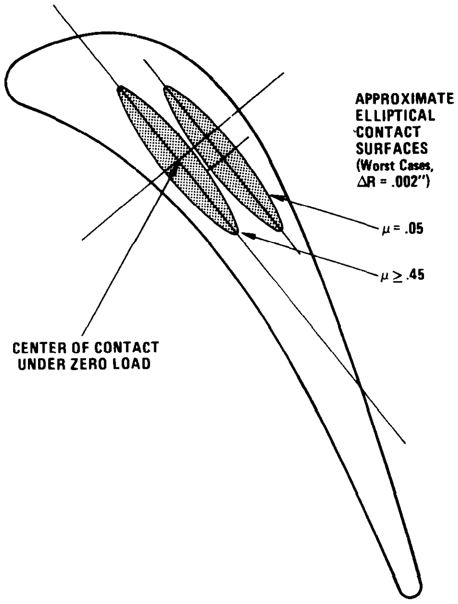
APPROXIMATE ELLIPTICAL CONTACT SURFACES (Worst Cases, ΔR = .002")
μ = .05
$\mu \geq$ .45
CENTER OF CONTACT UNDER ZERO LOAD

Figure 3-40. Vane Cross Section Showing Elliptical Contact Surface Projections for the Worst Contact Conditions at the Inner Airfoil/End Cap Interface

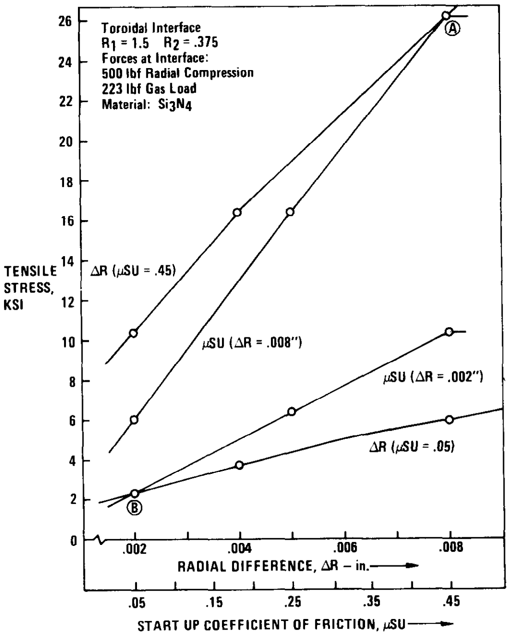

Figure 3-41. Startup Tensile Contact Stress at Airfoil/End Cap Interface Showing Effects of Parameter Variation

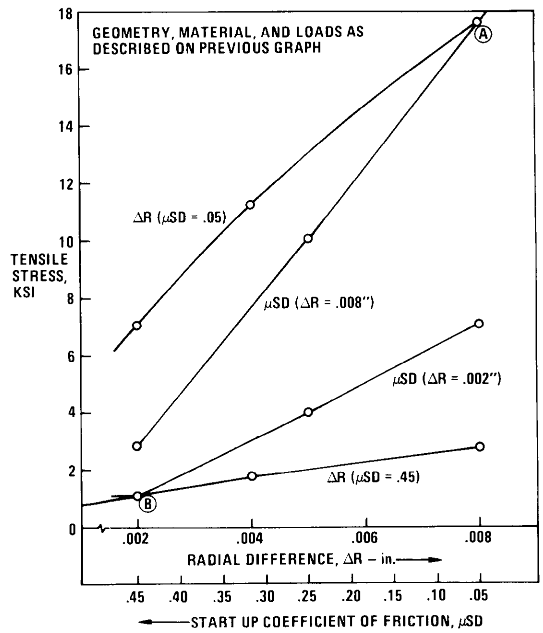

Figure 3-42. Shutdown Tensile Contact Stress at Airfoil/End Cap Interface Showing Effects of Parameter Variation

resulting radial difference between the mating surfaces at the airfoil tenon/end cap cavity interface was specified finally as 0.002 inch, minimum, and 0.012 inch, maximum. Edge radii of 0.060 inch were provided overall to reflect the results of the radii effects study appearing in Figure 3-43.

The second generation airfoil design was subjected to a preliminary transient thermal analysis(6) to test whether acceptable stress levels had been achieved by the mechanical-aerodynamic optimization design process. Boundary conditions for parabolic surface temperature decay from a constant 2500°F to 350°F in 80 seconds were established using a half-airfoil model in which symmetry about any line perpendicular to the radial direction was assumed. The airfoil cross section at its end cap cavity entrance location is illustrated in Figure 3-44. The finite element model with typical values of maximum principal stress resulting from thermal deformations at the nodal points appears in Figure 3-45. The greatest maximum principal stress (166,000 psi) occurred 8 seconds after shutdown in the region where the geometric approximation of the finite element model was the poorest, i.e., the transition region between the airfoil and tenon at the leading edge.

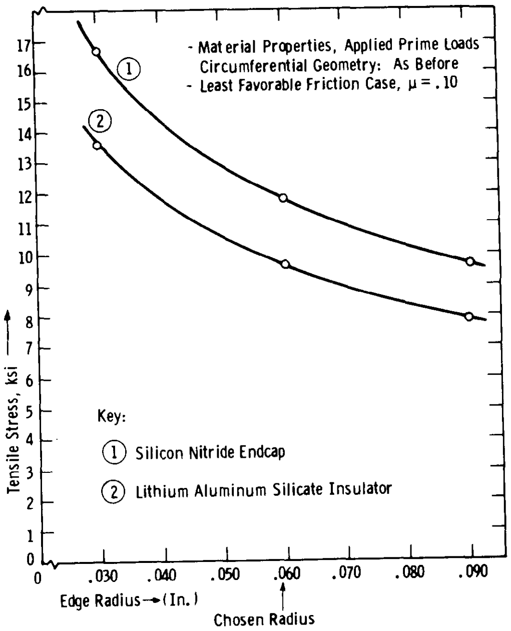

Figure 3-43. Circumferential Edge Loading Analysis of Hertzian Contact Stresses (Tensile) at Thick-Thin End Cap/Insulator Interlocks

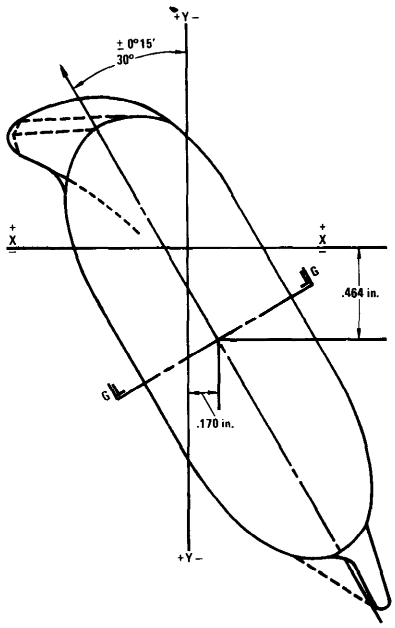
+Y-
± 0°15'
30°
+X-
+X-
G
.464 in.
G
.170 in.
+Y-

Figure 3-44. Second Generation Airfoil Cross Section at the End Cap Surface

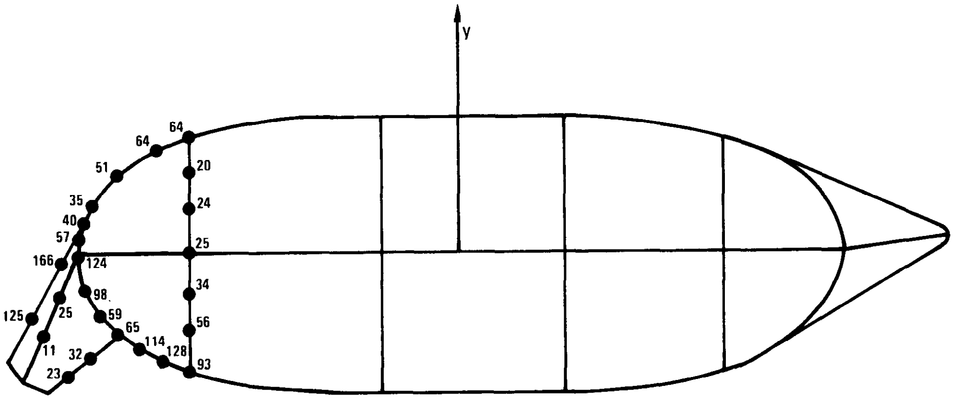

Figure 3-45. Finite Element Model of Airfoil Section With Representative Stress Values (ksi)

When a standard check incorporated into WISEC (Westinghouse Three-Dimensional Isoparametric Finite Element Code) confirmed the possibility of inaccuracy in the vicinity of this critical leading edge location, the analysis was rerun using a modified finite element model. These results are shown in Figure 3-46. Maximum principal stresses are indicated at the nodal points; temperatures appear in parentheses.

Although the preliminary stress analysis did not support design viability, the vagueness of results and questions concerning the qualifying assumptions suggested further three-dimensional stress analysis(7) before a final decision to discard the design. The analysis was repeated using the asymmetric condition of the tapered-twisted airfoil interacting with an end cap. Only the outer end cap location was considered, however, because principal stress maxima occurred there. At the inner end cap location, the overall stress distribution is proportionate but lower. Interference to cause high contact stresses along the mating surfaces of the end cap/airfoil interface was also considered for a steady-state case at 2500°F peak temperature. Other qualifying assumptions were similar to those stated previously. Silicon nitride was assumed to be homogeneous, isotropic and elastic at all temperatures and loading rates. The contact forces (between airfoil and tenon end caps)

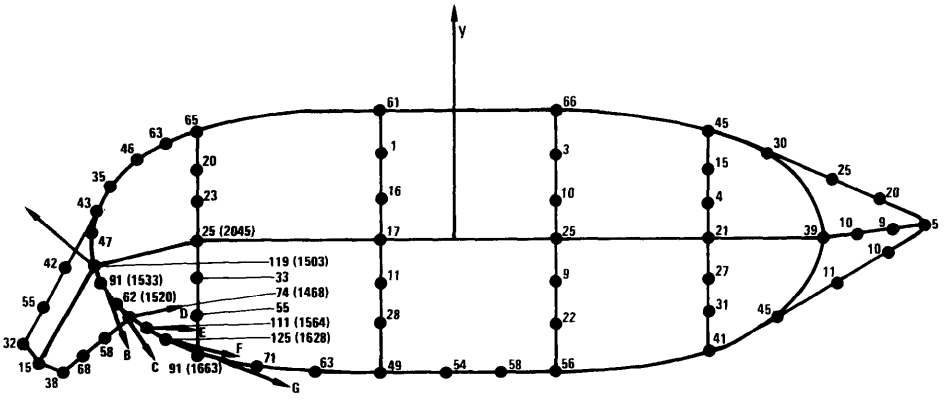
y
61
66
45
30
25
20
5
9
10
10
11
39
65
63
46
35
43
47
42
55
32
15
38
68
58
B
C
91 (1663)
71
63
G
F
E
D
20
23
25 (2045)
119 (1503)
33
74 (1468)
55
111 (1564)
125 (1628)
91 (1533)
62 (1520)
1
16
17
11
28
49
54
58
3
10
25
9
22
56
15
4
21
27
31
41
45

Figure 3-46. Modified Finite Element Model Showing Principal Stresses (in ksi) and Selected Temperatures (in °F)

and the gas load were considered to be negligible. Transient thermal analyses were performed for two conditions of shutdown, i.e., flameout (∿350°F/sec) and controlled at 25°F/sec.

The initial and boundary conditions for the end cap thermal analysis are shown superimposed upon the actual end cap geometry in Figure 3-47. Heat transfer data for the airfoil and outer end cap are presented in Figure 3-48. The three-dimensional element models for the second generation airfoil and an end cap appear in Figures 3-49 and 3-50, respectively.

Temperature and stress contours for the airfoil at Sections 7a (midplane), 3, and 6a (Figure 3-50) are illustrated in Figures 3-51, 3-52 and 3-53, respectively. Under flameout conditions from 2500°F, the maximum principal stress at midplane reached 72,300 psi after 10 seconds. A stress concentration and high stress gradient occurred in the vicinity of the upper and lower tenons. This result was attributed to the arbitraty use of a lower heat transfer coefficient at the airfoil tenon contact surface. The maximum principal stress in the airfoil occurred on the pressure side near the trailing edge. If the value of h was not reduced at the contact surface, but rather considered to be

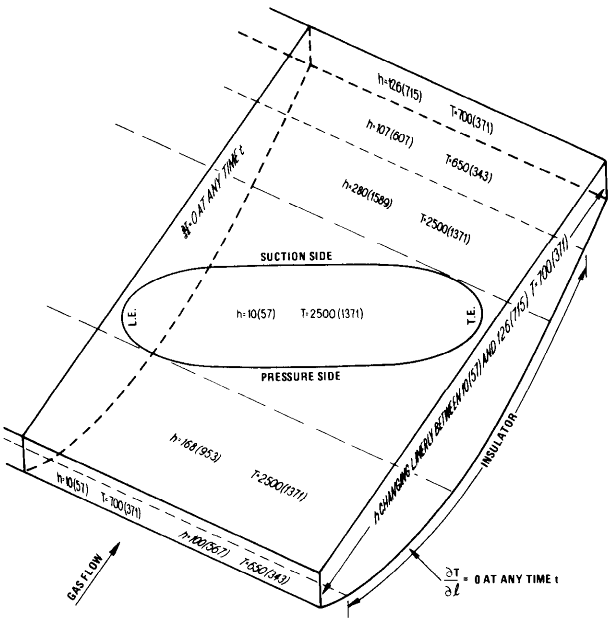
h=126(715)
T=700(371)
h=107(607)
T=650(343)
h=280(1589)
T=2500(1371)
∂T/∂ℓ=0 AT ANY TIME t
SUCTION SIDE
L.E.
h=10(57)
T=2500(1371)
T.E.
PRESSURE SIDE
h CHANGING LINEARLY BETWEEN 10(57) AND 126(715) T=700(371)
INSULATOR
h=168(953)
T=2500(1371)
h=10(57)
T=700(371)
h=100(567)
T=650(343)
GAS FLOW
∂T/∂ℓ = 0 AT ANY TIME t

Figure 3-47. Initial and Boundary Conditions for End Cap Thermal Analysis (h = Btu hr^{-1} ft^{-2} °F, T = °F)

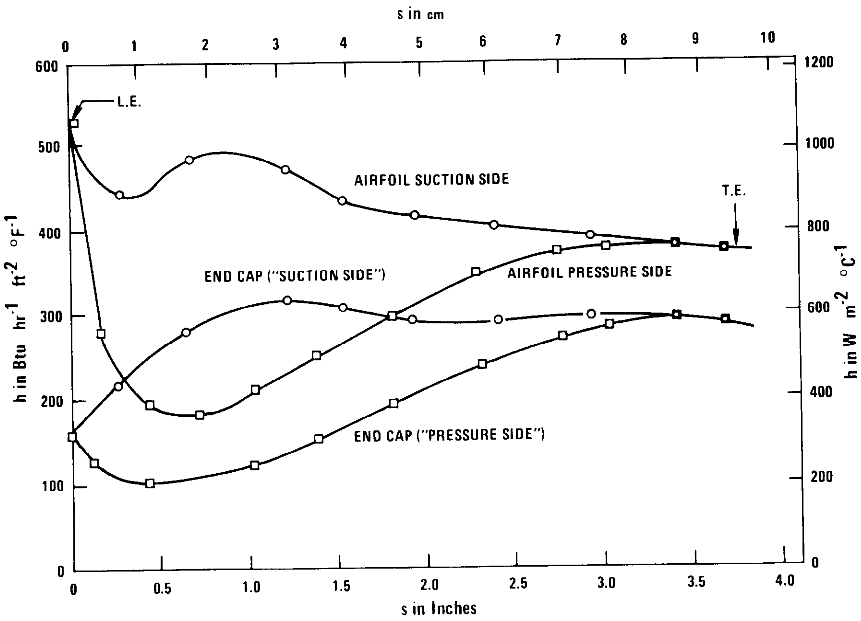

Figure 3-48. Calculated Variations in Heat Transfer Coefficients as a Function of Distance from the Leading Edge for the Airfoil Section at Mid-Height and the End Cap Surface

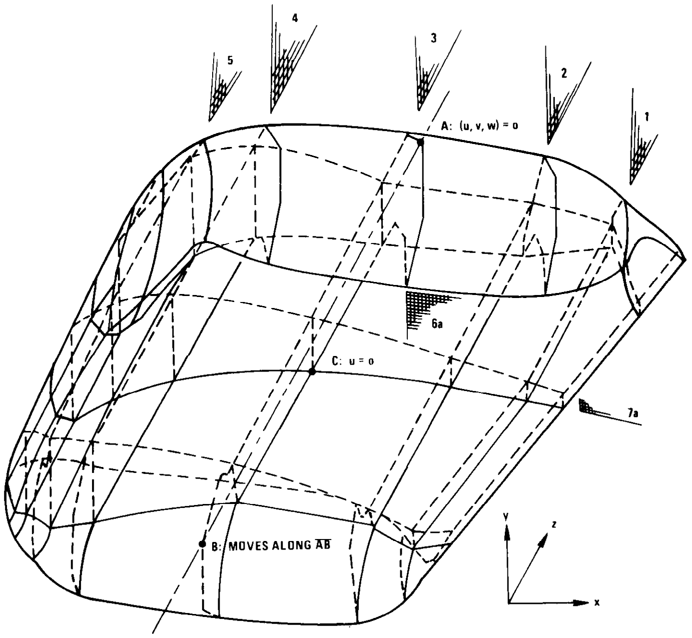
4
5
3
2
1
A: (u, v, w) = o
6a
C: u = o
7a
B: MOVES ALONG $\overline{AB}$
y
z
x

Figure 3-49. Three-Dimensional Element Model of the Second Generation Airfoil Under Equilibrium Conditions

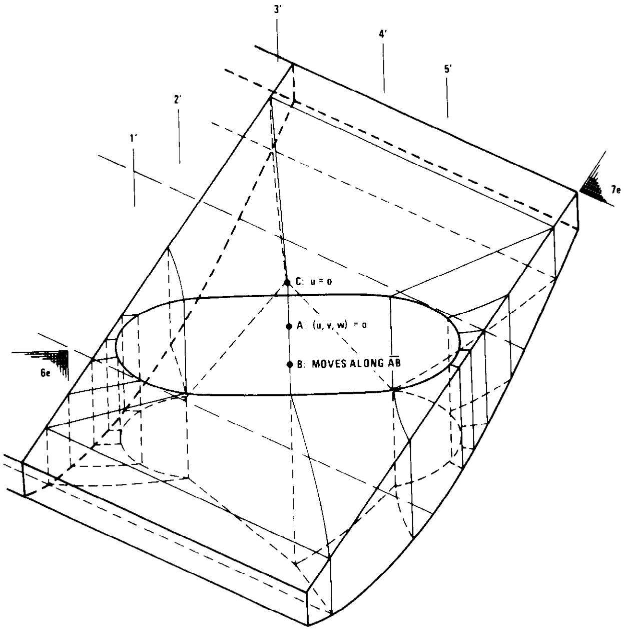
3'
4'
5'
2'
1'
7e
C: u = o
A: (u, v, w) = o
B: MOVES ALONG $\overline{AB}$
6e

Figure 3-50. Three-Dimensional Element Model of the End Cap Under Equilibrium Conditions

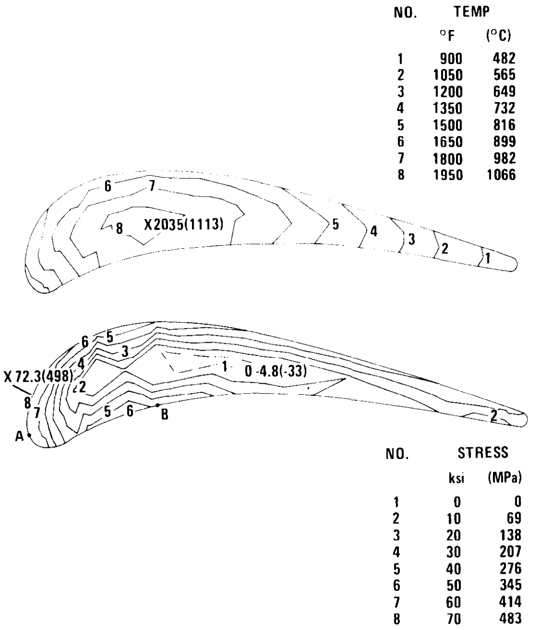
NO. TEMP °F (°C)
1 900 482
2 1050 565
3 1200 649
4 1350 732
5 1500 816
6 1650 899
7 1800 982
8 1950 1066
X2035(1113)
X 72.3(498)
0 -4.8(-33)
A
B
NO. STRESS ksi (MPa)
1 0 0
2 10 69
3 20 138
4 30 207
5 40 276
6 50 345
7 60 414
8 70 483

Figure 3-51. Temperature and Stress Distributions for Second Generation Design Airfoil 10 Seconds After Flameout from 2500°F Steady-State Gas Temperature (Section 7a) (h: High-Low)

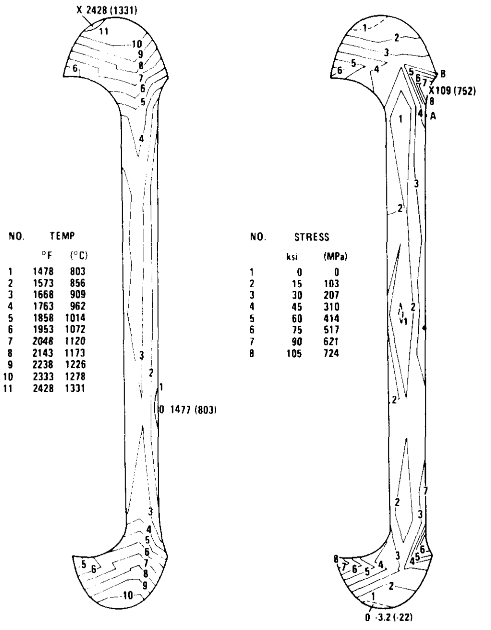
X 2428 (1331)
0 1477 (803)
NO. TEMP °F (°C)
1 1478 803
2 1573 856
3 1668 909
4 1763 962
5 1858 1014
6 1953 1072
7 2048 1120
8 2143 1173
9 2238 1226
10 2333 1278
11 2428 1331
NO. STRESS ksi (MPa)
1 0 0
2 15 103
3 30 207
4 45 310
5 60 414
6 75 517
7 90 621
8 105 724
X109 (752)
A
B
0 -3.2 (-22)

Figure 3-52. Temperature and Stress Distributions for Airfoil Section 3 Ten Seconds After Flameout from 2500°F Steady-State Gas Temperature (h: High-Low)

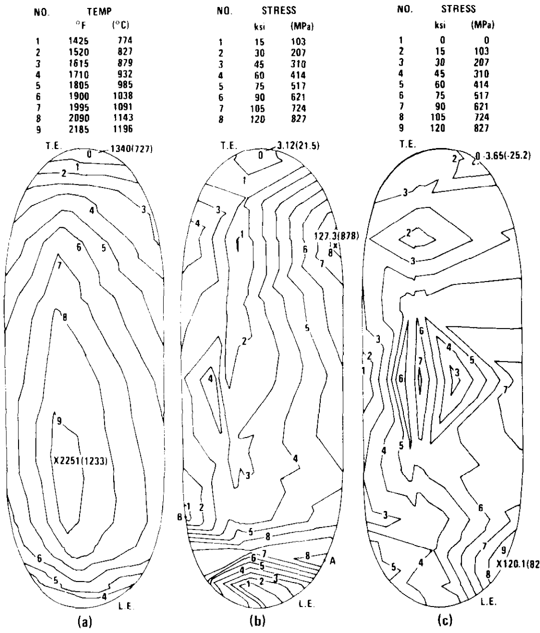
NO. TEMP °F (°C)
1 1425 774
2 1520 827
3 1615 879
4 1710 932
5 1805 985
6 1900 1038
7 1995 1091
8 2090 1143
9 2185 1196
T.E.
1340(727)
X2251(1233)
L.E.
(a)
NO. STRESS ksi (MPa)
1 15 103
2 30 207
3 45 310
4 60 414
5 75 517
6 90 621
7 105 724
8 120 827
T.E.
3.12(21.5)
127.3(878)
A
L.E.
(b)
NO. STRESS ksi (MPa)
1 0 0
2 15 103
3 30 207
4 45 310
5 60 414
6 75 517
7 90 621
8 105 724
9 120 827
T.E.
0 -3.65(-25.2)
X120.1(828)
L.E.
(c)

Figure 3-53. Temperature and Stress Distribution for Airfoil Section 6a Ten Seconds After Flameout from 2500°F Steady-State Gas Temperature [(a) h: High-Low, (b) h: High-Low, (c) h: High-High)]

an exposed part of the entire airfoil surface, the maximum principal stress would be reduced approximately 5 percent from 127,300 psi to 120,000 psi (Figure 3-53). Changes in the heat transfer coefficient at the contact surface had the effect of changing both the location of the maximum stress and the stress distribution.

At the controlled cooldown rate of 25°F/sec, a maximum principal stress of 71,800 psi was reached after 50 seconds. The resultant stress distribution is shown in Figure 3-54. A change in the shutdown transient not only reduced the principal stress maximum but also altered its position significantly.

Flameout produced a maximum principal stress of 123,000 psi at the inner surface of the outer end cap on the suction side near the leading edge of the airfoil after 14 seconds. The three-dimensional aspects of the temperature and stress distributions in the end cap can be obtained from Figures 3-55, 3-56 and 3-57. Figure 3-58 shows the state of stress resulting from cooldown at 25°F/sec. The maximum principal stress of 92,900 psi now occurs within the end cap cavity.

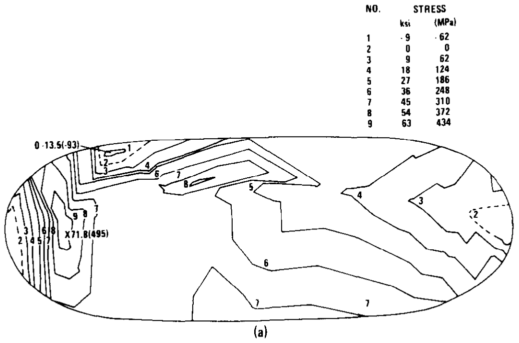

Figure 3-54. Stress Distribution in Airfoil Section 6a at 50 Seconds After Shutdown from 2500°F Steady-State Gas Temperature at 25°F/Sec

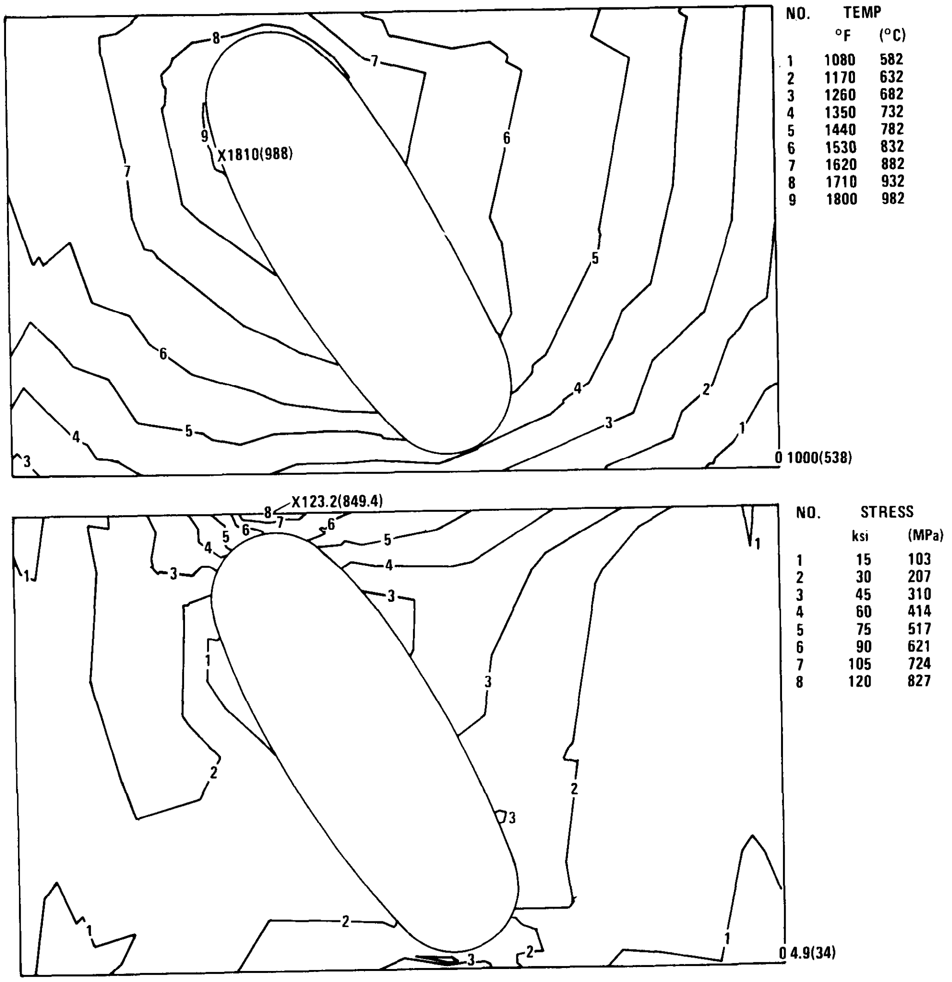

Figure 3-55. Temperature and Stress Distributions for End Cap Section 7e at 14 Seconds After Flameout from 2500°F Steady-State Gas Temperature (h: High-Low)

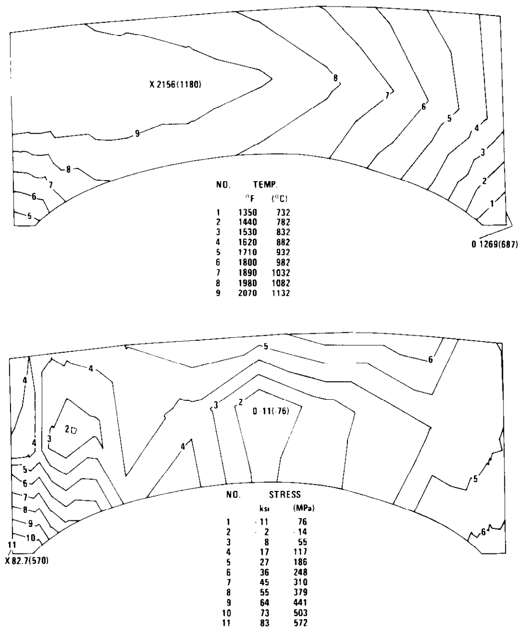

Figure 3-56. Temperature and Stress Distributions for End Cap Section 6e at 14 Seconds After Flameout from F 2500°F Steady-State Gas Temperature (h: High-Low)

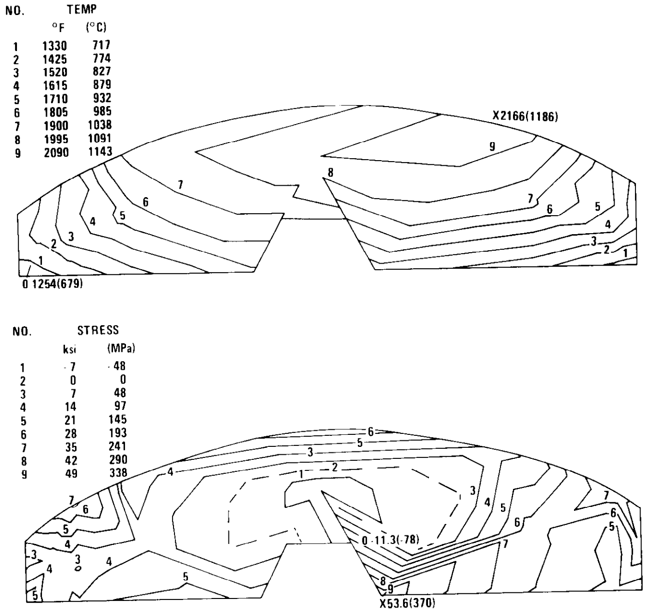

Figure 3-57. Temperature and Stress Distributions for End Cap Section 3 at 14 Seconds After Flameout from 2500°F Steady-State Gas Temperature (h: High-Low)

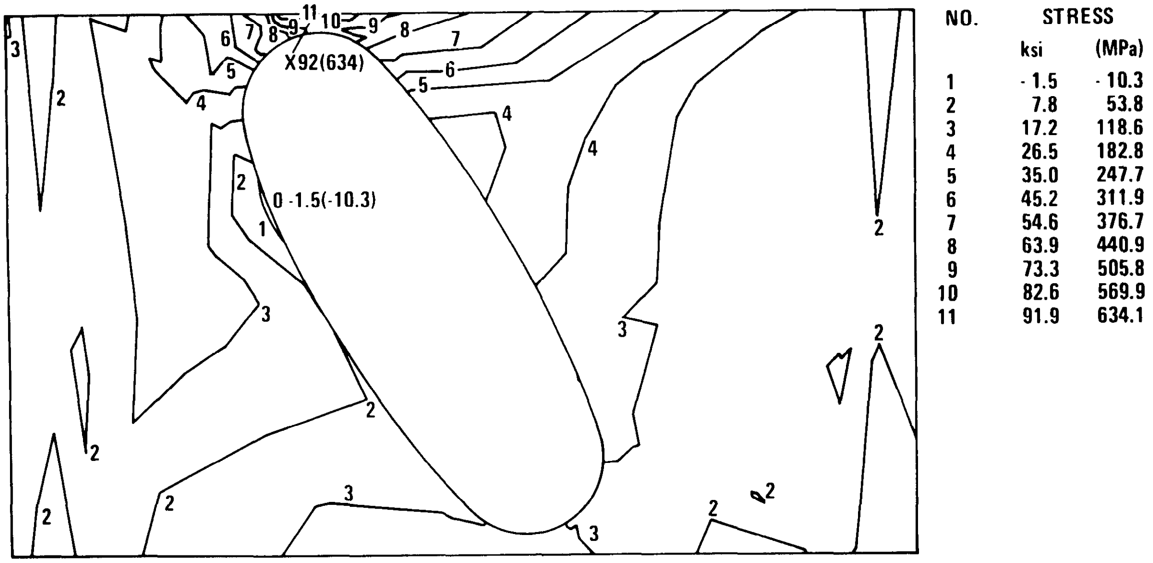

NO.	STRESS ksi	STRESS (MPa)
1	-1.5	-10.3
2	7.8	53.8
3	17.2	118.6
4	26.5	182.8
5	35.0	247.7
6	45.2	311.9
7	54.6	376.7
8	63.9	440.9
9	73.3	505.8
10	82.6	569.9
11	91.9	634.1

(b)

Figure 3-58. Stress Distribution during Cooling at 25°F/Sec from 2500°F Steady-State Gas Temperature in End Cap Section 7e After 58 Seconds

The airfoil-end cap interface was designed for partial area contact with the noncontact portions of the mating surfaces in close proximity. Maximum clearances were specified at room temperature such that the contact stresses due to the axial spring and gas loads remained low. However, differential thermal deformation of the mating geometries under operating conditions could reduce the contact area below that required to maintain acceptable contact stress levels. Alternately, interference could result in contact point changes to create edge loading and large bending and/or torsional stresses. Displacement components v in the y-direction are illustrated on the contact surface at four points, A, B, C and D, in Figure 3-59. Steady-state and transient displacements are defined as the distance a point moves from its original position at room temperature to its position at a given steady-state temperature or position at any transient temperature with respect to time. The transient chosen occurred after 50 seconds under controlled shutdown conditions at 25°F/sec cooling rate.

The u and w displacements, in the x and y directions, respectively, were similar for the airfoil and end cap in both the steady-state and transient cases calculated. These did not create contact problems under the controlled shutdown condition imposed. The displacements, v, in the

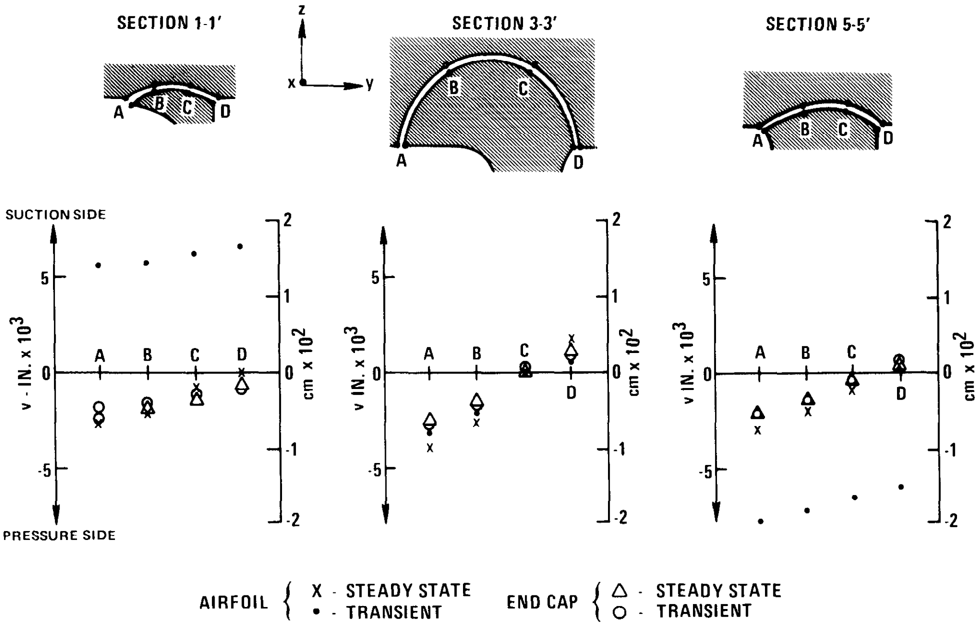

Figure 3-59. Deformations of the Airfoil/End Cap Contact Surfaces at Steady State and During Shutdown Transient

y-direction were also small and of similar magntiude in the airfoil and end cap at steady state. However, transient displacement, v, in the airfoil, at Sections 1 and 5 became significantly large, while corresponding Sections 1', 3' and 5' within the end cap remained small, creating a potential contact edge loading condition with attendant high bending and torsional stresses. At the mid-chord location (Section 3 - airfoil) changes were not appreciable. Section 5, near the leading edge of the airfoil, was displaced toward the pressure side and Section 1, near the trailing edge, was distorted toward the suction side. Recurring displacements in cyclic operations may cause fretting at the interfacial surfaces, further complicating the performance problem.

In spite of aerodynamic and mechanical advantages apparent in the second generation/ceramic stator vane assembly, design viability was not demonstrated. Rigorous three-dimensional stress analysis indicated that the principal tensile stresses, generated under even the moderate conditions of controlled shutdown at 25°F/sec, exceeded the engineering strength of hot pressed silicon nitride and hot pressed silicon carbide. Unfortunately, this analysis lagged the lead time required for vane assembly procurement. Design drawings were prepared previously to insure the availability of hardware for test. Norton manufactured eight first-stage stator vane assemblies (inner and outer end cap plus airfoil per assembly) from HS130 silicon nitride and eight assemblies from NC132 silicon carbide. However, while this design was dropped eventually, the manufacture of parts did provide an additional opportunity for fabrication development.

3.7 THIRD GENERATION VANE ASSEMBLY DESIGN

The third generation stator vane assembly design evolved to meet the general requirements of the Advanced Test Turbine.(6) In reality, it represented a refinement of the first generation design concept modified to provide a tapered-twisted airfoil for proper flow orientation to the first-stage rotor. A toroidal tenon geometry was superimposed upon the actual airfoil cross section with trailing edge relief retained as shown in Figure 3-60 (a photograph comparing design generations I, II and III). No attempt was made to fill the end cap cavities completely along the airfoil tenon mating surface.

The end cap configuration reflected improvements suggested by the stress analysis of the first and second generation components. Kinematic behavior was also considered. The major radius of the toroidal surface of curvature at the end cap insulator interface was specified as 3.000 ± 0.005 inches to resist displacement in the downstream direction regardless of friction coefficient. The groove depth was adjusted to 0.375 ± 0.003 inch, a dimension considered sufficient to prevent dislodgement of the airfoil under hot gas loads. End cap cavities at inner and outer end cap locations were sized and oriented independently to compensate for taper and twist in the airfoil section.

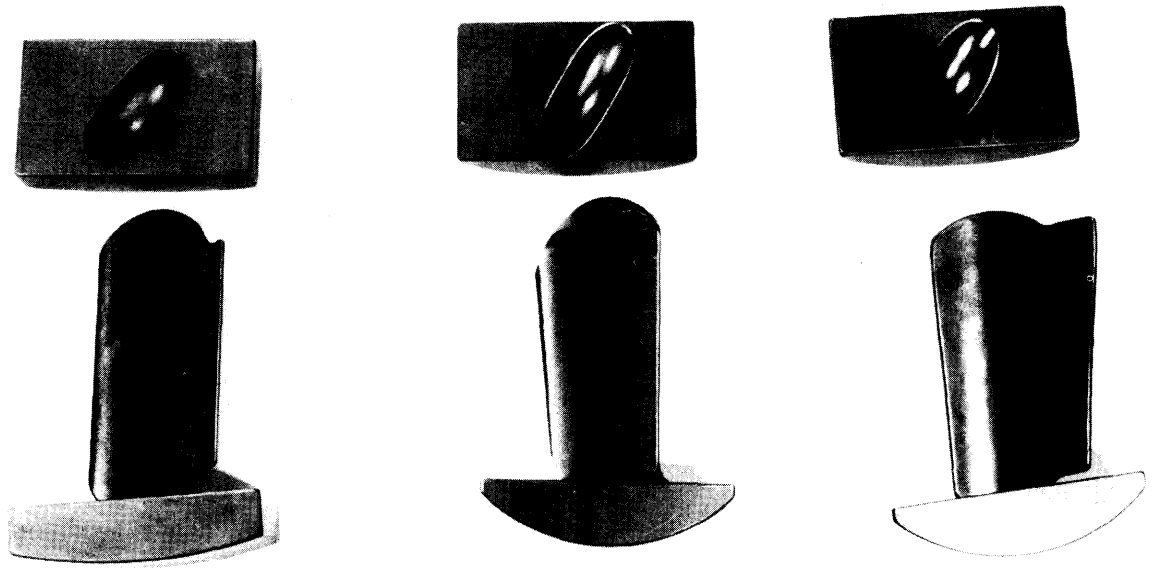

1st Generation 2nd Generation 3rd Generation

1. Parallel-Sided Airfoil
2. Tapered-Twisted Airfoil with Full Cavity-Filling Tenons
3. Tapered-Twisted Airfoil

Figure 3-60. Stator Vane Design Iterations

Particular care was taken in the selection of tolerances at the airfoil/end cap interfaces to insure adequate area contact confinement at the bottom of the end cap cavity without restriction of kinematic motion there beyond desired limites. Radius dimensions, R - 0.000 + 0.003 inches and R + 0.000 - 0.002 inches, were established for major and minor radii of end cap cavity and airfoil tenon, respectively.

The finalized design was not subjected to stress analysis, per se, as a final test of design viability. Time and funding limitations made this impossible considering the decision to eliminate the advanced turbine demonstration and return to the original contract expiration date, June 30, 1976. Certain aspects of previous analyses appear pertinent however. Contact stress calculations at the airfoil tenon/end cap cavity interfaces of the first generation design and the transient thermal stress distributions at airfoil mid-chord for the first generation design apply sufficiently well. The contact displacement analysis for the second generation design was considered valid for first and third generation hardware with provision that differential effects be less pronounced because mating surfaces reduce in direct proportion to the amount of end cap cavity filled by tenon volume. Thermal stresses in the airfoil at the inner and outer tenon locations are proportionally smaller and larger, respectively, in a tapered airfoil section, than for the parallel-sided case cited previously. Contact stresses at the end cap interfaces at these same inner and outer locations are proportionately larger and smaller, respectively, because the major radii decrease (or increase) to establish a smaller (or larger) contact area.

When the advanced turbine test was cancelled, an order to Norton for 100 silicon nitride (NC132) stator vane assemblies of third generation design was ammended and terminated prior to completion to conserve contract funds. Twenty-eight airfoil sections and 44 end caps were actually manufactured. These were used in the static rig test demonstration.

SECTION 4

STATIC RIG TESTING

4.1 STATIC RIG PREPARATION

Modification of an existing facility was initially proposed to meet the contract requirements for the static testing of ceramic stator vane assemblies at peak temperatures of 2200°F and 2500°F in a high velocity gas stream. A new cascade-type rig was eventually designed and built as part of the Stationary Turbine Project at Westinghouse Power Generation Systems Division (formally Gas Turbine Systems Division) in an attempt to test and evaluate full-size ceramic parts in a realistic turbine configuration using a commercial stationary gas turbine fuel nozzle and combustor basket.(3-7) Every effort was made to duplicate actual turbine conditions. Precise control and highly instrumented computerized data acquisition were provided. A 0.8 or 80 percent pressure simulation was the best obtainable because compressors available in the laboratory were capable of delivering air at pressures of 3 to 8 atmospheres only.

The initial version of the static rig, as constructed for 2200°F testing, is presented in schematic plan view in Figure 4-1.(4) Ceramic vane assemblies were tested in their true radial configuration and actually performed a gas turning function. Scale-up problems were eliminated by employing W251 combustor hardware and fuel nozzle assemblies. Internal flow baffles were used to direct inlet air flow and simulate the shell geometry that surrounds the combustion system in a gas turbine. A sight port was provided for the observation of hardware under test.

The cooled-wall combustor produced a temperature-profiled gas stream which passed from the transition piece, through the vane segments in the mitered section, into a complex exhaust duct which channeled the gas to the mixer. The mixer section served to smooth the temperature profile of the gas stream by turbulence so that hot gas of a more uniform temperature was monitored by control instrumentation. A high temperature composite refractory material was employed to insulate the mixer for applications up to 3000°F. The operating pressure level of the rig was controlled by the back pressure valve located downstream of the measurement section.

Key elements of the static rig are illustrated for ready reference. The rig itself is shown in Figure 4-2 as it appeared in the Combustion Laboratory ready for use. The mitered section with barrier plate and internal baffles, the mitered section internal with test fixture

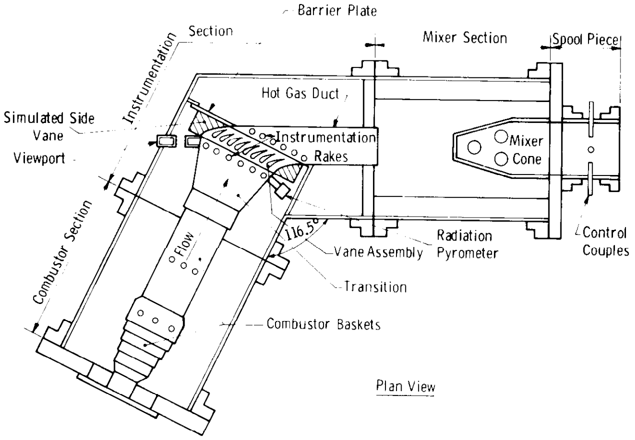
Barrier Plate
Instrumentation Section
Mixer Section
Spool Piece
Hot Gas Duct
Simulated Side Vane
Viewport
Instrumentation Rakes
Mixer Cone
Combustor Section
Flow
116.5°
Vane Assembly
Radiation Pyrometer
Control Couples
Transition
Combustor Baskets
Plan View

Figure 4-1. Modified Static Test Rig for 2200°F Test of Ceramic Vanes

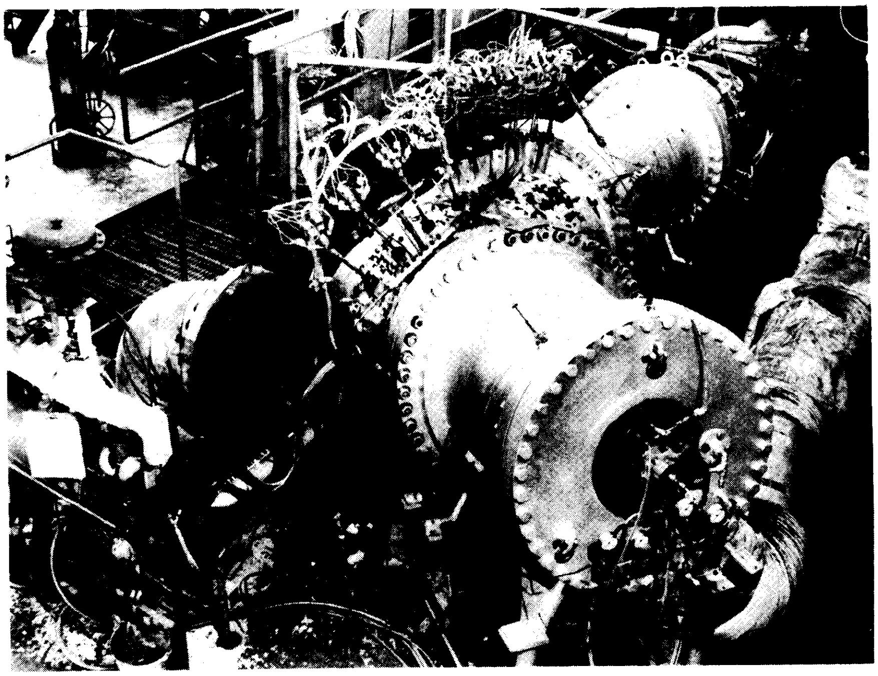

Figure 4-2. The Static Rig for Testing Ceramic Stator Vanes at 2200 and 2500°F (Mitered Section is 42 Inches in Diameter)

attached to the barrier plate, and the hot gas duct for 2200°F service are shown in Figures 4-3, 4-4 and 4-5, respectively. The actual flow path components, i.e., the instrumented combustor, the transition piece attached to the ceramic test assembly, and a metal exhaust duct with instrumentation rakes fit inside the five basic components of the refractory-lined outer shell structure.

Extensive instrumentation was provided. Gas passage temperature profiles were measured by fast response aspirating thermocouple rake systems located upstream (42 thermocouples) and downstream (49 thermocouples) of the ceramic stator vanes. All of the metal support hardware was monitored with thermocouples that were strategically located at shoes, air baffles, inner and outer housing rings, side vanes and spring housings. These thermocouples were used to evaluate heat transfer analyses, cooling air schemes and design/analysis characteristics. Specially designed load cells were installed to measure the radial load on each pair of vane assemblies during spring installation, loadup and during various phases of rig operation.

Unfortunately, attempts to maintain strain gauges on silicon nitride vanes under transient thermal conditions proved unsuccessful. However, an instrumented (with thermocouples and strain gauges) metal airfoil/end cap assembly was designed and fabricated to obtain meaningful heat transfer and stress data up to 1400°F. (The heat transfer and stress tests

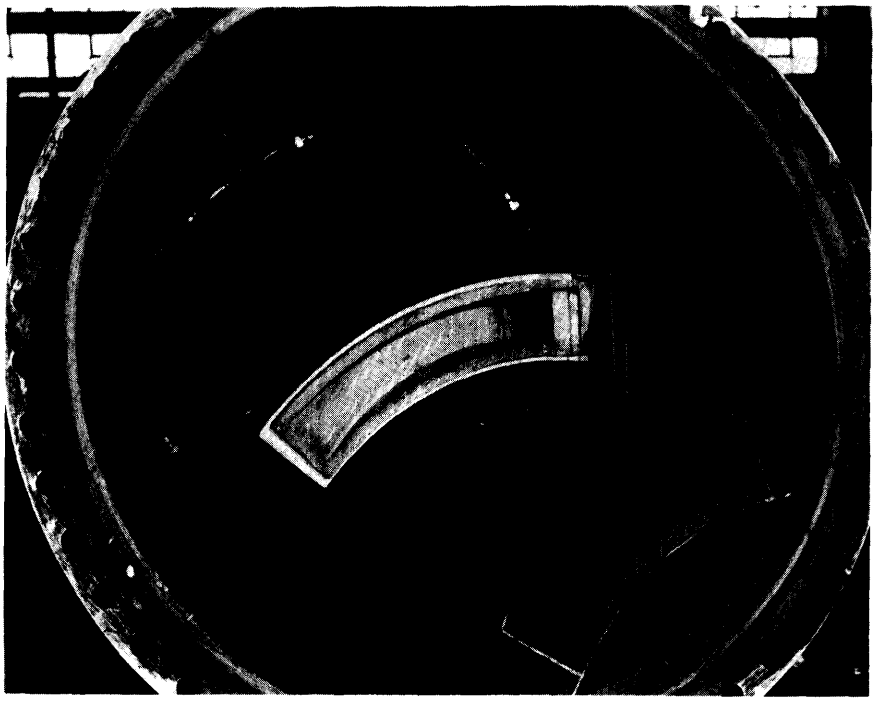

Figure 4-3. Mitered Section of Static Rig Showing Barrier Plate for the Installation of the Test Assembly

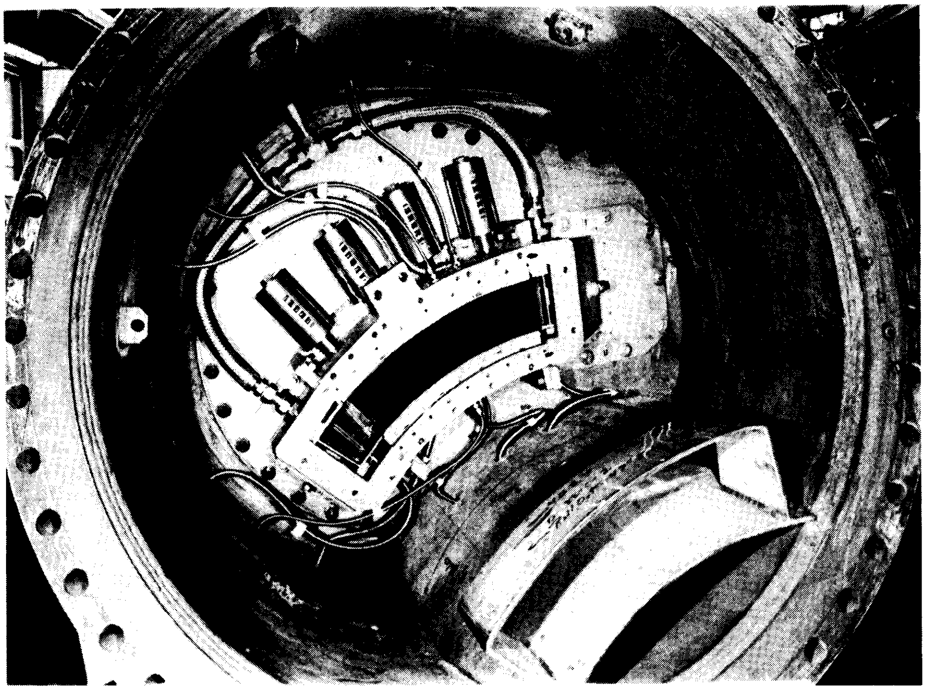

Figure 4-4. Mitered Section of the Static Rig with Test Assembly Installed

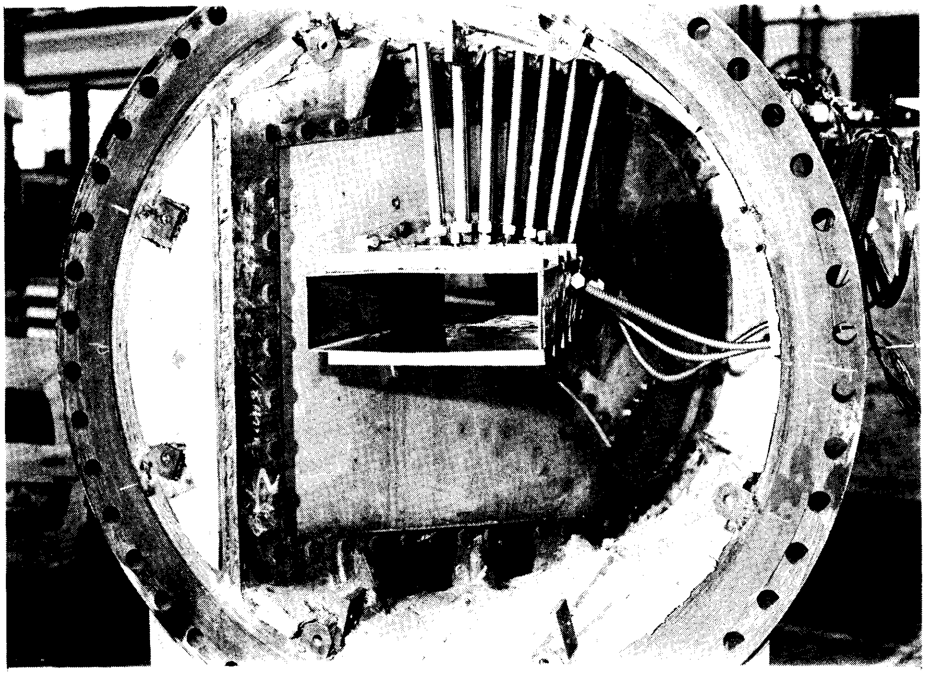

Figure 4-5. Hot Gas Duct for 2200°F Static Rig Test

to correlate two- and three-dimensional design/analysis techniques were scheduled but never run because vane test delays preempted them and the contract finally expired.)

Existing laboratory facilities accurately recorded air and fuel flows, pressures and temperatures. A Westinghouse Veritrak temperature controller reproducibly followed a prescribed mode of operation by sensing and responding to the uniform operating temperature of the gas, downstream of the mixer section, through a system of feedback loops and variable function generators.

The raw data, whether in the transient or steady-state mode, were collected by a rapid data acquisition system. Various data sequencing tapes controlled data retrieval during transient operation at acquisition rates of seven pieces of information per second. Computer programs converted the values directly into engineering units during the 2200°F test phase.

A rugged platinum-platinum/rhodium aspirating thermocouple, monitoring the peak gas temperature in the transition piece, functioned to exclude extreme temperature excursions. If the gas temperature in the rig exceeded 2450°F, fuel flow interrupted, automatically terminating the test to protect rig components and ceramic test parts from possible damage.

The test section contained eight ceramic stator vane assemblies (Norton HS130 silicon nitride) positioned between two air-cooled metal side vanes (X-45 alloy) which enclosed the gas passage on each side. The ceramic vane assemblies (an airfoil seated in toroidal cavities between an inner and an outer end cap) were supported in pairs between lithium aluminum silicate insulators (Owen Illinois CERVET C-140), woven metal cushion material, and Haynes 188 metal shoes (Figure 4-6). Two metal pivots supported each inner shoe while a single spring-loaded plunger and pivot were used at each outer shoe location. The entire assembly was fastened between inner and outer metal (Type 405 stainless) housing ring segments. Suitable cooling, seals and air baffles were provided to keep the metal support system within specified temperature limits. Figure 4-7 shows the fully instrumented vane assembly test section as it appeared before being bolted in place against the barrier plate.

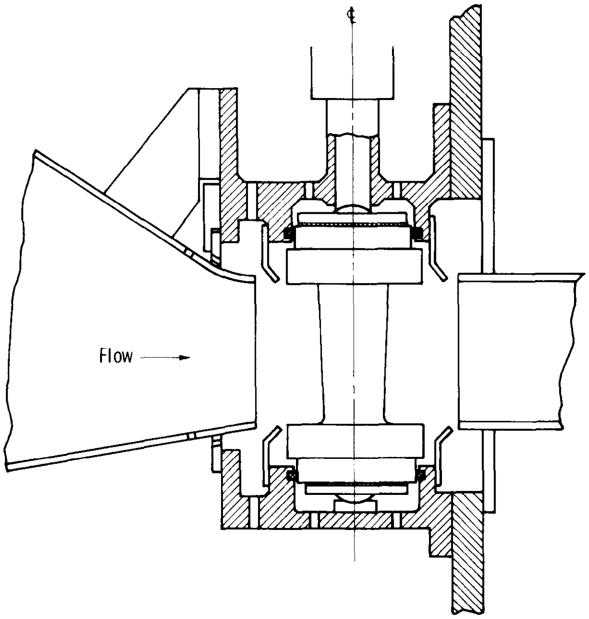

Figure 4-6. Ceramic Stator Vane Assembly for Static Rig Testing at 2200°F

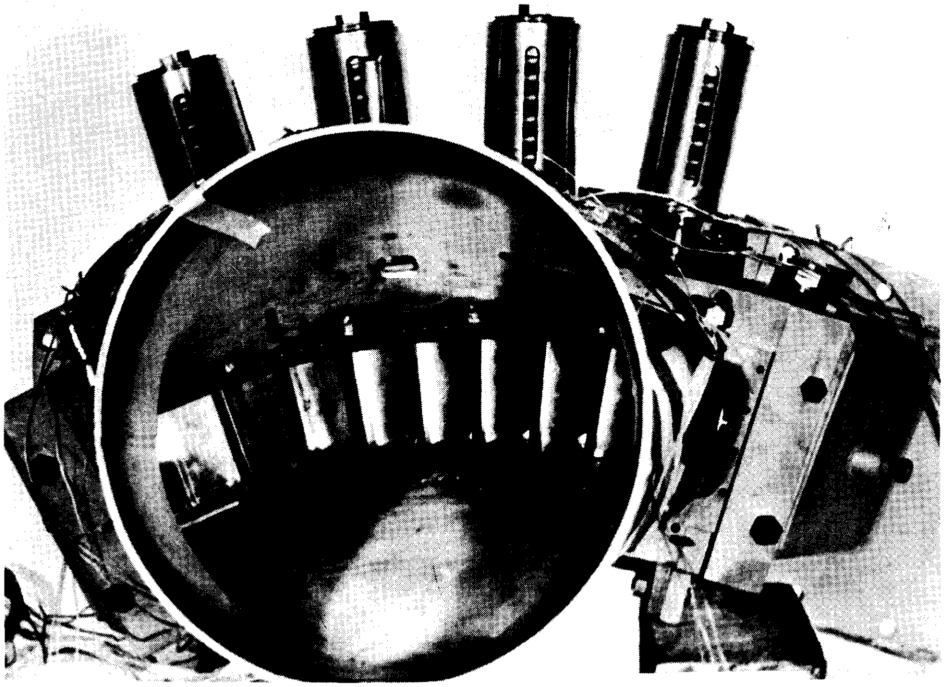

Figure 4-7. Instrumented Test Assembly for the 2200°F Static Rig Testing of Silicon Nitride Stator Vanes

4.2 DEFINITION OF THE STATIC RIG TEST CYCLE

Since stationary gas turbine generators are traditionally used to meet peak power requirements, the static rig environment for the test and evaluation of ceramic stator vanes was selected to represent a cyclic mode of operation where transient thermal conditions are considered most critical to component life and reliability. Much thought was given initially to the use of emergency shutdown or flameout as the determinant factor in the test because it occurs relatively often in commercial service whenever fuel is interrupted for any reason such as insufficient supply or abnormal operating condition, as the result of, for example, over-speed or over-temperature. Approximately 100 cycles were accepted arbitrarily as representative of start-stop sequences in actual use at normal overhaul or servicing intervals.

Under emergency shutdown or flameout conditions, however, the turbine inlet temperature was expected to drop from 2500°F peak to 1100°F within 2 seconds for the gas temperature profile shown in Figure 4-8. The 2500°F curve was extrapolated from actual data collected from a Westinghouse W251, 30 megawatt stationary gas turbine, operating at 1990°F average turbine inlet temperature (the system reserve condition), using a W251 AA combustor identical to the one specified for static rig tests at 2200°F. An analysis of the 2500°F peak temperature revealed principal stress levels in Si_3N_4 vanes reaching 70,000 psi and 58,000 psi at 1675°F and 1750°F for a turbine and the static rig, respectively

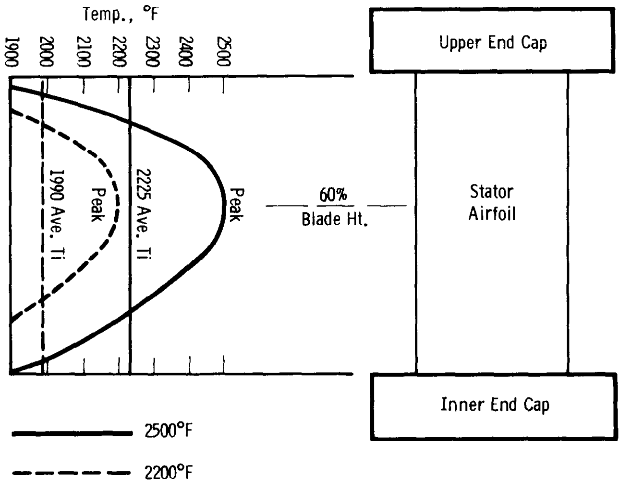

Figure 4-8. Relation of Peak Ceramic Vane Temperature to Temperature Profile and Average Turbine Inlet Temperature

(Figure 4-9). Results for the 2200°F peak condition appear in Figure 4-10 where the difference between the turbine and rig is attributed to pressure ratio (10.5:1 for the turbine vs 8.0 max.:1 for the rig) and the resultant heat transfer coefficients developed, respectively.

The calculated stress values were considered too high for acceptable cycle life based upon preliminary tensile test data for silicon nitride. At 1900°F, 20,000 psi stress appeared to be a reasonable limit based upon cursory low cycle fatigue results at 20,000 psi stress level, with increases to 30,000 and 50,000 psi permissible at 1500°F and 900°F, respectively.

Alternate shutdown ramps were investigated to find a cycle description which would meet the proposed conditions for a controlled emergency shutdown without subjecting ceramic components to an unfavorable stress history. Reductions in linearly programmed quenching rate from 770°F/sec to 315°F/sec, 100°F/sec, or 25°F/sec had an advantageous effect on maximum principal stress in the ceramic airfoil. At 315°F/sec the tensile stress maximum reached 68,000 psi at a calculated airfoil temperature of 1480°F, 8 seconds after shutdown, whereas at 100°F/sec, the maximum stress ascended to 40,000 psi at 1850°F after 12 seconds (Figure 4-11).

Figure 4-12 illustrates the extreme effect for 25°F/sec. Here, the maximum stress (17,000 psi) is developed at 2000°F after 25 seconds.

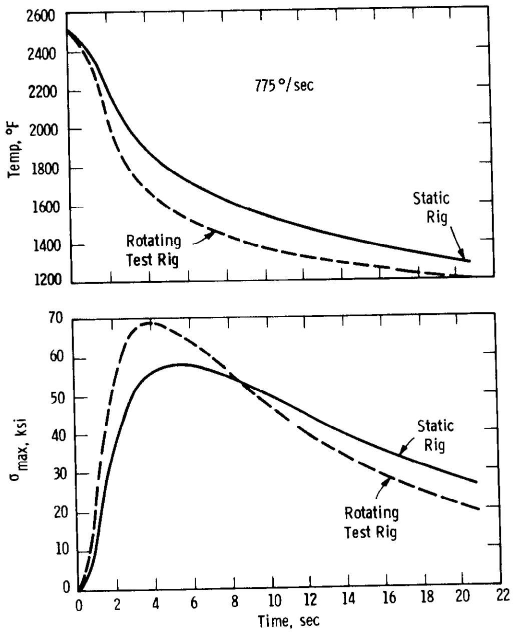

Figure 4-9. Shutdown from 2500°F to 950°F (Gas Temperature) in 2.0 Seconds